University of Denver
Digital Commons @ DU

Electronic Theses and Dissertations | Graduate Studies

2020

Fluid Dynamics Characterization of Transcatheter Aortic Valves

Mohammed Barakat
University of Denver

Follow this and additional works at: https://digitalcommons.du.edu/etd

Part of the Biological Engineering Commons

Recommended Citation

Barakat, Mohammed, "Fluid Dynamics Characterization of Transcatheter Aortic Valves" (2020). *Electronic Theses and Dissertations*. 1720.
https://digitalcommons.du.edu/etd/1720

This Dissertation is brought to you for free and open access by the Graduate Studies at Digital Commons @ DU. It has been accepted for inclusion in Electronic Theses and Dissertations by an authorized administrator of Digital Commons @ DU. For more information, please contact jennifer.cox@du.edu,dig-commons@du.edu.

Fluid Dynamics Characterization of Transcatheter Aortic Valves

A Dissertation

Presented to

the Faculty of the Daniel Felix Ritchie School of Engineering and Computer Science

University of Denver

In Partial Fulfillment

of the Requirements for the Degree

Doctor of Philosophy

by

Mohammed Barakat

August 2020

Advisor: Ali N. Azadani, Ph.D.

Author: Mohammed Barakat
Title: Fluid Dynamics Characterization of Transcatheter Aortic Valves
Advisor: Ali N. Azadani, Ph.D.
Degree Date: August 2020

Abstract

Aortic stenosis due to degenerative calcific aortic valvular disease is the most reason for aortic valve replacement in developed countries. Aortic stenosis affects up to 7% of the world population, and current clinical data indicate that the number of the affected people could be triple by 2050, due to population ageing and health lifestyle. Transcatheter aortic valve replacement (TAVR) was introduced as a minimal invasive treatment of severe aortic stenosis. Even though surgical aortic valve replacement (SAVR) is considered the golden standard treatment for severe aortic stenosis patients, TAVR showed equivalent or even superior outcome compare to SAVR. Currently, transcatheter aortic valves (TAVs) have limited clinical data in term of fluid dynamics performance of TAVs, in contrast to surgical aortic valves (SAVs). Due to limitations associated with devices that are used to evaluate the performance of TAVs in patients such as echocardiography, magnetic response imaging (MRI) and an accurate method to detect and evaluate any leakage. Thus, an experimental testing and computational modeling were performed to compare the performance of TAVs to SAVs in term of hemodynamic performance and addressing some clinical complications that are associated with TAV devices. Therefore, the objectives of this dissertation were to used particle image velocimetry (PIV) to obtain velocity and shear stress contours to indicate any damage to blood elements that could lead to stroke. Additionally, investigate the cause of reduced TAV leaflets motion post-TAVR procedure using blood residence time (BRT) approach. Furthermore, validating the current guideline uses to evaluate paravalvular leakage (PVL) severity and develop a new methodology to assess and evaluate the severity of PVL post-TAVR based on fluid dynamics. Moreover, developing and validating non-invasive procedure to estimate energy loss post-TAVR during the cardiac cycle

and determine the workload imposes on the left ventricular. Thus, the main goal of this dissertation was to develop experimental testing to measure hemodynamics performance of TAVs and validating computational modeling output in term of flow field.

Acknowledgments

I would like to express my sincere thanks to my chair my committee chair Dr. Ali Azadani, who has the attitude and the substance of a genius. He continually and convincingly conveyed a spirit of excitement regarding research in the amazing field of heart valves to save patients life. Without his guidance and help, this dissertation would not have been accomplished. Also, I would like to thank my committee members, Professor Matt Gordon, Dr. Yun-Bo Yi and Dr. Dinah Loerke for their assistance and advice to improve this dissertation.

In addition, I am also very grateful to all my colleagues and friends in the DU Cardiovascular Biomechanics Lab at University of Denver who have worked with me during my Ph.D. program, especially Mostafa Abbasi, Koohyar Vahidkhah, Dong Qiu, Farhan Khodaee and Saba Ravaghi.

Also, I would like to express my thanks to my mother, father and siblings, whom helped me through those years for their emotional and financial support. Also, I am grateful to all my wonderful friends and neighbors in Cheeseman Park area for the emotional support during those years. This dissertation is detected to them. Additionally, I would like to express my deepest appreciation to Jazan University for the generous Financial support during my PhD program.

Table of Contents

Chapter 1: Introduction 1
1.1 Anatomy and Structure of the Heart 1
1.2 Valvular Disease 3
1.3 Aortic Stenosis 3
1.4 Surgical Aortic Valve Replacement 4
1.5 Transcatheter Aortic Valve Replacement 6
1.6 Clinical issues associated with TAVR 9
1.6.1 Cerebral Embolisms 9
1.6.2 Reduced motion of TAV Leaflet 10
1.6.3 Paravalvular Leakage post-TAVR 11
1.7 Objectives 12

Chapter 2: Fluid Dynamics Characterization of Transcatheter Aortic Valves Using Particle Image Velocimetry 14
2.1 Introduction 14
2.2 Material and Method 16
2.2.1 Transcatheter Aortic Valve 16
2.2.2 Experimental Setup 16
2.2.3 Particle Image Velocimetry 17
2.3 Result 20
2.3.1 Hemodynamics performance of the valves 20
2.3.2 PIV Results of Surgical valve 22
2.3.3 PIV Results of CoreValve 22
2.3.4 PIV Results of SAPIEN 3 23
2.4 Discussion 27
2.4.1 Summary 27
2.4.2 Fluid Dynamics Impact on Thrombotic and Hemolytic 27
2.4.3 Validation of CFD Simulation 28
2.4.4 Study Limitation 30
2.5 Conclusion 31

Chapter 3: Valve Thrombosis Post Transcatheter Aortic Valve Replacement: Significance of blood Stasis on the Leaflets 32

3.1 Introduction 32
3.2 Material and Method 34
3.2.1 Experimental Setup 34
3.2.2 Validation of FSI Simulation 35
3.2.3 CFD Simulation Steps 36
3.2.4 Estimating BRT in Patient-Specific Geometry 36
3.3 Result 38
3.3.1 Hemodynamics Performance of the Valve 38
3.3.2 Validation of FE and CFD Simulation 39
3.3.3 Quantifying BRT in Surgical and Transcatheter Valve During Forward Flow 41
3.3.4 Quantifying BRT in Surgical and Transcatheter Valve During Valve Closing 42
3.3.5 Quantify Blood Resident Time in Low Cardiac Cycle. 43
3.3.6 Quantifying BRT in two models 45
3.4. Discussion 48
3.4.1 Summary 48
3.4.2 Thrombosis Formation post TAVR and SAVR 48
3.4.3 Thrombosis Formation in Low Cardiac Output 49
3.4.4 Study Limitation 50
3.5 Conclusion 51

Chapter 4: Assessment of Paravalvular Leakage Post Transcatheter Aortic Valve Replacement: A New Approach Based on Maximum Momentum Flux 52
4.1 Introduction 52
4.2 Material and Method 54
4.2.1 Theoretical Background 54
4.2.2 CFD Simulation of PVL 56
4.2.3 Fabrication of PVL and Valve Models 58
4.2.4 Experimental setup 59
4.2.5 Doppler Measurements 60
4.3 Results 62
4.3.1 CFD Steady Validation of Circumferential Extent 62
4.3.2 Estimating Maximum Momentum Flux using CFD Simulation 66
4.3.3 Estimating CE Experimentally. 68
4.3.4 Maximum Momentum Flux In Vitro 70

4.4 Discussion 73
4.4.1 Summary 73
4.4.2 Validation of CE 74
4.4.3 Maximum Momentum Flux 75

Chapter 5: Quantification the severity of Paravalvular Leakage Based on Energy Loss 78
5.1 Introduction 78
5.2 Material and Method 80
5.2.1 Energy loss Approach 80
5.2.2 Heart valves and PVL Model 81
5.2.3 In Vitro testing of TAVs 82
5.3 Results 84
5.3.1 Invasive energy loss 84
5.3.2 Non-invasive energy loss 87
5.4 Discussion 90
5.4.1 Summary 90
5.4.2 Energy loss Measurements 90
5.5 Conclusion 93

Chapter 6: Conclusion and Future work 94
6.1 Conclusion 95
6.2 Future Works 97

List of Figures

Figure 1.1: Anatomy structure of the human heart. Red arrow shows blood flow direction in left ventricle. Blue arrow shows blood flow direction in the right ventricle. Adopted from (Regina Bailey 2019) 2
Figure 1.3: (A) Mechanical heart valve (courtesy of www.heart-valve-surgery.com). (B) Bioprosthetic heart valve (courtesy of www.edwards.com). 5
Figure 1.5: Different design configuration of TAVs devices that are currently available. permission from (Sondergaard, 2016). 8
Figure 1.6: MRI results of 4 patients showing location of cerebral embolism without clinical stroke or TIA event. (A) single right embolus. (B) Multiple embolism in left and right of the brain. Permission from (Van Belle et al., 2016). 9
Figure 1.8: Echocardiography short axis view of SAPIEN 3 after one day of implementation. Permission from (Athappan et al., 2013) 11

Figure 2.1: (a) 25-mm surgical Carpentier-Edwards PERIMOUNT Magna bioprosthetic aortic valve. (b) 26-mm self-expanding Medtronic CoreValve. (c) 26-mm Edward SAPIEN 3 transcatheter heart valve. Adopted from (Vahidkhah, Barakat, et al., 2017). 19
Figure 2.2: Custom-built pulse duplicator system and PIV setup. 19
Figure 2.3: In vitro pressure and flow waveforms of (a) 25-mm surgical Carpentier-Edwards PERIMOUNT Magna bioprosthetic aortic valve, (b) 26-mm self-expanding Medtronic CoreValve, and (c) 26-mm Edward SAPIEN 3 transcatheter heart valve. 21
Figure 2.4: Instantaneous velocity and viscous shear stress fields of 25-mm surgical Carpentier-Edwards PERIMOUNT Magna bioprosthesis in various phases of a cardiac cycle. 24
Figure 2.5: Instantaneous velocity and viscous shear stress fields of 26-mm Medtronic CoreValve in various phases of a cardiac cycle. 25
Figure 2.6: Instantaneous velocity and viscous shear stress fields of 26-mm Edwards SAPIEN 3 in various phases of a cardiac cycle. 26

Figure 3.1: CAD models (A) surgical valve and (B) TAV model 37
Figure 3.2: Patient-specific geometry. (A) 3D patient-specific geometry from CTA images. (B) TAV leaflets are surrounded by the a failed degenerated bioprosthesis valve as in ViV (top), TAV leaflets surrounded by the native valve as in TAV (bottom). (C) CFD TAV model. 38
Figure 3.4: Validation of FE and CFD simulation. (A) Comparison between leaflet motion captured by the high-speed camera and FE simulation. (B) Comparison between flow field captured via PIV and CFD simulation at the peak of systole. 40
Figure 3.6: CFD results demonstrating the particles released in the ROI during stage-III in a cardiac cycle. (A) Snapshot illustrates particles released downstream of surgical valve. (B) Snapshot illustrates particles released downstream of TAV. 44
Figure 3.7: illustrates the contours of BRT on TAV model leaflets during a whole cardiac cycle. (A) BRT at cardiac output 5 L/min. (B) cardiac output at 3.5 L/min/ (C) cardiac output at 2 L/min. 45

Figure 3.8: Statistical compression average BRT between TAV and surgical models in different stages of the cardiac cycle. I-forward flow, II-closing, III-end of closing to mid-diastole, IV-mid diastole to early systole. 47
Figure 3.9: Evaluation n of the largest BRT areas on TAV leaflets at three different cardiac output. The vertical axis representing the area of three leaflets on which BRT is higher than critical values on the horizontal axis. 47

Figure 4.1 (a) Schematic of the idealized flow simulation model for PVL. (b) Overview of the proposed approach for the assessment of the severity of PVL regurgitation. 56
Figure 4.3. (a) TAVR implanted on calcified valve, the white arrows show the TAV's commissure. (b) Show the bottom view of TAV. (c) SAPIEN 3 TAV implanted in the 3D-printed washer, the black arrows show the gaps facing the valve's commissure. 59
Figure 4.4. (a) Pulse duplicator system with valves positioned within the system. (b) Diagram layout of the experiment setup. 61
Figure 4.5. CFD results simulation of paravalvular leakage. (a,b) The corresponding contours of flow velocity magnitude of PVL from short axis view. (c) Long axis view velocity flow contours of PVL jet. 62
Figure 4.8: In vitro color Doppler images of multiple degrees of PVL severity were taken from the short axis view. (a) Shows results RV of 11.46 ml/beat. (b) Shows results RV of 35.74 ml/beat. (c) Shows results RV of 60.25 ml/beat 69
Figure 4.9: Linear correlation between the measured RV and the estimated CE obtained from the in vitro measurements. 70
Figure 4.10: A sample of echocardiographic obtained from different level of PVL severity. (a) a mild case with RV of 13.60 ml/beat. (b) a moderate case of 46.65 ml/beat. (c) a severe case of 64.32 ml/beat. The first top raw shows color doppler of the LVOT area. The middle raw shows pulse wave velocity images at the LVOT area. The bottom raw shows continuous wave of the velocity magnitude at the vena contracta. 72

Figure 5.1: (A=a) 3D-printed washer with 3 gaps. (B) A 26 mm Edwards SAPIEN 3 implemented within the 3D-printed washer. (C) schematics show the flow through PVL channel. 82
Figure 5.2: A custom-built pulse duplicator system (BDC Labs, Wheat Ridge, CO) 83
Figure 5.3: Pulse duplicator result with RV of 48.51 ml/beat. (a) pressure waveform of one cardia cycle at mean aortic pressure of 100 mmHg, the blue sold line corresponds to aortic pressure, the red dash line corresponds to left ventricular pressure. (b) the measured flow rate across the aortic valve during the cardiac cycle, on the right, the red area in the right image shows the amount of leakage during diastole. 85
Figure 5.4: Linear correlation between the measured regurgitation volume and the measured energy loss invasively. Solid blue circle and empty diamond correspond to measured energy loss at mean aortic pressure of 100 mmHg and 120 mmHg, respectively. 86
Figure 5.5: Chart bar shows the measured total energy loss invasively per cardiac cycle. 86
Figure 5.6: A sample of echocardiography parameters that were used to estimate the maximum momentum flux. (a) Long axis view of the velocity jet, illustrating measurement locations. (b) CW Doppler measurement of the maximum velocity of the jet at the vena contracta, red arrow corresponds to systole and blue corresponds to diastole. (c) Short axis view of the area of the jets

in the LVOT region. (d) PW Doppler measurement of velocity magnitude at the location where the area was estimated..... 88
Figure 5.9: Linear correlation between the measured energy loss invasively and noninvasively during diastole. 92
Figure 5.10: Linear correlation between the measured energy loss invasively and noninvasively during the cardiac cycle..... 92

Chapter 1: Introduction

1.1 Anatomy and Structure of the Heart

The human heart function is to pump oxygenated blood from the heart into the rest of the body. The heart is located between the two lungs in the middle of the chest. The heart has two sides, each side divided into two chambers which are separated by valves as shown in Fig. 1.1. The upper chamber is known as the atrium, while lower is known as ventricle. In this dissertation, I focused on the left side of the heart which consist of the left atrium and ventricular. The left atrium and ventricle are separated by mitral valve, while the left ventricle and aorta are separated by aortic valve. The main function of the aortic valve is to prevent backward flow of blood, and to ensure one directional blood flow.

On the other hand, the cardiac cycle is divided into two phases: diastole and systole. When the left ventricle contracts, blood pumps out (forward flow) through the aortic valves into the aortic ascending then into the rest of the body. The aortic valve has three flaps called leaflets, they open and close during systole and diastole, respectively. During the diastole phase, the mitral valve opens to allow blood flow from left atrium into the left ventricle. While in systole phase, the left ventricle contracts opening the aortic valve allows blood flow out of the heart into the body. Wiggers diagram is shown in Fig. 1.2, which illustrate the motion of blood with respect to volume, pressure and valves movement during the cardiac cycle. The Pressure in left ventricular must exceed the pressure in the aorta among normal patients during systole. In addition, pressure of the left atrium is usually between 2 to 8 mmHg and pressure of left ventricle is between 2 to 120 mmHg. On the other hand, aortic pressure is usually from 80 to 120 mmHg.

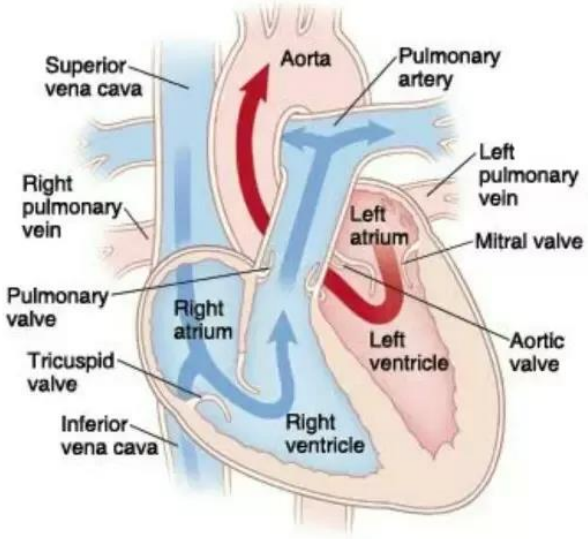

Figure 1.1: Anatomy structure of the human heart. Red arrow shows blood flow direction in left ventricle. Blue arrow shows blood flow direction in the right ventricle. Adopted from (Regina Bailey 2019)

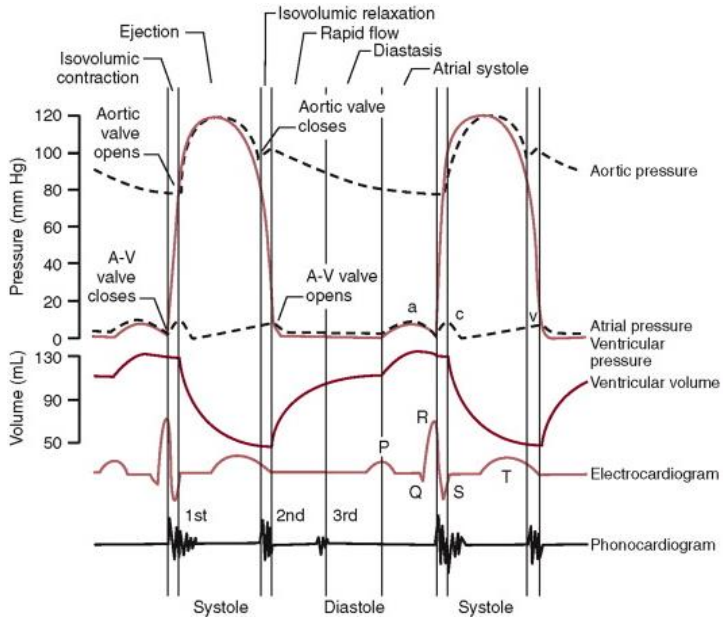

Figure 1.2: Illustrate pressure waveform diagram during the cardiac cycle. Adopted from (Robert Carroll 2007).

1.2 Valvular Disease

The main function of the heart valves is to arrange the motion of the blood and prevent blood moving backward. Valvular disease is one of the major causes of death in developed countries (Iung et al., 2003). There are several causes of valvular disease such as: age, infection, lifestyle, rheumatic fever and valve calcification. Stenosis and regurgitation are the most common valvular disease in the world. Valve stenosis occurs when the valve leaflets narrow where the valve does not open fully due to calcification, which results in reduce blood flow through the valve. On the other hand, valve regurgitation occurs when the valve leaflets don't close properly, leading to backward blood flow. In 2015, the total number of living people with valvular disease was 33.4 million (Association, 2017; Benjamin, Muntner, & Bittencourt, 2019). In the United States, the total of death due to valvular disease is 139,229 (Bevan, Zidar, Josephson, & Al-Kindi, 2019).

1.3 Aortic Stenosis

Each year approximately 300,000 people in the United States are diagnosed with sever aortic stenosis. Systemic severe aortic stenosis is linked to high mortality rates, up to 50% per year (Bevan et al., 2019; Nkomo et al., 2006). The prevalence of aortic stenosis is more likely to increase as population ages (Coffey et al., 2014). Aortic stenosis could be a result of degenerate calcified trileaflet aortic valve or a congenital heart defect bicuspid aortic valve. Generally, aortic stenosis prevents the aortic valve from opening fully, resulting in reducing oxygenated blood flow forward through the valve due to the present of the calcified or defected valve. In this case, the heart must work harder to compensate the body with the needed oxygenated blood.

The severity of aortic stenosis is classified as mild, moderate and severe based on measuring the opening area of aortic valve using echocardiography (Vahanian & Otto, 2010). Symptoms of aortic stenosis can be different or may not be present in most patients, especially

among mild and moderate patients. However, patients with severe aortic stenosis usually have the following symptoms: angina, syncope and or dyspnea (Vahanian & Otto, 2010). After classifying the severity of aortic stenosis, a special team of cardiologists will determine the best treatment option for the patient.

The classical treatment for aortic stenosis is surgical aortic valve replacement (SAVR), where the damaged valve repaired and is replaced it with a new valve. However, TAVR is considered an effective treatment with less mortality rate and fast recovery time compared to SAVR (Aranki et al., 1993). However, SAVR is an invasive procedure which requires an open heart surgery, either with a mechanical or bioprosthetic heart valve, is a gold standard treatment for patient with severe aortic stenosis (Walther, Blumenstein, van Linden, & Kempfert, 2012). On the other hand, SAVR may not be an effective treatment for old patients, especially patients whom are at high risk of open-heart surgery. Therefore, transcatheter aortic valve replacement (TAVR) has emerged as a safe alternative treatment to SAVR.

1.4 Surgical Aortic Valve Replacement

SAVR is the treatment of choice for patients with severe aortic stenosis. In this procedure, an incision is made in the chest to access the aortic valve location. The calcified, or defected, aortic valve is removed and replaced with either a mechanical valve or a bioprosthetic valve as shown in Fig. 1.3. The mechanical heart valve is more durable and reliable; however, patients with mechanical heart valve must receive anticoagulant for the rest of their life, due to the thrombogenicity of the mechanical valves material. On the other hand, bioprosthetic aortic valves (BAVs) were introduced for patient who cannot take anticoagulant.

Generally, BAVs are made of bovine pericardium or porcine aortic valves, also it can be made from equine pericardium. The best advantage of BAVs is that patients are not required to receive anticoagulant. Additionally, BAVs material has shown long term durability in term of

stress distribution on the leaflets. BAVs perform to imitate the one-way blood flow as the normal valve, by sealing valve leaflet against each other, or it can be stented or stentless as shown in Fig.1.4. Surgical aortic valves (SAVs) have shown good outstanding in term of their biocompatibility and hemodynamic performance; however, SAVs are less durable than mechanical valve . The Capentier-Edwards (CE) PERIMOUNT pericardial bioprosthesis (Edwards Lifesciences, Irvine, CA) as shown in Fig. 1.4 has an excellent freedom from structural valve deterioration and satisfaction in term of hemodynamic performance up to 18 years of operation. However, SAVs may not be a recommended treatment option, especially for patient at high-risk of open-heart surgery.

Figure 1.3: (A) Mechanical heart valve (courtesy of www.heart-valve-surgery.com). (B) Bioprosthetic heart valve (courtesy of www.edwards.com).

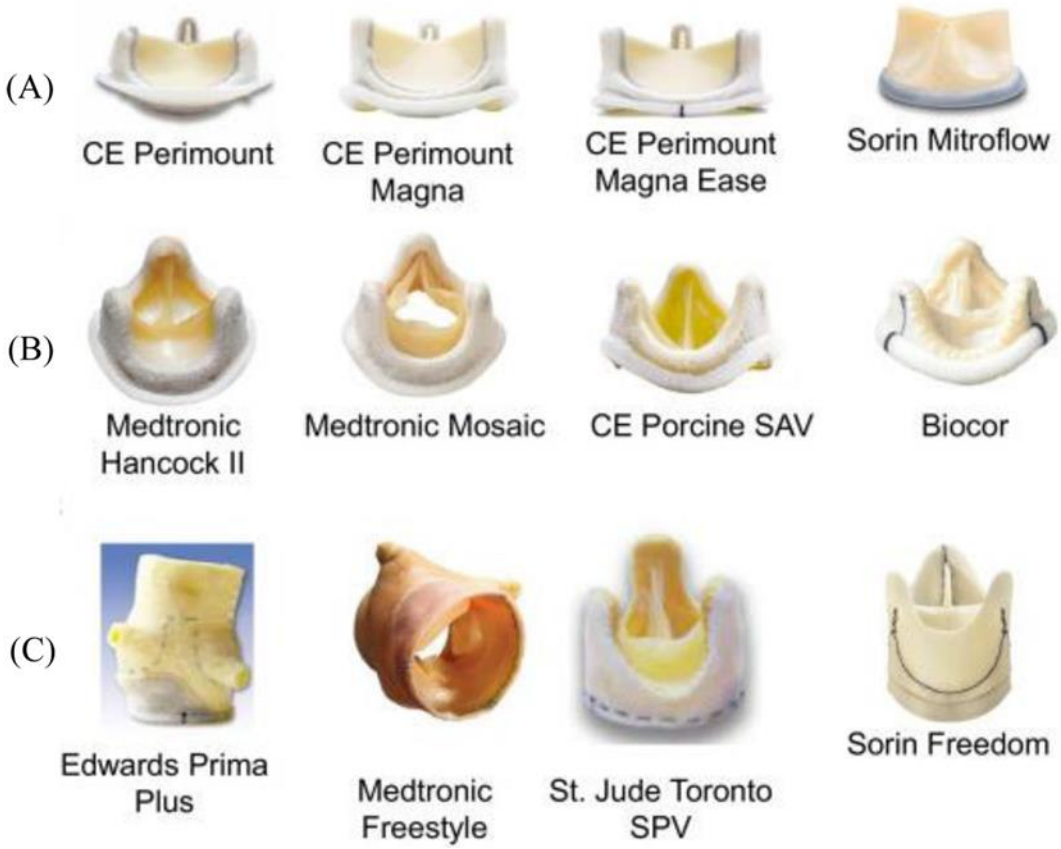

Figure 1.4: (A) Stented pericardial bovine bioprosthetic valves. (B) Stented porcine aortic valve bioprostheses. (C) Stentless bioprosthetic valves. CE = Carpentier-Edwards; SPV = stentless porcine valve, permission from (Piazza et al. 2011).

1.5 Transcatheter Aortic Valve Replacement

Current clinical trials are investigating outcomes of transcatheter aortic valve replacement (TAVR) among patient at intermediate-risk and low-risk of an open surgery (Carabello, 2011; Chakos et al., 2017; Coylewright, Forrest, McCabe, & Nazif, 2020; Daubert et al., 2017; Kheradvar et al., 2015; M. Leon et al., 2010; M. B. Leon et al., 2016; Linden, Leon, Smith, Mack, & Investigators, 2011). TAVR procedure is performed using one of the four different approach to access the aortic valve location: transfemoral, transapical, transaortic and transcarotid (Barbanti, Webb, Gilard, Capodanno, & Tamburino, 2017). A team of cardiologists will determine which

appropriate way to deliver the TAV into the calcified native aortic valve, however, the transfemoral approach is the most common way to deliver TAV. During the transfemoral approach, a small incision is made in the leg, and a catheter is inserted and traveled into the artery while the heart is beating. The team will guide the catheter and place it within the damaged valve. TAV can be delivered via chest for patients whom have vascular anatomy issues, transcarotid arterial access may be an alternative solution. Despite TAV industries use similar material leaflets as SAV, and therefore, TAV is expected to degenerate via similar mechanisms. However, TAVs design and implant configuration are totally different from SAVs (Thourani et al., 2015).

One of the most advantages of TAVR procedure is short recovery time (3-5 days) compare to SAVR which its recovery time about three months (Rodés-Cabau, 2012). Since TAVR was established, there has been more than 350,000 patient underwent TAVR procedure in 70 different countries (Webb et al., 2007). Currently, there are several designs of TAV that are commercially available as shown in Fig. 1.5. Even though, TAVR is less invasive procedure for patient with high risk of an open heart surgery with short recovery time, SAVR is still quite the golden standard for treating patient with aortic stenosis (Barbanti et al., 2017). TAVR is currently being investigated in a clinical trial among low risk patients of open heart surgery (Coylewright et al., 2020; Kodali et al., 2012; Sondergaard, 2016). Nevertheless, TAVs lack to more data in term of hemodynamic performance and its impact on the cardiac cycle, in contrary to SAVs.

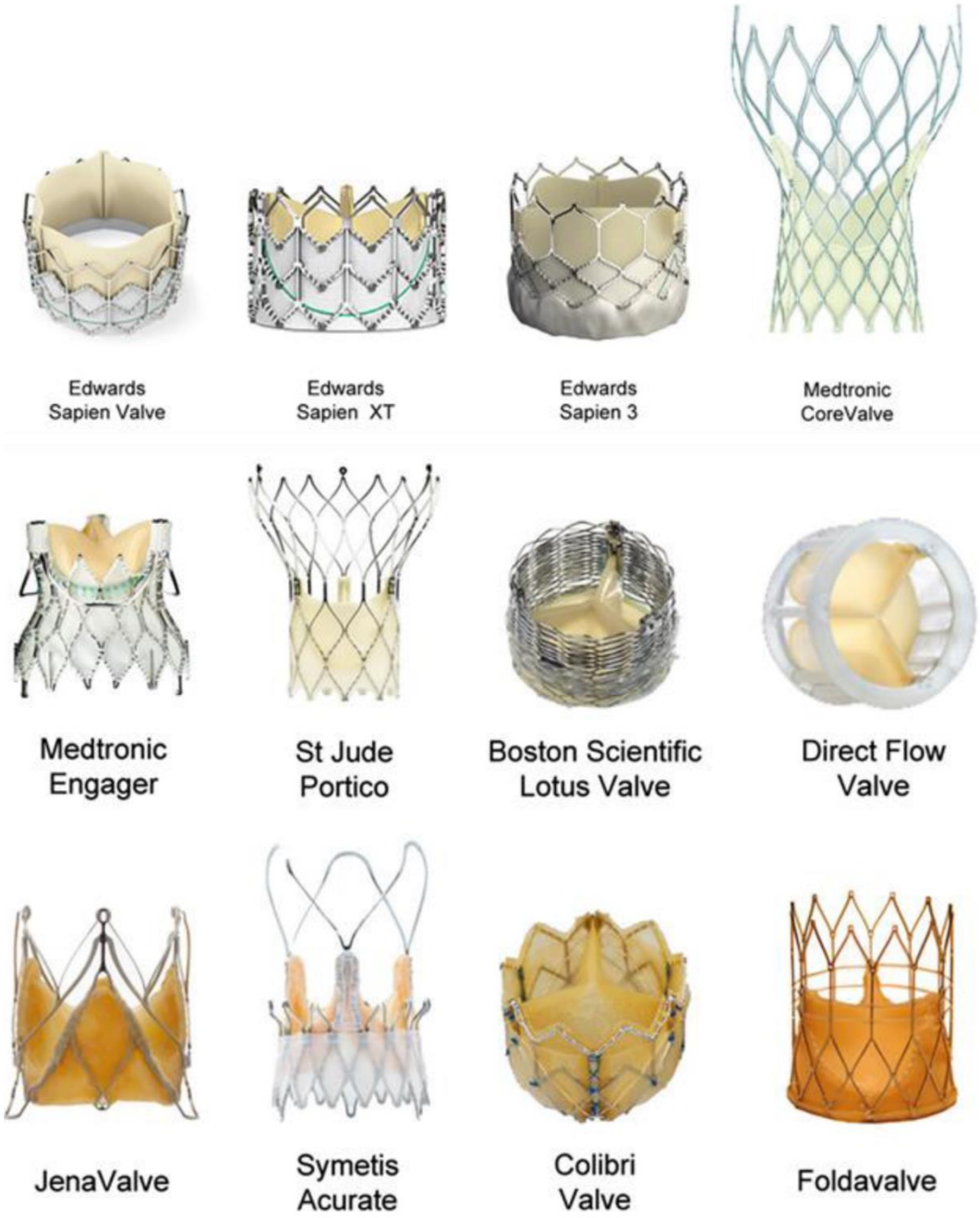

Figure 1.5: Different design configuration of TAVs devices that are currently available. permission from (Sondergaard, 2016).

1.6 Clinical issues associated with TAVR

1.6.1 Cerebral Embolisms

In the last decade TAVR has been introduced as a treatment option for patients with severe aortic stenosis. However, cerebral embolism complication was seen early as a potential clinical issue (Kheradvar et al., 2015). A published clinical data shows that there is no increase of stroke among patients who underwent TAVR vs surgical replacement (Adams et al., 2014; Makkar et al., 2012). Several magnetic respond imaging (MRI) studies (Arnold et al., 2010; Astarci et al., 2011; Ghanem et al., 2010; Hamm et al., 2013; Kahlert et al., 2009) have shown that cerebral embolism was observed in the majority of TAVR patients with a few days after the procedure. The issue of cerebral embolism could be originated from several places such as the native calcified valve or the aortic. Even with the use of a device to protect embolism from traveling to the brain, the majority of TAVR still show evidence of cerebral embolism (Lansky et al., 2015). To expand the use of TAVR to low-risk patient of aortic stenosis, the sources of cerebral emboli must be understood to prevent such an issue from occurring.

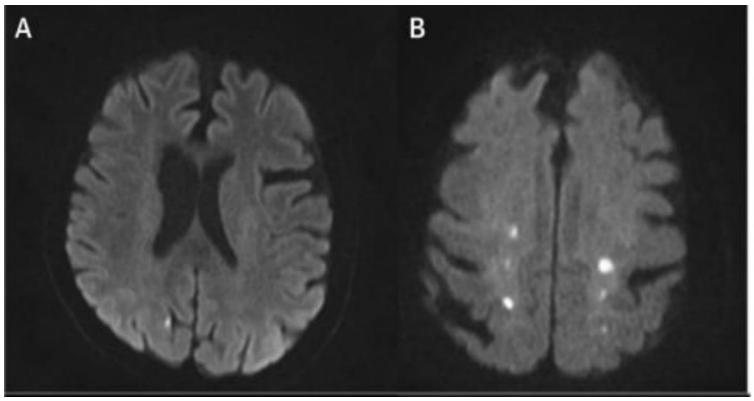

Figure 1.6: MRI results of 4 patients showing location of cerebral embolism without clinical stroke or TIA event. (A) single right embolus. (B) Multiple embolism in left and right of the brain. Permission from (Van Belle et al., 2016).

1.6.2 Reduced motion of TAV Leaflet

Another major clinical complication post-TAVR is that reduce leaflet motion has been reported in several clinical studies (De Marchena et al., 2015; Egbe et al., 2015; Leetmaa et al., 2015; Makkar et al., 2015; Van Belle et al., 2016). Reduced leaflet motion was detected among multiple bioprosthesis valves, including TAVs and SAVs. Additionally, valvular thrombosis was observed in patients following TAVR even days post the procedure (Akhras et al., 2016; De Marchena et al., 2015; Latib et al., 2015; Martí et al., 2015). A clinical study using 4-D volume computed tomography (CT) reported that valvular thrombosis has been found to be on the aortic surface of the valve leaflets and to the lesser extent of the ventricular surface (Del Trigo et al., 2016; Makkar et al., 2015). However, reduced leaflet motion is less among patients with surgical bioprosthesis (De Marchena et al., 2015; Egbe et al., 2015; Grunkemeier & Rahimtoola, 1990).

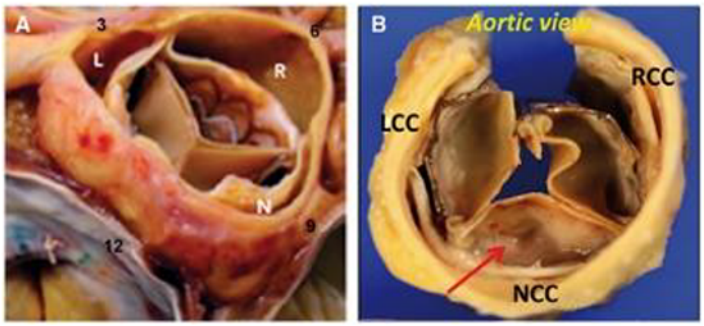

Figure 1.7: TAV device implanted over the native aortic valve. (A) TAV stent is surrounded around the native calcified aortic valve. Permission from (Brown, Park, Sundt, & Schaff, 2012). (B) The presence of thrombosis on the aortic surface of a SAPIEN valve following TAVR. Permission from (Krishnaswamy, Kapadia, & Tuzcu, 2012).

1.6.3 Paravalvular Leakage post-TAVR

Unlike surgical valve where a surgeon removed the calcified native or degenerated bioprosthetic valve, and replace it with a surgical valve, TAVR is implanted using a catheter to expand the TAV device over the calcified native valve or a degenerated bioprosthetic valve. Therefore, incomplete expansion of TAV, might lead to paravalvular leakage (PVL). The severity of PVL graded as mild, moderate and severe depending on the total volume of the leakage during TAV closure. Despite the possibility of measuring the volume of PVL, estimating the severity of PVL remains challenging. A clinical study has reported a mild PVL in 38% and moderate/severe in 9.1% of patients post-TAVR (De Marchena et al., 2015; Vahl, Kodali, & Leon, 2016). The rate of morbidity and mortality has been dramatically increased among TAVR patients due to PVL, even in mild PVL cases (Dencker et al., 2016; Rodés-Cabau, 2012). Clinically, it has been reported that moderate and severe PVL severity was seen more in self-expanded valve than balloon-expanded valve following TAVR (Gotzmann et al., 2012).

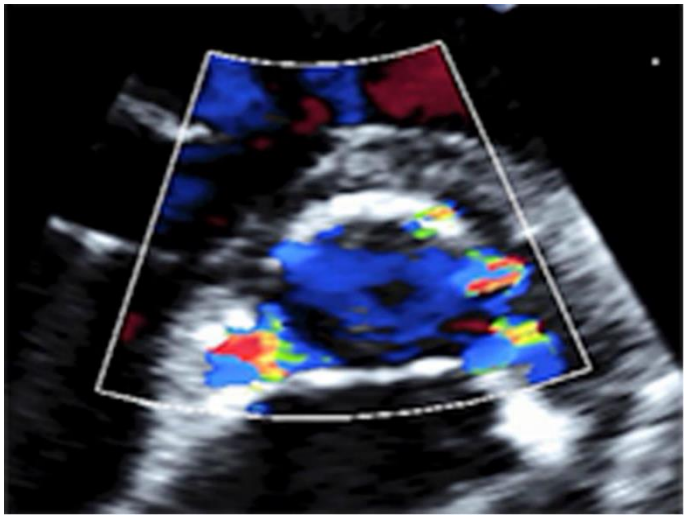

Figure 1.8: Echocardiography short axis view of SAPIEN 3 after one day of implementation. Permission from (Athappan et al., 2013)

1.7 Objectives

Fluid dynamics has been known to play a critical role in thrombotic and hemolytic complications associated with bioprosthetic aortic valves. Therefore, the first objective of this study was to characterize and measure hemodynamic performance of transcatheter aortic valves under physiological conditions. Previously, its well know that both high shear stress magnitude and exposure time is associated with blood elements damage and platelet activation. In the presence of high shear stress magnitude, the likelihood of blood clot and thrombosis formation increase leading to serious clinical complications. Additionally, computer simulations have been leading approach in the design and verification of bioprosthetic aortic valves, therefore the particle image velocimetry (PIV) images obtained from the experimental result will provide validation of computational fluid dynamic (CFD) results.

Reduced leaflet motion is increasingly recognized complication observed in a majority of TAVR patients even after short time of the implantation. Therefore, the second goal of this dissertation was to address the issue behind reduced leaflet motion post-TAVR. The study is aimed to explain the mechanisms behind valvular thrombosis on TAV leaflet surface. The hypothesis of this study is that since TAV is implanted within the native aortic valve or a degenerated surgical valve, that increase the chance of blood traps between the TAV outer surface and the native valve inner surface which increase the likelihood of thrombosis formation on TAV surface.

PVL is a common clinical complication post TAVR procedure. An accurate evolution of PVL severity is important for clinical decision. The current methodology to evaluate the severity of PVL is not validated experimentally, and it shows to over-estimate the severity of PVL. Accordingly, the third objective of this thesis was to validate the current guideline uses to evaluate PVL severity and developed a new methodology to assess the severity of PVL post-

TAVR based on fluid dynamics. The introduced approach is based on estimating the maximum momentum flux of PVL jets, using parameters that are currently being used to estimate the severity of PVL in clinic.

Energy loss is a well-established engineering concept that applied to evaluate the performance of native aortic valve and bioprosthetic aortic valve. Energy loss not only allows assessment of TAV performance during systole, but also allows quantification of PVL during diastole. The fourth objective of this study is to develop and validate a non-invasive procedure to estimate the energy loss during the cardiac cycle using doppler echocardiography. Additionally, energy loss is an excellent parameter to measure workload on the left ventricle due to PVL. In this study, we quantified the impact of PVL on the left ventricle experimentally.

The general objective of this thesis was to develop a better understanding of the performance of TAV devices and comparing it with the surgical bioprosthetic which considered to be the golden treatment option for severe aortic stenosis patients. Additionally, developing and validating new methods to estimate the severity of PVL following TAVR will save millions of TAVR patients, and to quantify the overall performance of TAVs during the cardiac cycle.

Chapter 2: Fluid Dynamics Characterization of Transcatheter Aortic Valves Using Particle Image Velocimetry

2.1 Introduction

Aortic stenosis due to degenerative calcific aortic valvular disease is the main reason for aortic valve replacement in developed countries (Kobayashi, Giri, Vallabhajosyula, Herrmann, & Jagasia, 2015). In developing countries, conversely, rheumatic disease is a common cause of valvular heart disease (Iung et al., 2003; Organization, 2004). Each year, more than 67 500 surgical aortic valve replacements (SAVRs) are performed in the United States, and over 275 000 are done worldwide (Clark et al., 2012; Rajamannan et al., 2011; Sliwa et al., 2009). The number of patient with aortic valve disease is expected to triple by 2050 due to aging populations and high incidence of rheumatic heart disease in developing countries (Association, 2002; Nkomo et al., 2006; Takkenberg et al., 2008; Yacoub & Takkenberg, 2005). Traditionally, the risks of lifelong anticoagulation therapy after surgical implantation of mechanical heart valves were evaluated against the risks of bioprosthetic valve structural deterioration and possible reoperation. Due to the promising improvements in the long-term durability of surgical bioprostheses, bioprosthetic heart valves have been recently implanted in more than 90% of patients who are over sixty years old to avoid lifelong anti-coagulation treatment (De Santo et al., 2012; Egbe et al., 2015). In addition to SAVR, transcatheter aortic valve replacement (TAVR) has emerged as a safe and effective alternative treatment option for patients with severe symptomatic aortic stenosis deemed at high and intermediate risk for SAVR(Adams et al., 2014; Isaacs, Shuhaiber, Salemi, Isom, & Sedrakyan, 2015; Smith et al., 2011). The possibility of redo transcatheter valve-in-valve implantation has also contributed to the shift toward the use of bioprostheses in patient

(Azadani & Tseng, 2010, 2011; M. B. Leon et al., 2016). Consequently, most patients who undergo aortic valve replacement currently receive either surgical or transcatheter bioprosthetic aortic valves.

Unlike surgical stented bioprosthetic heart valves where leaflets are sutured to a frame mounted on a sewing ring, TAV leaflets are attached to a stent which can be expanded within the annulus. The lack of a sewing ring in TAVs can lead to a larger valve area compared to surgical bioprostheses following full expansion of the TAV stent to its nominal size. As a result, clinical measurements of transvalvular pressure gradients and effective orifice area have been shown that TAVs match and may even exceed the systolic hemodynamic function of surgical stented bioprostheses (Daubert et al., 2017; Dvir et al., 2014; Hahn et al., 2013). Although, in-depth investigation of the flow field structures in TAVs using quantitative measurement techniques such as particle image velocimetry is of interest to examine the flow-field characteristics (Clavel et al., 2009; Stühle et al., 2011). In addition, the experimental data provide evidence necessary for verification and validation of computational models of bioprosthetic heart valves. Computational modeling and simulations are becoming increasingly accepted component in design and verification of medical devices in the past few years (Dasi, Simon, Sucosky, & Yoganathan, 2009). Therefore, the goal of our study was to determine flow field characteristics of the two commercially available TAV devices, Edwards SAPIEN 3, and Medtronic CoreValve, during systole and compare it with that of a commonly used surgical bioprosthesis, Carpentier-Edwards PERIMOUNT Magna valve, using phase-locked particle image velocimetry (PIV) measurements.

2.2 Material and Method

2.2.1 Transcatheter Aortic Valve

Edwards SAPIEN Transcatheter Heart Valve (Edwards Lifesciences) and Medtronic CoreValve (Medtronic, Minneapolis, MN, USA) have been widely used in clinical trials and clinical practice. Edwards SAPIEN valve consists of a balloon-expandable stent and bovine pericardial leaflets. Conversely, Medtronic CoreValve is constructed from a self-expanding nitinol stent and porcine pericardial leaflets. Both devices were granted CE Mark approval for commercial use in Europe in 2007. In addition, the U.S. Food and Drug Administration approved the indication for the systems to include treatment of patients with severe aortic stenosis at high and intermediate risk for surgery. In this study, detailed flow-field characteristics of 26-mm Edwards SAPIEN 3 and 26-mm Medtronic CoreValve were determined and compared with that of a 25-mm surgical Carpentier-Edwards PERIMOUNT Magna aortic heart valve (Edwards Lifesciences Fig. 1)

2.2.2 Experimental Setup

A custom-built pulse duplicator system (BDC Labs, Wheat Ridge, CO, USA) was used for testing the three bioprosthetic heart valves (Fig. 2). Heart rate and cardiac output were control parameters for a virtual LabVIEW pulse-signal-generator that controls a servo pump system. Each stroke of the pump's piston changes the pressure surrounding a compliant silicone ventricle, causing ejection through the aortic valve. Custom-made silicone washers (outer diameter 40 mm, inner diameter labeled size of the bioprostheses, and thickness 10 mm) were employed to mount the bioprosthetic valves. The Carpentier-Edwards PERIMOUNT Magna bioprosthesis was placed on the top of the silicone washer and sutures were passed through the sewing ring to hold the valve in place. In addition, the two TAVs were placed within the custom-made silicone washers, so that the bottom of the TAV frame (stent) was at the same level as the bottom of the silicone

washer. A bileaflet mechanical heart valve was placed on the other side of the silicone ventricle in the mitral valve position. The pulse duplicator input parameters matched the international standard ISO 5840: 2015 recommendations for testing prosthetic heart valves; that is, heart rate of 70 beats/min, mean atrial and aortic pressures of 10 and 100 mmHg, and cardiac output of 5 L/min. The physiological flow condition was simulated by controlling peripheral resistance in the pulse duplicator and local compliance using two compliance chambers downstream of the aortic valve. Recirculating fluid of 45% by volume glycerin solution (99% The Science Company, Denver, CO, USA) in phosphate buffered normal saline solution (Research Products International, Mount Prospect, IL, USA) was used as a blood analog fluid. The running solution has a viscosity of 3.45 cP, a density of 1.12 g/cm^3, and a refractive index of 1.39 at 37 °C. Pressure was measured in the aorta and left ventricle using strain gauge pressure transducers (Utah Medical Products, Midvale, UT, USA) embedded inside the pulse duplicator 35 mm upstream and 105 mm downstream of the bio-prostheses. The pressure transducers were calibrated prior to the tests using Delta-Cal Pressure transducer simulator/tester (Utah Medical Products, Inc). In addition, an electromagnetic flowmeter (Model 501, Carolina Medical Electronics Inc, East Bend, NC, USA) was used to measure flow rate in the system. Moreover, motion of the leaflets was captured using a high-speed camera (Sony DSC-RX10M3) placed on top of the aortic valve at rates of 480 and 960 frames per second.

2.2.3 Particle Image Velocimetry

A conventional two-dimensional PIV system (TSI, Inc., Shoreview, MN, USA) was used to obtain planar velocity measurements downstream of the bioprosthetic valves. Illumination was supplied by a dual oscillator Nd:YAG laser (Litron Lasers Nano S 15 Hz) and lasers were synchronized using a Laser Pulse Synchronizer (TSI, model 610035, TSI Inc.). Silver coated hollow glass particles (8 μm diameter, TSI, model 10089-SLVR) were used to visualize the flow.

Images were recorded with a 1600 × 1200-pixel resolution cross correlation CCD camera (Power View Plus 2MP, TSI, model 630157), capable of capturing PIV image pairs at 30 frames per second. For PIV measurement, the camera was fitted to a NIKKOR lens (50 mm f/1.8D) and a narrow band interference filter was utilized to reduce reflections. The spatial resolution for the Magna surgical bioprosthesis, CoreValve, and SAPIEN 3 was 58.96 μm/pixel, 62.29 μm/pixel, and 56.29 μm/pixel, respectively. Phase-locked measurements were acquired by triggering the PIV system from the pulse generator driving the piston pump, over 91-time instances regularly spaced over the entire cardiac cycle. All images were correlated on a recursive Nyquist grid using a 50% overlap with a final pass interrogation window of 24 × 24 pixels. The final interrogation size was selected to have a careful balance between the highest resolution and the signal-to-noise ratio of the cross correlations. Data was processed using INSIGHT 3G TM software from TSI. For simple nondeforming solid boundaries, such as straight pipes, calibration codes can be applied to the PIV measurements to re-move the optical distortion caused by the refractive index mismatch between the working fluid and the valve-mounting chamber. For calibration, a plate with a regular pattern of markers was placed in the field of view along the bioprosthetic centerline. The image was then used to define the scale and determine the image distortion in both radial and axial directions. Subsequently, a correction function was determined and a calibration MATLAB code was applied to the PIV measurements to remove the optical distortion caused by the mismatch of the refractive index of the working fluid and that of the straight cylindrical pipe (Stewart et al., 2013). After obtaining the velocity field, Tecplot software (Tecplot Inc., Bellevue, WA, USA) was adopted to obtain instantaneous viscous shear stress from the measured 2D velocity gradient using Newton's law of viscosity.

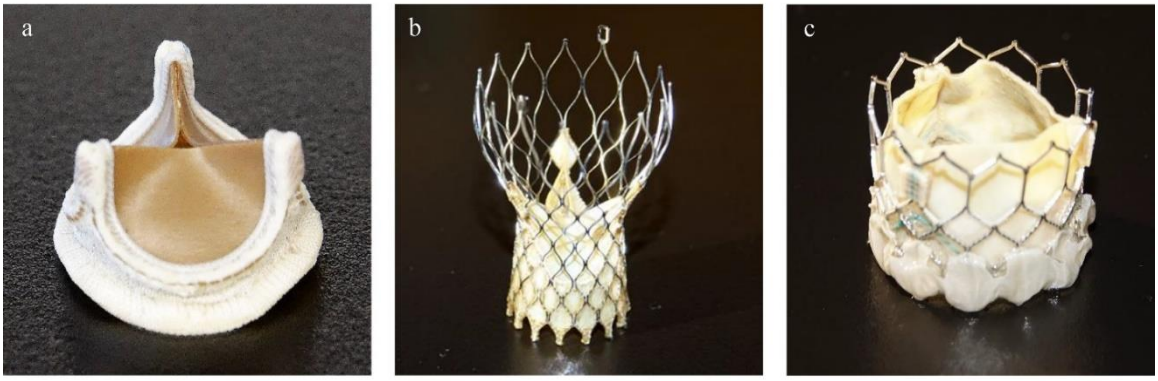

Figure 2.1: (a) 25-mm surgical Carpentier-Edwards PERIMOUNT Magna bioprosthetic aortic valve. (b) 26-mm self-expanding Medtronic CoreValve. (c) 26-mm Edward SAPIEN 3 transcatheter heart valve. Adopted from (Vahidkhah, Barakat, et al., 2017).

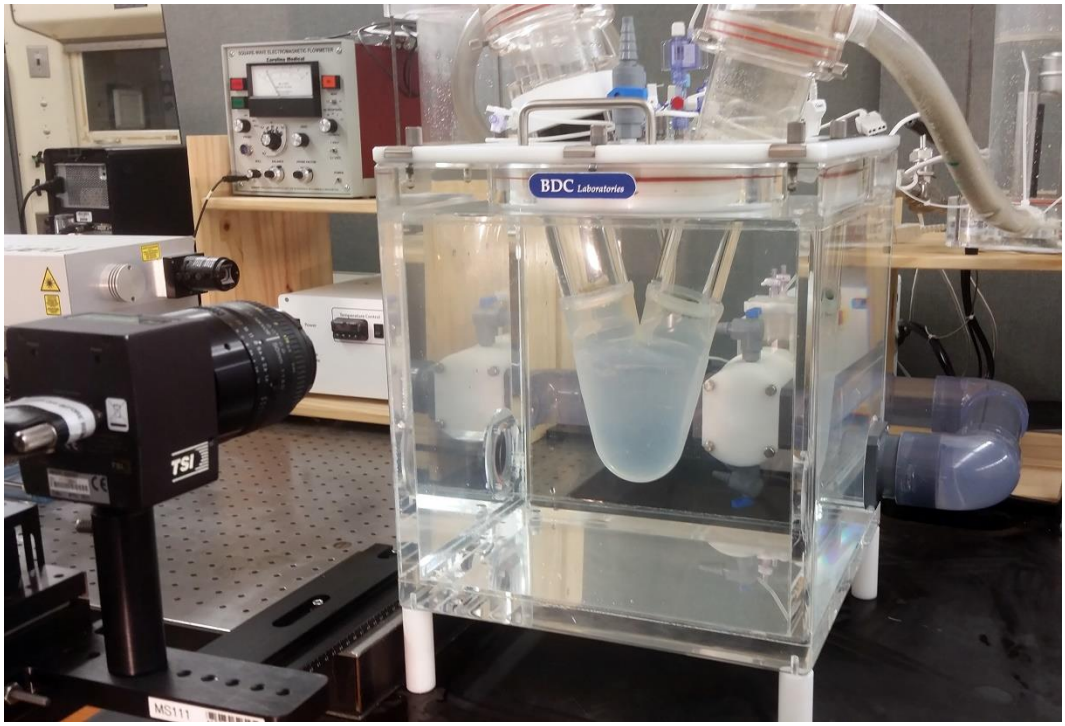

Figure 2.2: Custom-built pulse duplicator system and PIV setup.

2.3 Result

2.3.1 Hemodynamics performance of the valves

The raw pressure and flow waveforms obtained from the three bioprosthetic heart valves in the pulse duplicator are shown in Fig. 2.3. The 25-mm Carpentier-Edwards PERIMOUNT Magna bioprosthesis had a mean pressure gradient of 8.6 ± 0.07 mm Hg (Fig. 2.3a). In addition, the effective orifice area of the bioprosthesis was 1.7 ± 0.03 cm2. The effective orifice area was calculated based on the Gorlin equation. The 26-mm CoreValve, conversely, had a mean pressure gradient of 7.5 ± 0.16 mm Hg and an effective orifice area of 1.72 ± 0.03 cm2 (Fig. 2.3b). In addition, the 26-mm SAPIEN 3 had a mean pressure gradient of 6.2 ± 0.052 mm Hg (Fig. 2.3c). The effective orifice area of the Edwards SAPIEN 3 bioprosthesis was 2.0 ± 0.06 cm2. Moreover, leaflet motion of the three bioprosthetic heart valves captured by the highspeed camera is shown in the Supporting Information videos.

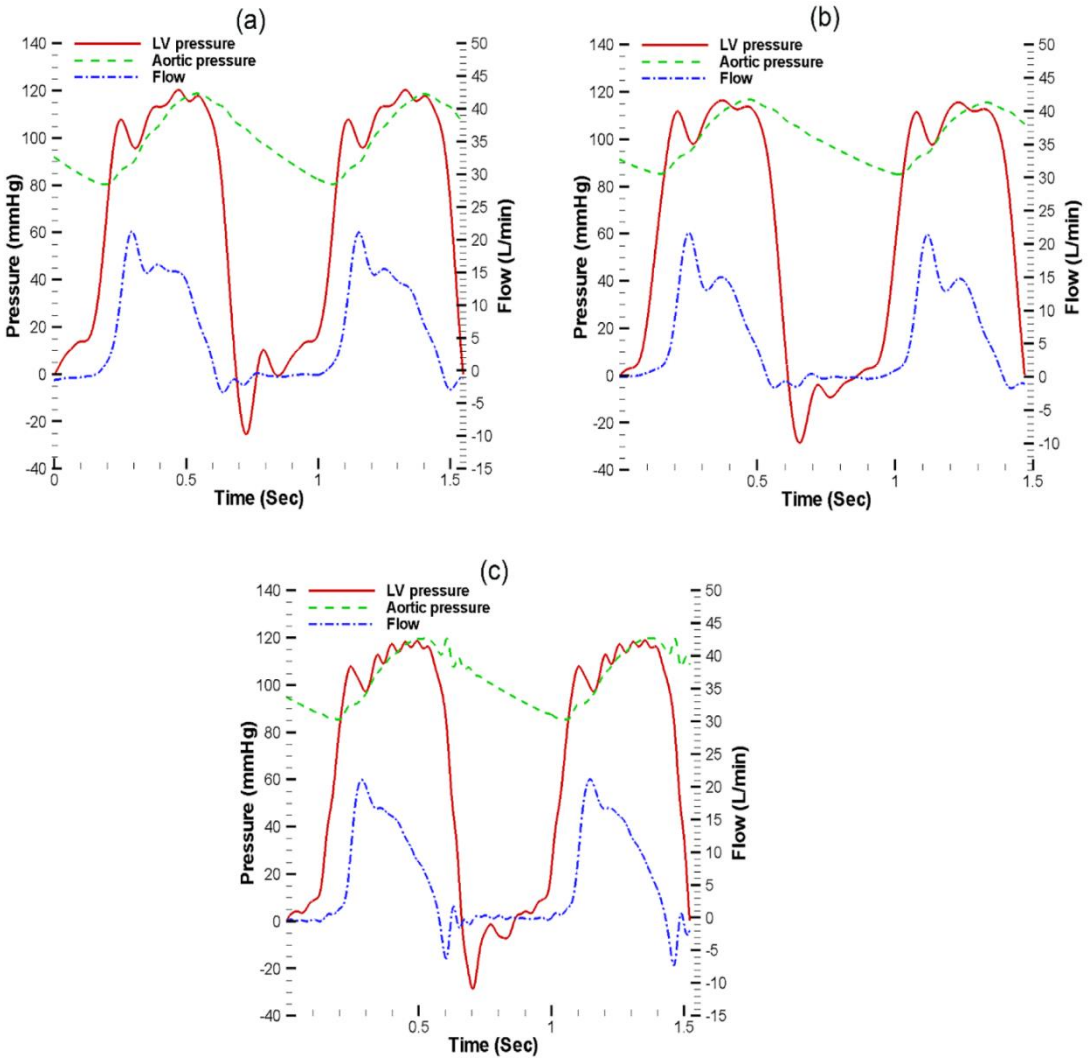

Figure 2.3: In vitro pressure and flow waveforms of (a) 25-mm surgical Carpentier-Edwards PERIMOUNT Magna bioprosthetic aortic valve, (b) 26-mm self-expanding Medtronic CoreValve, and (c) 26-mm Edward SAPIEN 3 transcatheter heart valve.

2.3.2 PIV Results of Surgical valve

Instantaneous velocity vectors and viscous shear stress values of the 25-mm Carpentier-Edwards PERIMOUNT Magna bioprosthesis are presented in Fig. 2.4. The time intervals presented in the figure correspond to five different phases within a cardiac cycle, namely, acceleration, peak flow, deceleration, early-diastole, and mid-diastole. In the acceleration phase, a highly axial flow velocity was observed along the bioprosthetic centerline (Fig. 2.4a). At the peak of flow, a maximum jet velocity of 2.1 m/s was measured in the center of the jet (Fig. 2.4b). The jet diameter at the peak of flow was approximately 15.2 mm. The velocity decreased abruptly from the strong central jet to the surrounding region. During deceleration phase, velocity of the jet at the core was decreased to 1.2 m/s (Fig. 2.4c). Furthermore, significantly lower velocity magnitudes were observed after the valve closure both in early- and mid-diastole (Fig. 4d,e). In addition to the velocity field, Fig. 2. 4 demonstrates viscous shear stress fields throughout one cardiac cycle. At the peak of the flow, maximum viscous shear stress was 4 N/m^2 and occurred along a significant portion of the jet boundary layer (Fig. 2.4b). During deceleration phase and in the diastole, however, viscous shear stress was significantly lower than the magnitudes observed at the peak of the flow (Fig. 4c–e)

2.3.3 PIV Results of CoreValve

Velocity and viscous shear stress fields of the 26-mm Medtronic CoreValve are presented in Fig. 2.5. During the acceleration phase, as presented in Fig. 2.5a, PIV measurements showed an accelerating axial flow along the valve centerline. At peak of the systole, a maximum velocity of 2.2 m/s was measured in the center of the jet (Fig. 2.5b). The diameter of the jet velocity was approximately 11.3 mm, which was smaller than that of the PERIMOUNT Magna bioprosthesis. During the deceleration phase, velocity magnitude considerably dropped as shown in Fig. 2.5c. In addition, even lower velocity magnitudes were observed during the diastole after the valve

closure. (Fig. 2.5d,e). In addition to the velocity field, Fig. 2.5 illustrates viscous shear stress magnitude throughout the five phases of one cardiac cycle. At the peak of flow, maximum viscous shear stress was 4 N/m^2 (Fig. 2.5b). However, due to the relatively wider jet boundary layer in CoreValve compared to the PERIMOUNT Magna valve, the overall magnitude of the viscous shear stress at the peak of flow was lower in the CoreValve than the PERIMOUNT Magna bioprosthesis. During the deceleration phase and during diastole, the maximum viscous shear stress magnitude was significantly lower than the peak of the flow as presented in (Fig. 2.5c–e). Local pockets of elevated viscous shear stress were found within the flow field downstream of the bioprosthesis

2.3.4 PIV Results of SAPIEN 3

In addition, Fig. 2.6 shows instantaneous velocity vectors and viscous shear stress field of the 26-mm Edwards SAPIEN 3 bioprosthesis. The first image row shows the acceleration phase, in which an accelerating axial flow can be clearly observed along the bioprosthetic centerline (Fig. 2.6a). After 40 ms, at the peak of flow, a strong jet with a maximum velocity of 1.9 m/s was observed (Fig. 2.6b). The jet diameter was approximately 20.9 mm, which was more than the Medtronic CoreValve and PERIMOUNT Magna bioprosthesis. During the deceleration phase, as shown in Fig. 2.6c, velocity of the central jet decreased to 1.3 m/s. Furthermore, significantly lower velocity magnitudes were observed in the early- and mid-diastole following the closure of the bioprosthesis (Fig. 2.6d,e). In addition, Fig. 2.6 shows viscous shear stress magnitudes that were obtained from the velocity field throughout one cardiac cycle. In the peak flow, maximum viscous shear stress was 4 N/m^2 and occurred at the jet boundary layer (Fig. 2.6b). However, the overall magnitude of the viscous shear stress at the peak of flow within the jet boundary layer was lower in the SAPIEN 3 than the PERIMOUNT Magna bioprosthesis.

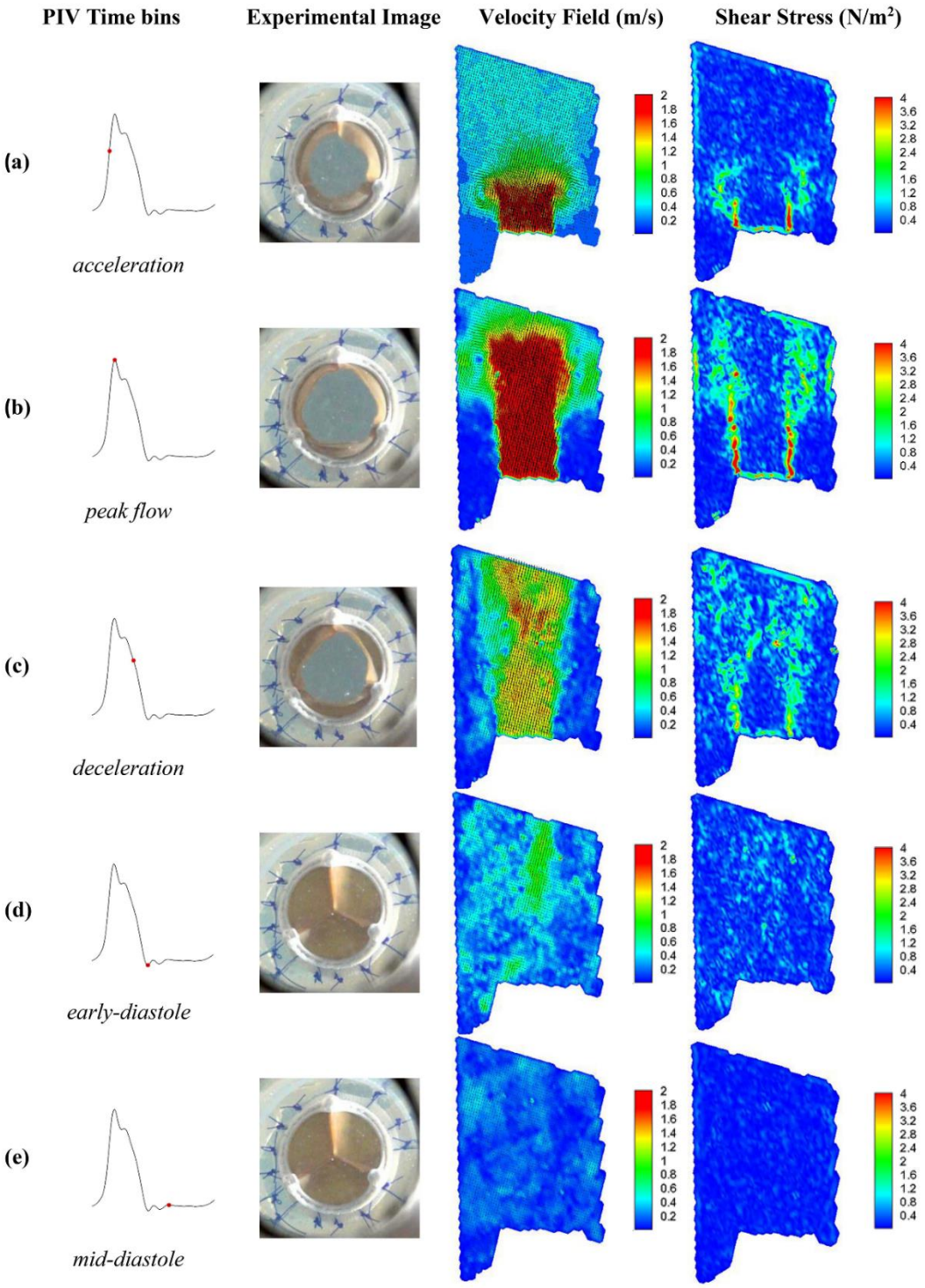

Figure 2.4: Instantaneous velocity and viscous shear stress fields of 25-mm surgical Carpentier-Edwards PERIMOUNT Magna bioprosthesis in various phases of a cardiac cycle.

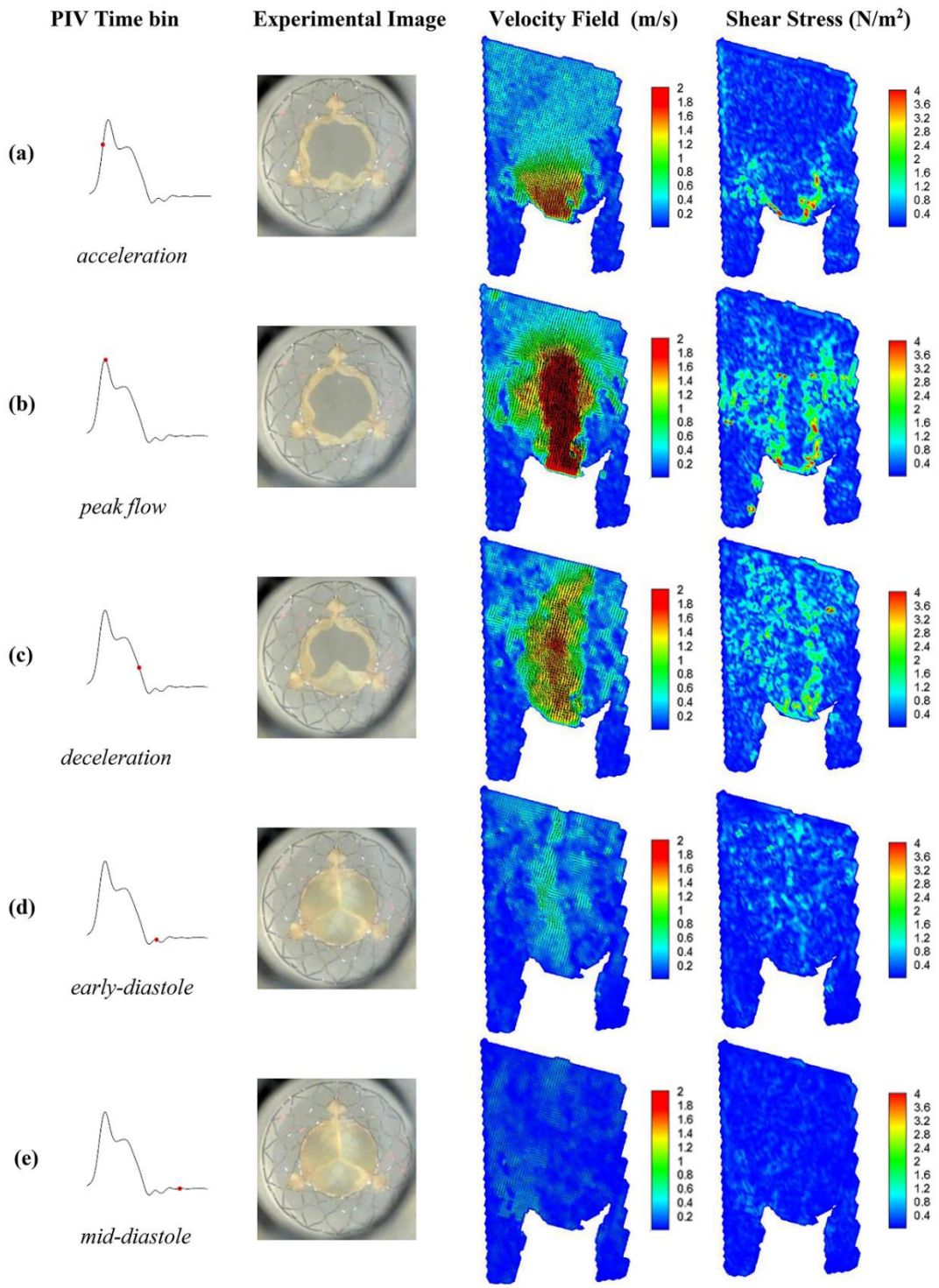

Figure 2.5: Instantaneous velocity and viscous shear stress fields of 26-mm Medtronic CoreValve in various phases of a cardiac cycle.

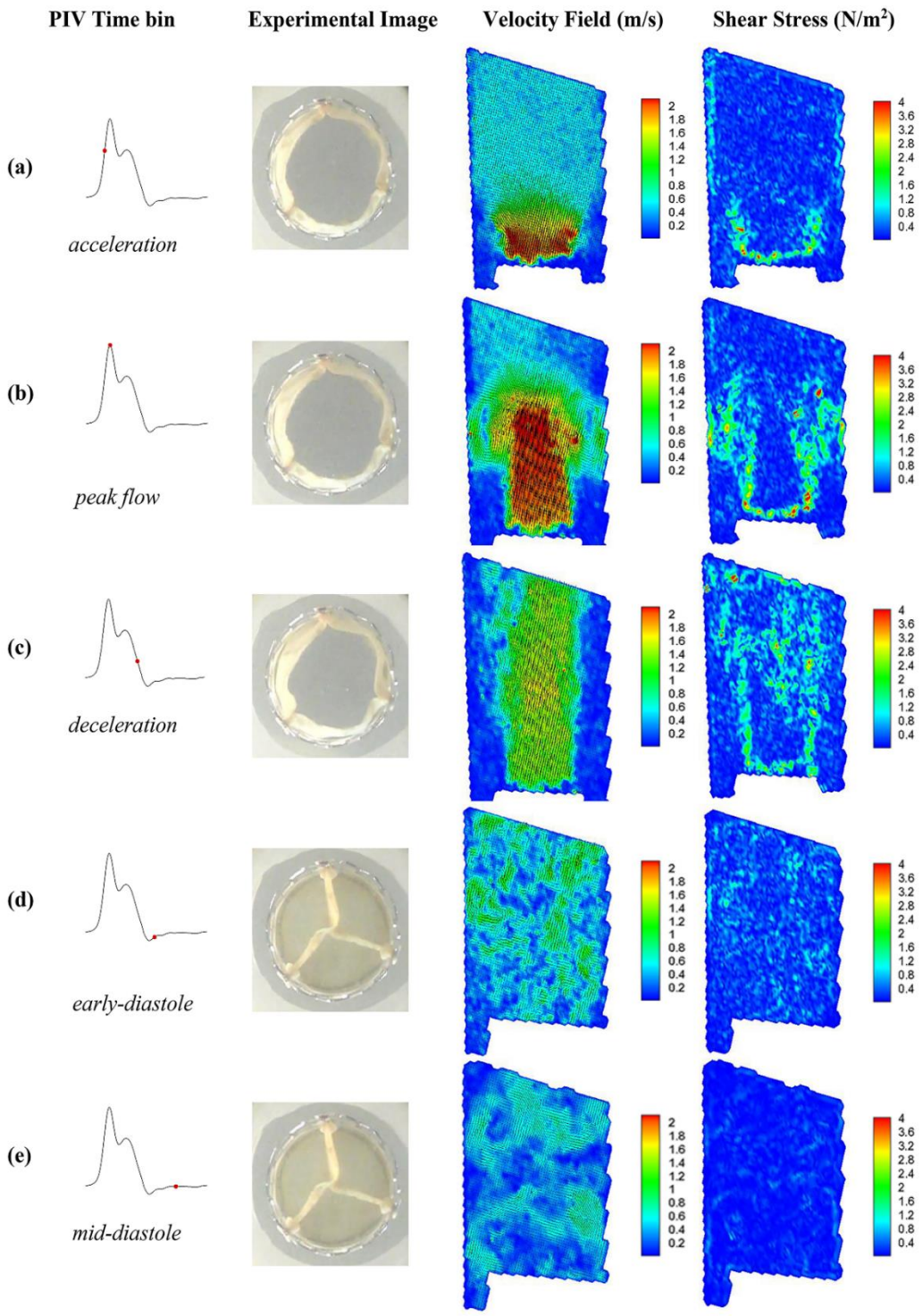

Figure 2.6: Instantaneous velocity and viscous shear stress fields of 26-mm Edwards SAPIEN 3 in various phases of a cardiac cycle.

2.4 Discussion

2.4.1 Summary

In this study, we determined flow field characteristics of the two commercially available and commonly used TAVs, Edwards SAPIEN 3, and Medtronic CoreValve, using phase-locked PIV measurements and compared the results with that of a commonly used surgical bioprosthesis, Carpentier Edwards PERIMOUNT Magna bioprosthesis. The overall systolic hemodynamic performance of the 26-mm Medtronic CoreValve and 26-mm Edwards SAPIEN 3, in terms of the mean transvalvular pressure gradient and effective orifice area, was slightly superior to that of the 25-mm Carpentier-Edwards PERIMOUNT Magna bioprosthesis. The observation was consistent with the clinical hemodynamic measurements of the bioprostheses (Barakat, Dvir, & Azadani, 2018; Külling et al., 2017). Due to the lack of sewing ring in TAVs, TAV devices offer a larger orifice area than comparable size surgical bioprostheses after full expansion of the TAV stent to its nominal size. In addition, the maximum viscous shear stress magnitude within the jet boundary layer at the peak of the flow was higher in PERIMOUNT Magna than CoreValve and SAPIEN 3 bioprostheses. In addition, the velocity jet diameter was relatively narrower in the Medtronic CoreValve than SAPIEN 3 and PERIMOUNT Magna, which was due to the conical inflow section of the CoreValve. The velocity measurements were comparable with majority of previous studies using 2D PIV to obtain velocity profiles of surgical bioprosthetic valves (Raghav et al., 2016; Spethmann et al., 2012)

2.4.2 Fluid Dynamics Impact on Thrombotic and Hemolytic

Fluid dynamics has been known to play a critical role in thrombotic and hemolytic complications associated with prosthetic heart valves (Dasi et al., 2009; Moore & Dasi, 2015). Thromboembolic events due to hemolysis and shear-induced platelet activation have been correlated to high shear stress regions in the blood flow (Becker, Eisenberg, & Turpie, 2001;

Vahidkhah et al., 2016; Yoganathan, He, & Casey Jones, 2004). The true shear force experienced by blood cells is caused by viscous shear stress than Reynolds shear stress in the presence of turbulence (Alemu & Bluestein, 2007; Ge, Dasi, Sotiropoulos, & Yoganathan, 2008). It is well known that both shear stress magnitude and exposure time are important in activation of blood cell elements. The higher the exposure time, the lower would be the stress threshold level for blood cell impairment. The shear stress magnitude of 150 N/m^2 is known to be the threshold under which no red blood cell damage has been observed regardless of the exposure time (Jones, 1995). In the current study, the measured viscous shear stress downstream of the three bioprostheses was significantly below the threshold level for red blood cell damage reported in the literature. Conversely, shear-induced platelet activation occurs at significantly lower shear stress values. Hung et al in (Leverett, Hellums, Alfrey, & Lynch, 1972) reported platelet damage at 10–16.5 N/m^2 for an exposure time of 102 s, while Williams (Hung, Hochmuth, Joist, & Sutera, 1976) found a threshold of 13 N/m^2 for exposure time levels of 10^{-3} s. In addition, Ramstack et al (Williams, 1974) reported platelet activation at a somewhat higher threshold of 30–100 N/m^2 with an exposure time of 10^{-2} – 10^{1} s. The measured shear stress values in the three bioprosthetic heart valves examined in this study were significantly below platelet activation threshold reported in the literature. As a result, the predominant mechanism of platelet activation in the bioprosthetic heart valves will likely be as a result of blood contact with foreign surfaces of bioprostheses than shear-induced platelet activation.

2.4.3 Validation of CFD Simulation

In vitro experimental testing has been an integral part of design verification and optimization of medical devices. In the past few years, the role of computational modeling and simulations in design and verification of prosthetic heart valves is becoming more and more important (Ramstack, Zuckerman, & Mockros, 1979). The U.S. Food and Drug Administration

(FDA) and EU Medical Device Regulatory System are major driving forces behind the trend (Dwyer et al., 2009; Hsu et al., 2015; Morris et al., 2016; Oberkampf, Trucano, & Hirsch, 2004; Sirois & Sun, 2011; Stewart et al., 2012). A combined experimental and computational approach should be considered to shed light on the flow-mediated mechanisms of thrombosis in bioprosthetic aortic valves. For instance, regions of blood stagnation provide an opportunity for platelets and blood proteins to accumulate to critical concentrations leading to thrombosis (Anning, 1957; Bluestein, Niu, Schoephoerster, & Dewanjee, 1997; Friedrich & Reininger, 1995; Goodman, Barlow, Crapo, Mohammad, & Solen, 2005; Karino & Goldsmith, 1979; Reininger, Reininger, Heinzmann, & Wurzinger, 1995; Tan et al., 2012). Contrary to SAVR where native calcified leaflets are removed from the annulus during open heart surgery, TAVs are implanted within native valves in TAVR procedures. As a result, the aortic portion of the TAV stent is circumferentially surrounded by the calcified native valves in TAVR. This configuration is more pronounced in TAVs that tend to operate inside the annulus such as SAPIEN valves compared to supra-annular TAVs such as CoreValve. The geometric confinement of TAVs disturbs the natural flow field between the leaflets and aortic sinuses, increases the blood residence time (stasis) on the leaflets, and consequently increases the likelihood of thrombogenesis on the TAV leaflets (Sukavaneshvar, 2017; Vahidkhah, Abbasi, et al., 2017; Vahidkhah & Azadani, 2017; Vahidkhah, Barakat, et al., 2017; Vahidkhah, Javani, et al., 2017). Remarkably, leaflet thrombosis is more commonly observed in TAVR than SAVR (Midha et al., 2017). In addition, the majority of the reported cases of leaflet thrombosis occurred after using TAVs with intra-annular design, such as Edwards SAPIEN and St. Jude Portico valves (Córdoba-Soriano et al., 2015; Mack & Holmes, 2016; Makkar et al., 2015).

2.4.4 Study Limitation

In this study, a conventional 2D PIV system was used to obtain planar velocity measurements downstream of the three bioprosthetic heart valves. In 2D PIV measurements, the third component of velocity vector cannot be measured. However, since the axial jet velocity is of such great magnitude during the systole, the third component of the velocity vector is insignificant. Therefore, the 2D PIV measurements accurately approximate the total viscous shear stress values in the jet boundary layer during the systole. In the diastole, however, flow is three-dimensional, rotational, and spatially inhomogeneous. Therefore, other PIV methods, such as stereo-PIV and tomographic-PIV, should be utilized to measure the three components of velocity vectors. Another limitation of this study was the lack of aortic sinus and coronary flow in the pulse duplicator system. However, we believe that the limitations of the currently available in vitro experimental setups that attempt to model the aortic root geometry justify the use of the simplified geometry of the present work. For instance, in the currently available pulse duplicator systems, the aortic root does not represent a patient specific geometry, the root compliance and coronary arteries are nonexistent, and in the cases that include these properties, the resistance of coronary arteries cannot be accurately adjusted. As a result, using a simplified geometry facilitates the validation process of computational works during systole which was one of the main objectives of this study.

2.5 Conclusion

A comprehensive evaluation of velocity and viscous shear stress fields downstream of three commonly used bioprosthetic heart valves was performed using 2D particle image velocimetry measurements. The in vitro experiments showed that hemodynamic characteristics of the 26-mm SAPIEN 3 and 26-mm CoreValve were comparable to the 25-mm PERIMOUNT Magna surgical bioprosthesis. Maximum viscous shear stress was observed at the peak of flow during the systole within the jet boundary layer in all the three bioprostheses. The measured shear stress values were below the known threshold for red blood damage and platelet activation. Therefore, shear-induced damage to red blood cells and platelet activation are unlikely to take place during systole in all the three bioprosthesis. Despite the limitations described previously, PIV measurements can also be used for verification and validation of computational simulation.

Chapter 3: Valve Thrombosis Post Transcatheter Aortic Valve Replacement: Significance of blood Stasis on the Leaflets

3.1 Introduction

Transcatheter aortic valve replacement (TAVR) is a promising treatment for patients with severe aortic valve stenosis whom at high risk of an open-heart surgery. Reduced leaflets motion due to valvular formation have been increasingly a major complication post TAVR patients (De Marchena et al., 2015; Egbe et al., 2015; Leetmaa et al., 2015; Makkar et al., 2015). In addition, reduced leaflets motion has been observed among patients following valve-in-valve (ViV) procedures (Akhras et al., 2016; De Marchena et al., 2015; Latib et al., 2015; Martí et al., 2015). Thrombosis formation was mostly found on the surface of the aortic valve leaflets and on the ventricular surface (Del Trigo et al., 2016; Makkar et al., 2015). Anticoagulation and antithrombotic therapies are used to prevent thrombosis formation post-TAVR, however a further investigation is required to determine and manage the mechanisms of thrombosis formation post-TAVR. Currently, the management of TAVR depends on history, outcomes, and treatment responses of SAVR (De Marchena et al., 2015). Thrombosis formation post-SAVR is relatively low 0.03-1.46% (De Marchena et al., 2015; Egbe et al., 2015; Grunkemeier & Rahimtoola, 1990). Nevertheless, the assessment of bioprosthetic surgical leaflets motion are not normally done after SAVR, therefore, the frequency might be underestimated. In contrast to SAVR patients, the occurrence of reduced leaflets motion due to thrombosis formation among TAVR/ViV may be

high 40% as reported in a published clinical trial (Brown et al., 2012). The mechanisms beyond leaflet thrombosis in TAVR/ViV patients still unclear. Therefore, it is important to investigate the essential factors causing the valvular thrombogenesis post-TAVR/ViV procedure.

In this study, we investigate to address the source of leaflet thrombosis post-TAVR/ViV. In TAVR/ViV procedures, a transcatheter aortic valves (TAVs) are implanted within the native calcified aortic valve or a degenerated bioprosthetic valve. Therefore, the aortic stent frame portion is circumferentially surrounded by the native calcified valve in TAVR setting, or by the leaflets of the degenerated bioprostheses in ViV setting as it shown in (Fig 3.1). this implementation configuration is more present with TAVs which tend to place within the annulus than super-annular TAVS. In this study our theory is that the longer blood resident time (BRT) on the aortic surface of TAV leaflets because of the annulus surrounded TAV frame, might lead to explain the high rate of reduced leaflets motion due to thrombosis formation following TAVR/ViV procedures. Even though the increased of BRT does not result in thrombogenesis by itself, it suggests that once the clotting process starts, for example by blood contact with the forgiver surface of TAVs, the likelihood of thrombosis formation increases in the low flow regions determined by increase BRT (Makkar et al., 2015; Rayz et al., 2010). Blood stasis on the aortic surface after TAVR/ViV procedures, may be considered as the main reason in thrombosis formation on the aortic surface. The theory presented in this study is examined by determine BRT in two different models representing a surgical bioprosthesis and a TAV via statistical analysis. Additionally, in this study we investigate to quantify the effect of low cardiac output on blood stasis on the TAV leaflets surface with respect to valvular thrombosis.

This project is a combination study of computational and experimental technique. A former postdoctoral Dr. Koohyar Vahidkhah performed the CFD simulation and the calculation of BRT on the TAV/SAV models. The FE simulation was performed by a former PhD candidate, Dr. Mostafa Abbasi. On the other hand, I provided with the experimental testing such as hemodynamics measurements, and PIV results for validating the CFD simulation.

3.2 Material and Method

To investigate the effect of TAVR/ViV setting configuration in intra-annular positioning on the BRT on TAV leaflets, and the likelihood of thrombosis formation on leaflet, a fluid-solid interaction (FSI) modeling was used to quantify BRT on TAV leaflets. In this modelling a computer simulation was performed to mimic the 3-D large deformation of the leaflets along with the 3-D time-dependent flow field of the bioprosthesis. The input parameters for the simulations, i.e. transvalvular pressure gradient, was obtained from the pulse duplicator. Additionally, experimental velocity measurements were used to confirm the validity of the FSI modelling. Due to the lack of optical access at the base part of TAV, where leaflets are attached to the metallic frame. Therefore, computer simulations are motivated.

3.2.1 Experimental Setup

A custom-built pulse duplicator system was used to for testing a 23 mm Carpentier-Edwards Perimount bioprosthesis to obtain the transvalvular pressure waveform and flow rate. The pressure waveform and cardiac output were control parameters for a virtual LabVIEW pulse signal generator that controls a servo pump system. A home-made silicon washer outer diameter 40 mm and inner diameter labeled sized of the bioprosthesis, and a thickness of 10 mm, was used to mount the bioprosthesis valve. The Carpentier-Edwards Perimount bioprosthesis was places on top of the silicon washer and sutures were passed through the swing ring. Additionally, a bileaflet mechanical heart valve was placed in the other side of the silicon chamber. The pulse

duplicator input parameters matched the international standard ISO 5480:2015 recommendation for testing prosthetic heart valves, that is, heart rate of 70 BPM, mean arterial and aortic pressure of 10 and 100 mmHg and cardiac output of 5 L/min. Running fluid of 37 % by volume glycerin solution (99% the science company, Denver, CO,USA) mixed with normal saline solution (Research Products International, Mount Prospect, IL, USA) was used as a blood analog solution. The blood analog solution has the following physical properties: viscosity of 3.8 cp, density of 1.105 g/cm^3, refractive index of 1.35.

3.2.2 Validation of FSI Simulation

A 2-D particle image velocimetry (PIV) system was used to obtain the flow field measurements downstream of the bioprosthesis for validating of simulations flow field. The lasers were synchronized using laser pulse synchronizer (TSI, model 610035, TSI, Inc.) and the illumination was supplied by a dual oscillator Nd:YAG laser (Litron Lasers Nano S 15 Hz). The running solution was seeded with silver coated hollow glass particles (8 μm diameter, TSI, model 10089-SLVR) to visualize the flow. The resolution of the images was 1600 × 1200- pixel cross correlation CCD camera (power View Pulse 2MP, TSI, model 630157), which can capture PIV images pairs at 30 frames per second. The spatial resolution for the 23 mm surgical bioprosthesis was 60 μm/pixel. Phase-locked PIV measurements were performed by synchronizing the PIV system from the pulse generator driving the piston pump, over 91 images were taken over the entire cardiac cycle. All images were analysis in Insight 3G TM software from TSI using Nyquist grid using 50% overlap with a final pass integration window of 28 × 28 pixel. The optical distraction caused from refractive index mismatching between the running solution and the valve mounting the chamber, was removed using calibration code. A correction function was determined and a calibration home-made code was applied to all PIV measurement images to remove optical distortion and that of the straight cylindrical pipe (Gorbet & Sefton, 2004). The

velocity field was obtained using Tecplot software (Tecplot Inc., Bellevue, WA, USA) to validate the velocity field obtained from CFD simulation.

3.2.3 CFD Simulation Steps

The obtained transvalvular pressure gradient from the pulse duplicator was used in a finite element (FE) simulation to obtain the complex 3-D large motion of the valve leaflets during the opening and closing of the valve. After that, to calculate the deformation respond of their assembly to the transvalvular pressure gradient, the large 3-D deformation was divided into several parts. In this method, the complex deformation of the leaflets was subdivided into several simpler parts, to calculate the deformation respond of their assembly to the pressure gradient. After that the deformation motion of the valve leaflets was then input in the computational fluid dynamics (CFD) model to simulate the complex 3-D flow field of the bioprosthesis. CFD simulations was performed in two different setups: (1) one representing the surgical bioprosthesis setup, this one being corresponded to the surgical valve (Fig. 3.1 A) and (2) representing TAVR setting, this one is being corresponded to TAV model (Fig. 3.1 B). After obtaining the flow field from the CFD simulation, particle tracking procedure was used to calculate BRT in the valve leaflets region using a scalar parameter known as (T_R). TR can be computed using the equation below:

$$\frac{\partial T}{\partial t} + v.\nabla T_R = 1 \tag{1}$$

3.2.4 Estimating BRT in Patient-Specific Geometry

After validating the BRT approach in models based on the geometry of the pulse duplicator as in Fig. 3.1, the theory was examined in models was driven from a patient specific geometry. The anatomical geometry was obtained from computed tomographic (CTA) images of a 76-years old female with normal aortic root geometry (Fig 3.2A). The geometry of the coronary

arteries, ascending aorta and aortic root was reconstructed using image processing. In TAVR/ViV setting, the TAV leaflets are surrounded by frame of failed bioprosthesis valve (Fig. 3.3B, top), while the TAV leaflets are confined by the native valve's leaflet as in the intra-annular positioning (Fig. 3.3B, bottom). TAV leaflets was confined by a cylindrical geometry to reduce the CFD cost and time.

A FE method was employed to simulate the 3D motion of the leaflets under different cardiac output, detailed regraded the FE approach can be found in (Barakat et al., 2018). The obtained large 3D motion of the leaflets during an entire cardiac cycle were used as an input parameter to the CFD simulation ANSYS Fluent CFD package (ANSYS, Inc., Canonsburg, PA, USA). The hemodynamic data obtained from the pulse duplicator was used as an input parameter to the CFD simulation. A 100 mmHg of mean aortic pressure, and 5.0, 3.5, and 2 L/min of cardiac outputs was used as an impute parameters to the CFD simulation. Additionally, T_R was calculated using Equ 1, to estimate BRT on the valve leaflets.

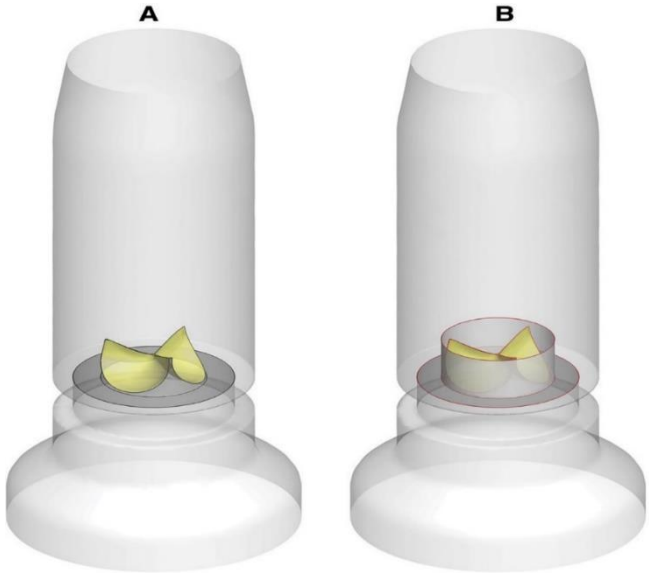

Figure 3.1: CAD models (A) surgical valve and (B) TAV model .

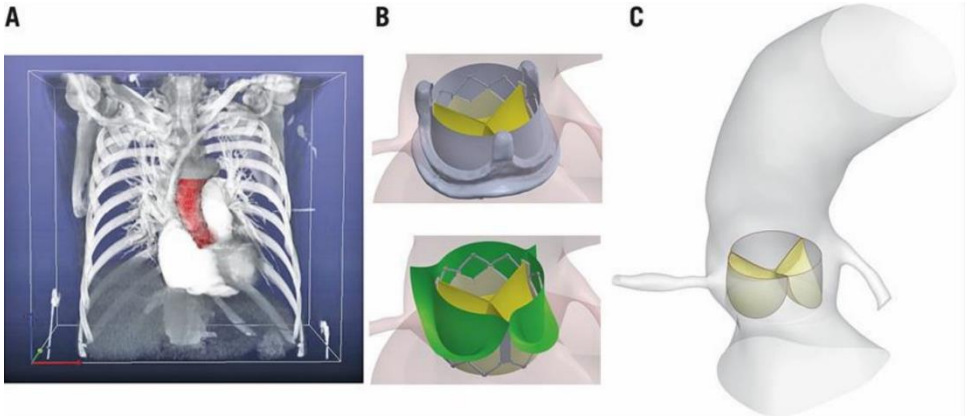

Figure 3.2: Patient-specific geometry. (A) 3D patient-specific geometry from CTA images. (B) TAV leaflets are surrounded by the a failed degenerated bioprosthesis valve as in ViV (top), TAV leaflets surrounded by the native valve as in TAV (bottom). (C) CFD TAV model.

3.3 Result

3.3.1 Hemodynamics Performance of the Valve

The valvular hemodynamics data was obtained from testing the 23 mm Carpentier-Edwards Perimount bioprosthesis in the pulse duplicator. The measured transvalvular pressure gradient (Fig 3.3) from the experimental test was used as an input dynamic loading in the FE simulations (Abbasi, Barakat, Vahidkhah, & Azadani, 2016) to obtain valve displacement. The figure below (Fig 3.4) shows the results of the FE simulations deformation of the bioprosthesis leaflets during multiple points of the cardiac cycle. An excellent agreement was observed between leaflet deformation obtained from the FE simulations and the experimental images captured by the high-speed camera throughout the cardia cycle.

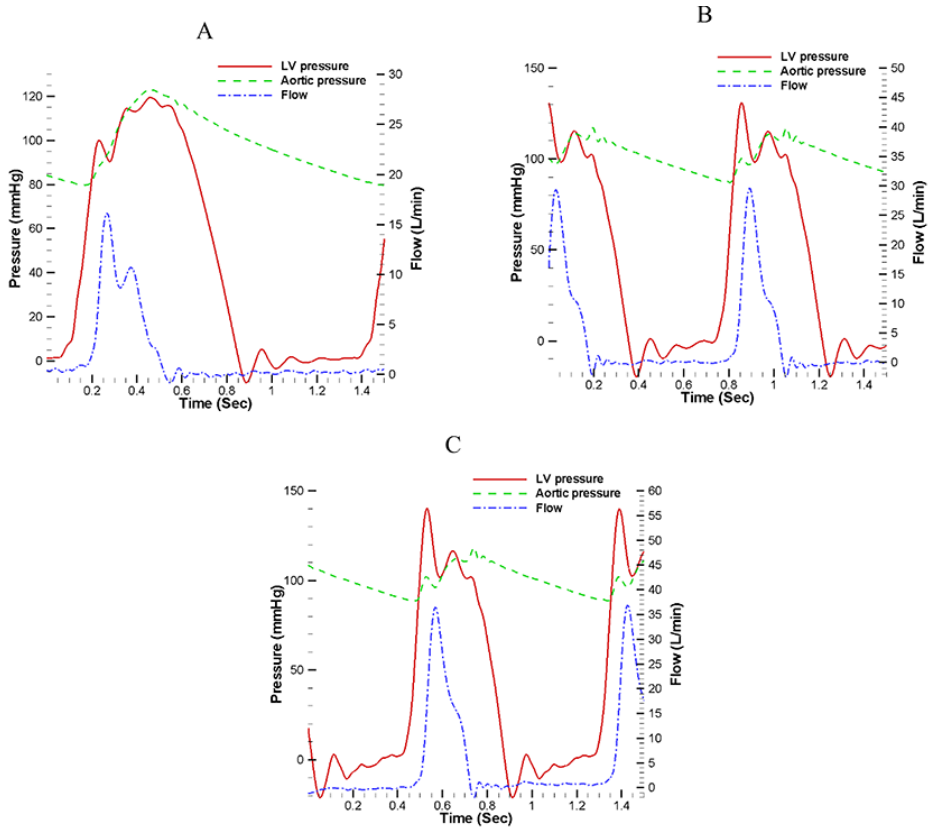

Figure 3.3: Pressure and flow curves obtained from the pulse duplicator. (A) cardiac output of 2 L/min. (B) cardiac output of 3.5 L/min. (C) cardiac output of 5 L/min.

3.3.2 Validation of FE and CFD Simulation

The results presented in the below figure corresponds to the 23-mm surgical valve, after obtaining the large 3D deformation of the bioprosthesis leaflets from the FE simulation, it was used as an input parameter in the CFD model to simulate the flow through the bioprosthesis valve. A comparison was made between the CFD flow field simulation and the PIV measurement at the peak of flow, to ensure the validity of the flow in term of flow structure (Fig 3.4(B)). The presented velocity magnitude contours in Fig 3.4(B) as well as the stream traces during the valve opening, which were obtained from CFD simulation and PIV experimental measurement, are illustrated in (Fig. 3.4B(left)) and (Fig. 3.4A(right)). To the reader knowledge, the plane at which

the velocity contours are presented in (Fig 3.4(B)) was at the mid plane longitudinally cutting through the bioprosthesis valve. Overall, the above result confirms the validity of the flow structure in the study.

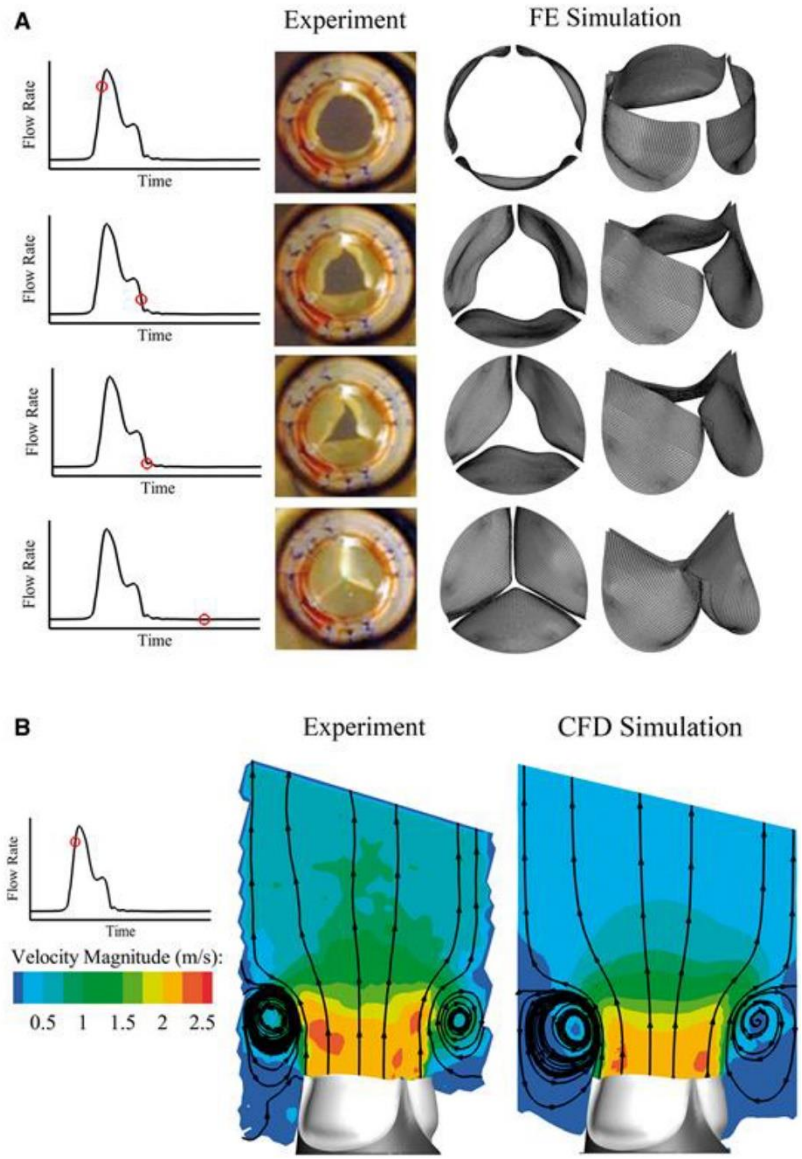

Figure 3.4: Validation of FE and CFD simulation. (A) Comparison between leaflet motion captured by the high-speed camera and FE simulation. (B) Comparison between flow field captured via PIV and CFD simulation at the peak of systole.

3.3.3 Quantifying BRT in Surgical and Transcatheter Valve During Forward Flow

After confirming the validity of flow field of the two-models which is representing surgical and TAV valve based on the geometric of the pulse duplicator. Random particles were generated in the simulated flow field to visualize the effect of the geometric confinement of the TAV on the BRT on the valve leaflets. The procedure was performed as follows: first, 3000 particles was randomly distributed in the region of interest (ROI). To the reader knowledge the ROI was defined as the volume between the inner surface of the confining cylinder, which modeled as the calcified valve or the degenerated bioprosthesis valve, and the outer surface of the leaflets. In this study the defined ROI illustrates the region in close to the aortic side of the leaflets. To quantify BRT throughout the opening and closing of the valve, the cardiac cycle was divided into four stages: I- forward flow, II, closing, III-end of closing to mid diastole, IV-mid diastole to early systole. Consequently, in the beginning of each phase, the distributed particles were generated and tracked during the time period. The generated particles follow the flow velocities and their variation in time throughout the cardiac cycle.

The below figure of the velocity contours of the two models demonstrated the particle tracking during the forward flow (Stage I). The top raw illustrates the flow field of the surgical valve in (Fig. 3.5(A)), and that of TAV is illustrated in (Fig.3.5(B)). The contours of the flow field is shown by the 3D-stream traces and the velocity magnitude contours in the mid-plane of the CFD domain. The distributed particles are shown in black dot, each black dot showing one particle. As its clearly to see in (Fig. 3.5), the formation of jet and recirculation areas were similar between the two models. Additionally, it was easy to notice that the generation of particles was similar between the two models in the opening stage as it shown in the first three columns. However, there is a significant difference in the distribution of particles between the two models in the late stage of forward flow, the last two columns in (Fig 3.5). While its clearly to see that the

particles were almost washed out of the ROI in the surgical valve model, a significant number of particles are resided in the ROI on the leaflets of TAV. This result demonstrates the effect of the confident geometry around TAV on BRT.

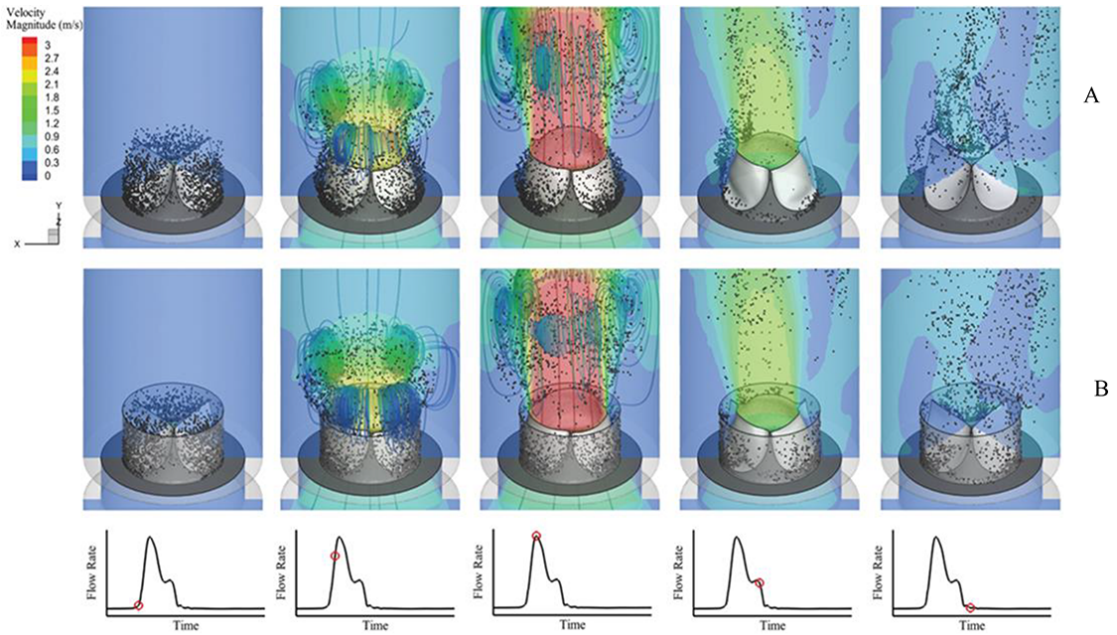

Figure 3.5: CFD simulation result showing the distribution of particles during the forward stage. (A) represent surgical valve. (B) represent TAV model. and the bottom raw indicate the time of the flow field contours with respect to flow curve.

3.3.4 Quantifying BRT in Surgical and Transcatheter Valve During Valve Closing

The below snapshots of the particle motion during the end of closing to mid diastole (Stage-III), while the valve is completely closed. The surgical valve is shown in (Fig3.6A), while the velocity contour of TAV is shown in (Fig. 3.6B). Like Stage-I, a significant difference in the distribution of particles between the two models, especially at the end of diastole. Again, a considerable number of particles were noticed to reside on the leaflet in TAV model in the ROI, while most of the particles were washed away in the surgical valve. Fig 3.6 demonstrates that more particles are being trapped in TAV model in early and mid-diastole, compare to SAV model.

3.3.5 Quantify Blood Resident Time in Low Cardiac Cycle.

The same procedure was followed to estimate BRT on the leaflets during low cardiac output, 3000 imaginary massless particles were randomly generated in the volume of the ROI between the outer surface of the leaflets and the inner surface of TAV. The distributed particles have the same velocity magnitude as the simulation. In this part a lagrangian approach was used to follow and track each particle over time during each stage. The effect of low cardiac output on BRT on TAV leaflets is shown in (Fig. 3.7), the figure demonstrates contours of time resident of BRT on the three leaflets during an entire cardiac cycle. During the forward flow, there is no significant different in BRT among the three cases during the valve opening and closing (the first three columns) in Fig. 3.7. While, it is observed that BRT was higher mostly at lower cardiac output during diastole (the last three columns) as in Fig. 3.7. The BRT is high mostly in the fixed boundary of the three leaflets at lower cardiac output cases especially with cardiac output 3.5 ml/min and 2 ml/min. Blood stasis are not only found in the fixed boundaries of the leaflets, blood stasis was high in the lesser extent of the free edges. This might be because of the slight distortion in the leaflet coaptation during diastole in the TAV model.

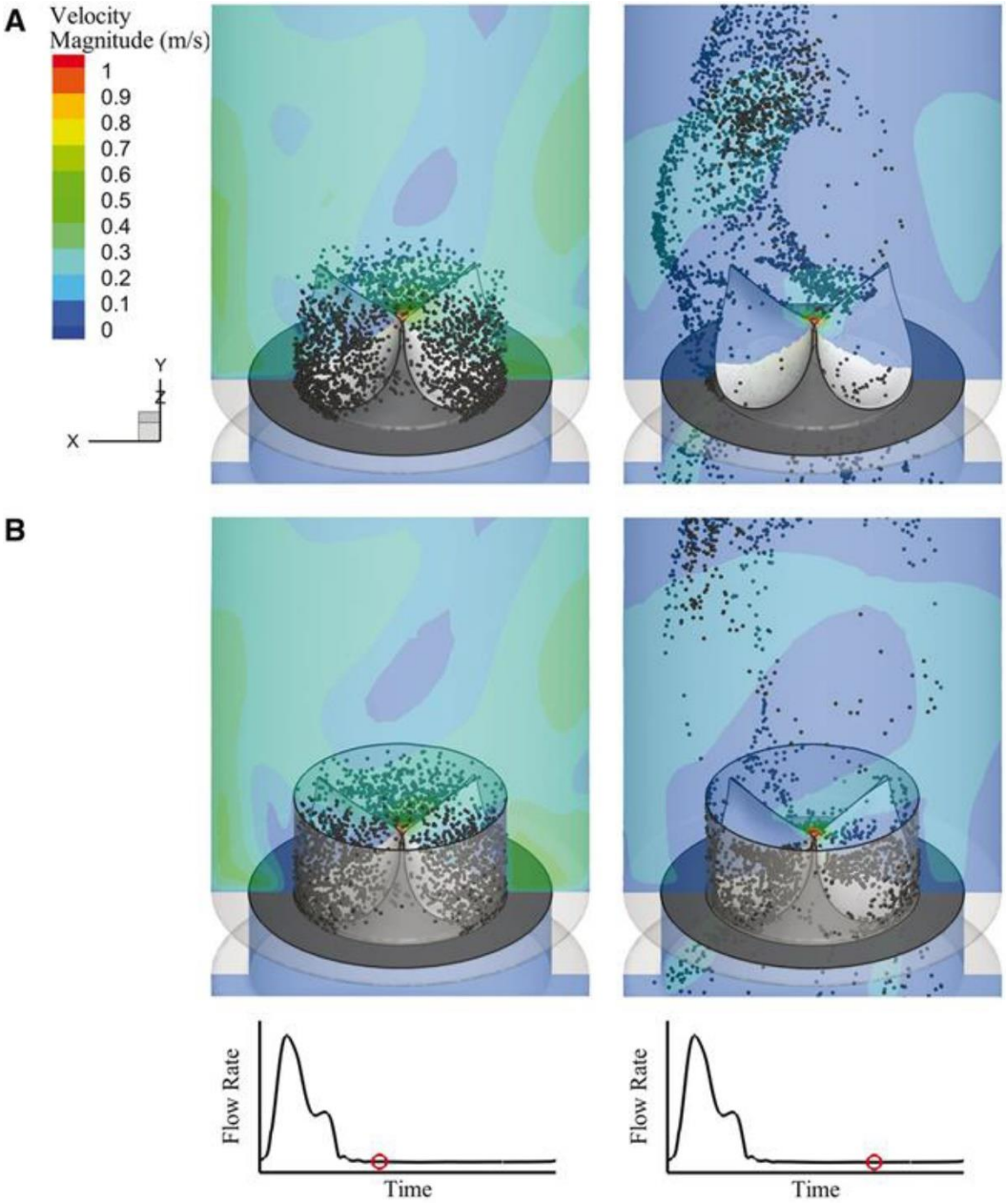

Figure 3.6: CFD results demonstrating the particles released in the ROI during stage-III in a cardiac cycle. (A) Snapshot illustrates particles released downstream of surgical valve. (B) Snapshot illustrates particles released downstream of TAV.

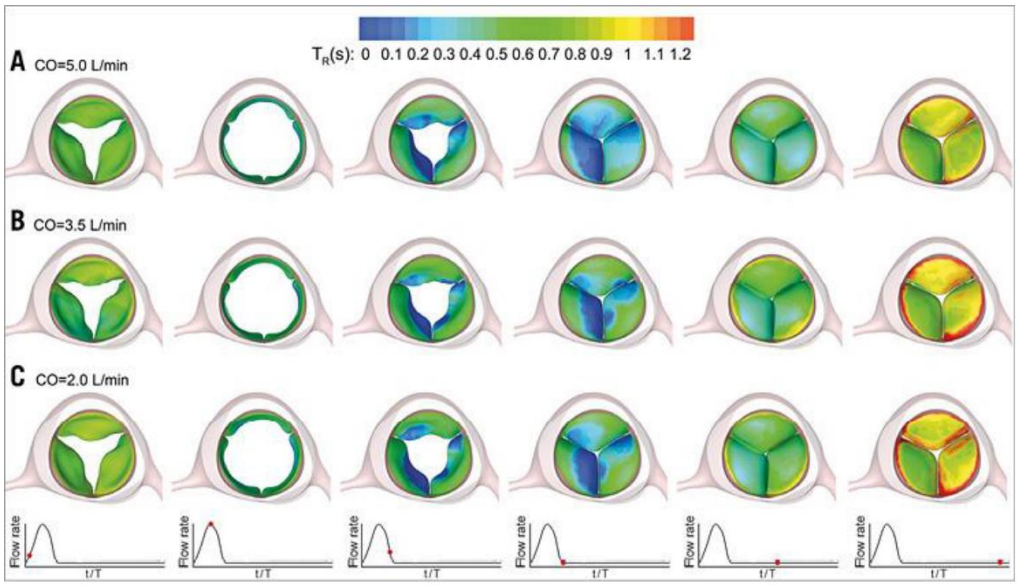

Figure 3.7: illustrates the contours of BRT on TAV model leaflets during a whole cardiac cycle. (A) BRT at cardiac output 5 L/min. (B) cardiac output at 3.5 L/min/ (C) cardiac output at 2 L/min.

3.3.6 Quantifying BRT in two models

Statistical analysis was performed to quantify the differences between the two models in term of BRT on valve leaflets. The resident time (T_R) of the distributed particles in the volume of ROI, was computed based on the velocity and displacement of the particle in the ROI. The statistical analysis was calculated after all the particles in all the four stages of an entire cardiac cycle in the two models computed. The statistical analysis demonstrated that TAV model has high T_R, compared to the surgical model in the four stages (Fig. 3.8). Comparison analysis between the two models are shown in (Fig. 3.8) included standard deviation which shown as error bar. As it is observed, the value of T_R was 39% higher in TAV model compared to surgical valve during the forward flow (Stage I). Moreover, T_R was even higher during closing (stage II) 132% than surgical valve and was even higher during closing to mid-diastole (Stage III) and mid-

diastole to systole (Stage IV). It should be mentioned that a significant difference was noticed between all cardiac stages in term of T_R for both models ($P < 0.0005$).

In the same way, BRT percentage analysis was performed to quantify the observed difference in BRT among low cardiac output cases at the end of diastole. In this case the presented data was defined as S which is the percentage of the total area of the TAV model leaflets on which blood stasis was noticed to be higher than a selected value. The threshold values of BRT were chosen as 0.8 to 1.2 s with increment 0.1 s. The selected threshold values were based on the surface-avenged BRT to the local surface maximum BRT on TAV model leaflets during the end of diastole in the simulation. The results of the total percentage in term of S among the three cases of lower cardiac cycles are presented in (Fig. 3.9). As it can be observed, a significant increase of BRT on TAV model leaflets with low cardiac output cases. The criteria of TR > 1.2 , the value of S was computed to be 2, 8, and 11% at cardiac output of 5, 3.5, and 2 L/min, respectively. This result illustrates that there is a strong correlation between low cardiac output and increased blood stasis on TAV leaflets, which could lead to increase the likelihood of thrombosis formation on leaflets.

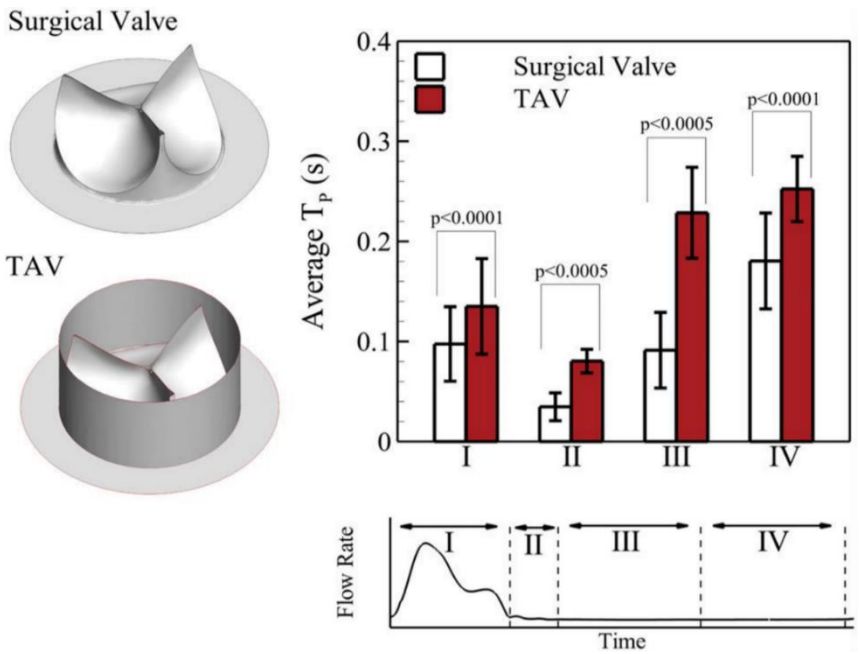

Figure 3.8: Statistical compression average BRT between TAV and surgical models in different stages of the cardiac cycle. I-forward flow, II-closing, III-end of closing to mid-diastole, IV-mid diastole to early systole.

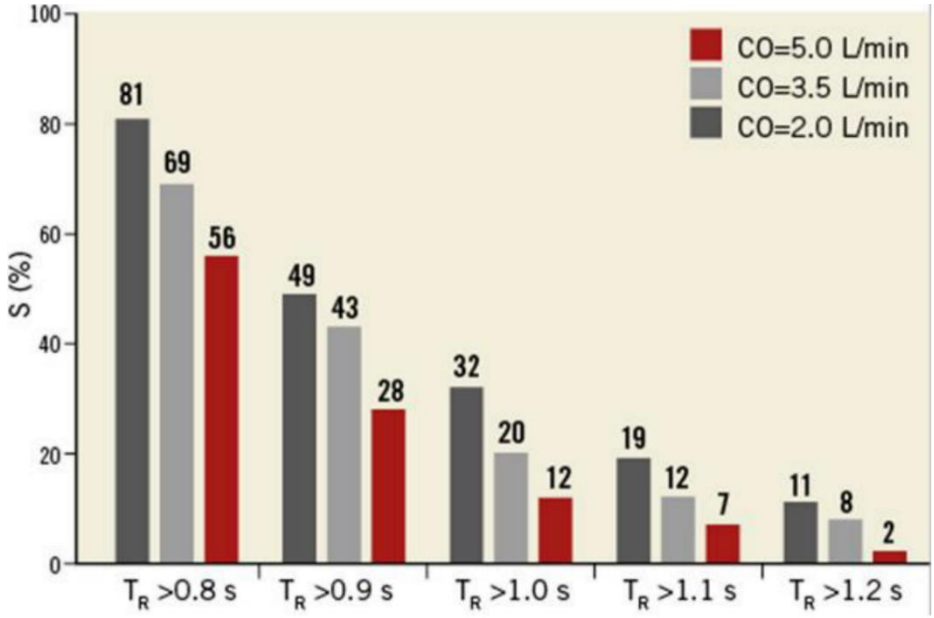

Figure 3.9: Evaluation n of the largest BRT areas on TAV leaflets at three different cardiac output. The vertical axis representing the area of three leaflets on which BRT is higher than critical values on the horizontal axis.

3.4. Discussion

3.4.1 Summary

In this chapter, we demonstrated the possibility of thrombosis formation on TAV leaflets due to the present of confining geometry in TAV, by investigation of BRT on the TAV leaflets. The CFD results illustrated a significant longer BRT on TAV leaflets, in contrast to surgical valve during the entire cardiac cycle. the average value of BRT was found to be 39% higher in TAV model compared to the surgical valve model, during the forward flow. In the same way, the average of BRT was higher in TAV model compared to surgical model value was 150% and 40$, respectively, during diastole. The CFD results of this study confirm the validity of the proposed theory that the geometric confinement of TAV due to native calcified valve or failed bioprostheses lead to increase of BRT which increase the possibility of thrombosis formation on TAV leaflets.

3.4.2 Thrombosis Formation post TAVR and SAVR

Generally, the appearance of thrombosis formation post SAVR has been lower than TAVR procedure, which could be because of neglecting of its awareness. One of the most reliable tools to investigate the present of thrombosis formation on leaflets and leaflets immobility are 4-D computed tomographic or transesophageal echocardiographic assessments. Subclinical thrombosis formation and reduced leaflets motion has been observed post TAVR and SAVR. A recent published clinical study found that reduced leaflets motion was noticed in 13% of the patients with either TAVR or SAVR, however in 40% among TAVR patients (Abbasi et al., 2016). Normally, patients whom underwent with bioprosthetic heart valves are at more risk of peripheral embolism and stroke than the normal patients. Therefore, the American Heart Association recommended patients with aortic bioprosthetic valves to take vitamin K antagonists

(VKAs) for 3-6 months, on the other hand, aspirin is recommended over VKA in European Society of Cardiology guideline (Makkar et al., 2015; Nishimura et al., 2014).

Flow stagnation and low flow regions in the sinus area has been previously studied due to blood stasis. For example, a study showed a significant reduced of blood flow in the bases of the sinus by performing PIV flow measurements (Members et al., 2012). A second published study reported the effect of TAV positioning on the flow residence time and wall shear stress in the aortic root (Ducci, Tzamtzis, Mullen, & Burriesci, 2013). Another study addressed the thrombotic potential by examining the sinus wall shear stress , in different axial positioning in ViV setting (Groves, Falahatpisheh, Su, & Kheradvar, 2014). However, most of these studies were mainly focused on the fluid dynamic characteristics in the aortic root. Nevertheless, the association between the flow stagnation regions in the sinus of aortic root and reduced leaflets motion due to thrombosis formation still unclear. In this study, the calculation of the BRT was performed in the defined of ROI, the selected ROI is supported by clinical studies where thrombosis has been mostly observed (De Marchena et al., 2015; Midha et al., 2015).

3.4.3 Thrombosis Formation in Low Cardiac Output

In this chapter, we demonstrated the effect of low cardiac output on blood stasis post TAVR procedure, and the likelihood of thrombosis formation due to the present of the confinement geometry of TAV device. Other hemodynamics parameters could indicate the present of valvular thrombosis such as aortic regurgitation and transvalvular pressure gradient (Makkar et al., 2015). However, geometric parameters may affect thrombosis formation on TAV compared to hemodynamic effects. For example, a study demonstrated the possible link between TAV size and the increase risk of valvular thrombosis (Chakravarty, Abramowitz, Jilaihawi, & Makkar, 2016). That encourages a computer simulation to study and address the effect of TAV geometric on blood stasis on TAV leaflets.

Some available clinical data suggest a strong relationship between reduced left ventricle ejection fraction (LFEF) and thrombosis formation after TAVR or ViV procedures. For instance, a clinical study illustrated the possible association between low LVEF (<35%) and thrombosis formation post TAVR (Hansson et al., 2016). In the same way, a recent clinical observation has pointed out to a significant correlation between low ejection fraction and the predication of leaflet thrombosis (Leetmaa et al., 2015). However, another clinical data reported that an LVEF of <35% is not sufficient to predicate leaflet thrombosis . The CFD results of this study show a significant correlation between low cardiac output and leaflet thrombosis. The presented data might help to demonstrate the apparent of leaflet thrombosis in the clinical data. In this study we proved that cardiac output is an appropriate factor to address the likelihood of leaflet thrombosis compared to LVEF.

3.4.4 Study Limitation

This chapter is a combination of computational studies and experimental testing environment which can be used to validate the computer simulation results. One of the limitations of this study is the absent of the aortic root geometry in the model, however in the current study the determine of the ROI was realistic condition, therefore our hypothesis is not affected by the geometric simplification. Geometric details such as TAV stent, calcified native valve and bioprosthetic frame or failed bioprosthetic valve around the stent were missing in this work which consider a second limitation, however the presented hypothesis mostly focus on quantify and comparison of the BRT between the surgical and TAV models, therefore the results remain valid, though the absent of the geometric details. Even with all the listed limitation, the defective washout of blood from bioprosthetic leaflet is unbelievable to change or vary by defining more details to the models.

3.5 Conclusion

In short, the results of this study demonstrate that flow field in TAVR leaflets disrupted because of the geometric confinement resulted from calcified native valve or degenerated bioprosthesis that circumferentially around the TAV, as opposed to SAVR. Additionally, there is a significant association between low cardiac output and increased BRT which can increase the likelihood of thrombosis formation on TAV leaflets. Areas of low blood flow could lead to valvular thrombosis by accumulating platelets and blood proteins to a critical concentration. Furthermore, the presented geometric confinement in TAV causes to longer BRT which lead to leaflets thrombosis. The above results support many clinical observations on reduced leaflet motion due to valvular thrombosis following TAVR and ViV procedures. The presented results suggest further investigations regarding geometric variability associated with TAVR and ViV procedures in term of TAV type, size and positioning.

Chapter 4: Assessment of Paravalvular Leakage Post Transcatheter Aortic Valve Replacement: A New Approach Based on Maximum Momentum Flux

4.1 Introduction

Previously, TAVR was a limited treatment option for patients whom are at high risk of open-heart surgery. Recently the U.S. Food and Drug Administration (FDA) approved TAVR regardless of patient's surgical risk (Chakravarty et al., 2017; Coylewright et al., 2020). In contrary to SAVR, where surgeons remove the calcified valve and replace it with a bioprosthetic valve, in TAVR procedure transcatheter aortic valves (TAVs) are implanted within native or a degenerated bioprosthetic valve. As a result of TAVR procedure, paravalvular leakage (PVL) is a frequent complication among TAVR patients (Coylewright et al., 2020; Neragi-Miandoab & Michler, 2013; Webb et al., 2007). There is growing evidence suggesting a significant association of PVL, even mild, with short and long-term mortality (Grube et al., 2007). The incidence of mild PVL post TAVR is still quite significant with the third generation of TAVR devices (Kodali et al., 2012). A clinical study has reported the severity of PVL post TAVR was 32% mild, 40% moderate and 17% severe (Chakos et al., 2017). Nevertheless, there is a lack of validated protocol to evaluate PVL post TAVR and ensure the appropriate classification of its severity.

Accurate evaluation of PVL is essential for clinical decisions. The current TAVs device provides superior systolic performance in terms of hemodynamics performance (Barakat et al., 2018; Gotzmann et al., 2011; Walther & Falk, 2009). However, measuring the regurgitation

volume (RV) of PVL is considered to be the most accurate way to evaluate the severity of PVL, the current guideline concludes that an RV of <30 ml/beat, 30-59 ml/beat and <60 ml/beat corresponds to mild, moderate and severe, respectively (Clavel et al., 2009; Zoghbi et al., 2009). Nevertheless, measuring RV in patients can be performed using MRI, however it's not accurate and costly. On the other hand, the circumferential extent (CE) of PVL has been introduced by the Valve Academic Research Consortium II (VARC II) as a semi-quantitative method to classify the severity of PVL post TAVR (Kappetein et al., 2012; Lang et al., 2005). This method depends on capturing careful imaging of the paravalvular jet in a short axis view, at the level of the TAVs using two-dimensional echocardiograph (Bloomfield et al., 2012). Although the CE has not been validated, it has been widely used to estimate the severity of PVL. According to this method a CE of 10-29% suggests to moderate PVL, less than 10 % corresponds to mild PVL and larger than 29% of PVL suggests to severe PVL (Kappetein et al., 2012). Additionally, totally depending on short axis echocardiography images, often can be limited and misleading due to the present of multiple PVL jets that are not parallel to the echo probe (Pibarot, Hahn, Weissman, & Monaghan, 2015). In this study, we first validate the CE of PVL, and then propose a new novel approach based on fluid dynamics concept to assess the severity of PVL. The proposed method is based on the estimation of the maximum momentum flux at the vena contracta of the leakage jet flow using parameters that are currently being used for PVL classification, i.e. maximum jet velocity, CE of PVL, and the aortic and ventricular pressures. The validation of CE and estimation of maximum momentum flux was achieved via computational flow dynamics (CFD) modeling and in vitro

This study is a combination work of CFD modeling and experimental approach. To ensure the feasibility of the proposed approach, first a CFD model was developed to estimate the CE in correspond to multiple level of PVL severity at steady flow condition. After that, the maximum momentum flux was estimate. After ensuring the feasibility of our new approach, an in vitro study was performed to measure and estimate the CE and maximum momentum flux, respectively under a pulsatile flow condition. The CFD simulation was performed by a former postdoctoral Dr. Koohyar Vahidkhah. I conducted the experimental testing which was used to validate the CFD modeling.

4.2 Material and Method

4.2.1 Theoretical Background

In this study we present a simple approach based on fluid dynamics concept to estimate maximum momentum flux in PVL using parameters that are recommended by VARC-II to assess the severity of PVL post-TVAR. The parameters we introduce to estimate the maximum momentum flux, are being currently used to estimate the severity of PVL, such as maximum velocity jet, CE of the jet, and the aortic and ventricular pressures of the PVL. The schematic layout in Fig. 4.1 demonstrates the location and the procedure of presented approach. In (Fig. 4.1a) is a CFD snapshot showing the locations of where these parameters were measured, while in (Fig. 4.1b) a flowchart demonstrates the overall procedure to estimate the maximum momentum flux at the vena contracta. The following calculation steps were performed in in vitro and in CFD simulation results:

Bernoullie equation was used to estimate the pressure at the vena contracta (P_{vc}). The equation was applied between aortic and vena contracta as in (Fig. 4.1a), assuming the difference height as well as the head loss are negligible.

$$\frac{P_A}{\rho g} = \frac{P_{vc}}{\rho g} + \frac{V_{vc}^2}{2g} \tag{1}$$

By using Eq. 1, the pressure at the vena contracta can be estimated as $P_{vc} = P_A - \frac{\rho V_{vc}^2}{2}$. Where ($V_{vc}$) is the maximum velocity of the PVL which is measured using Doppler CW long axis view, while P_A is measured in the pulse duplicator. Once P_{vc} is found, the following momentum equation balance was applied between vena contracta and left ventricle:

$$P_{vc}A_{vc} + \rho V_{vc}^2 A_{vc} = P_{LVOT}A_{LVOT} + \rho V_{LVOT}^2 A_{LVOT} \tag{2}$$

In Eq. 2 the viscous loss due to duct walls were neglected since we are measuring maximum momentum flux which is at the vena contracta. (P_{LVOT}) represents the LVOT pressure which is measured in the pulse duplicator. On the other hand, (A_{LVOT}) is estimated using images taken by color doppler from short axis view. Additionally, (V_{LVOT}) is measured using Doppler PW from long axis view at the location where A_{LVOT} were estimated. Having the values of pressure and velocity at the vena contracta with the surface area at the exit of the jet, the area of vena contracta can be estimated by using Eq. 2 $A_{vc} = A_{LVOT}(P_{LVOT} + \rho V_{LVOT}^2)/(P_{vc} + \rho V_{vc}^2)$ The estimated values of A_vc can then be used to estimate the maximum momentum flux of the PVL $J_{max} = \rho V_{vc}^2 A_{vc}$.

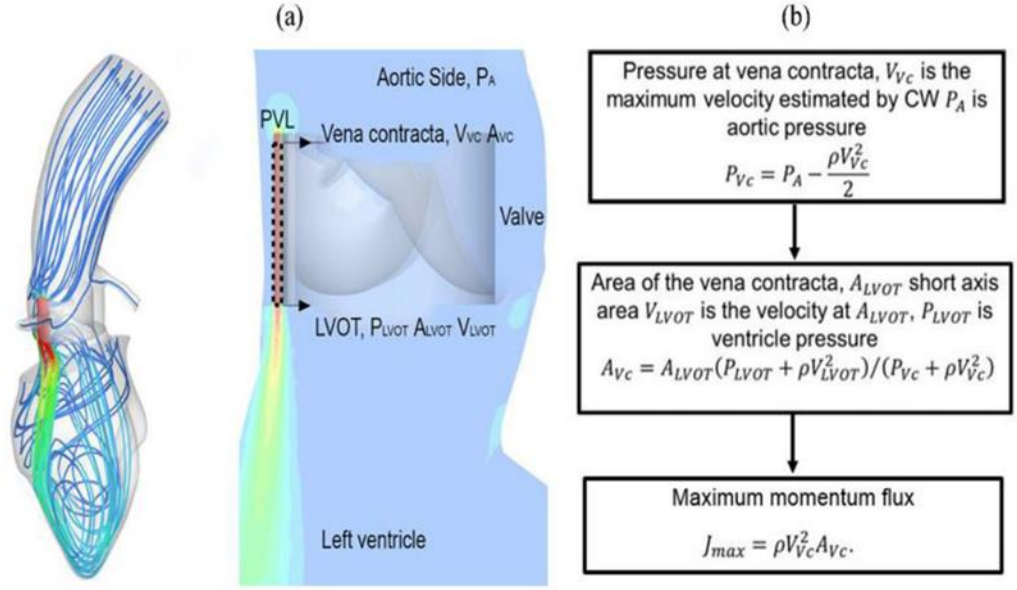

Figure 4.1 (a) Schematic of the idealized flow simulation model for PVL. (b) Overview of the proposed approach for the assessment of the severity of PVL regurgitation.

The proposed method is summarized as follows:

1- Estimate the pressure at the Vena Contracta: $P_{vc} = P_A - \frac{\rho V_{vc}^2}{2}$. Note that the values of P_A comes from the pulse duplicator, and V_{vc} comes from long-axis CW measurement.
2- Estimate the surface area of high velocity regions at TAV color Doppler short-axis plane A_{LVOT} in the LVOT region.
3- Estimate the velocity at A_{LVOT} from long-axis view PW measurement V_{LVOT}.
4- Estimate the area of vena contracta from $A_{vc} = A_{LVOT}(P_{LVOT} + \rho V_{LVOT}^2)/(P_{vc} + \rho V_{vc}^2)$.
5- Estimate the maximum momentum flux of PVL using $J_{max} = \rho V_{vc}^2 A_{vc}$.

4.2.2 CFD Simulation of PVL

The geometry of the flow simulation was obtained from a de-identified computed tomographic angiography (CTA) images of a 76-year-old female see (Fig. 4.2a). The geometry of the left ventricle, aortic root, ascending aorta, and the coronary arteries was then reconstructed using an image processing package (ScanIP; Simpleware Ltd., Exeter, UK). Once the patient

specific geometry was obtained, a model representing PVL was developed. The PVL was modeled by introducing gaps between the TAV geometry and the native valve commissures as its seen in (Fig. 4.2b). The level of the leakage was adjusted by the curves that represented the free edges of the native valve leaflets at the commissures.

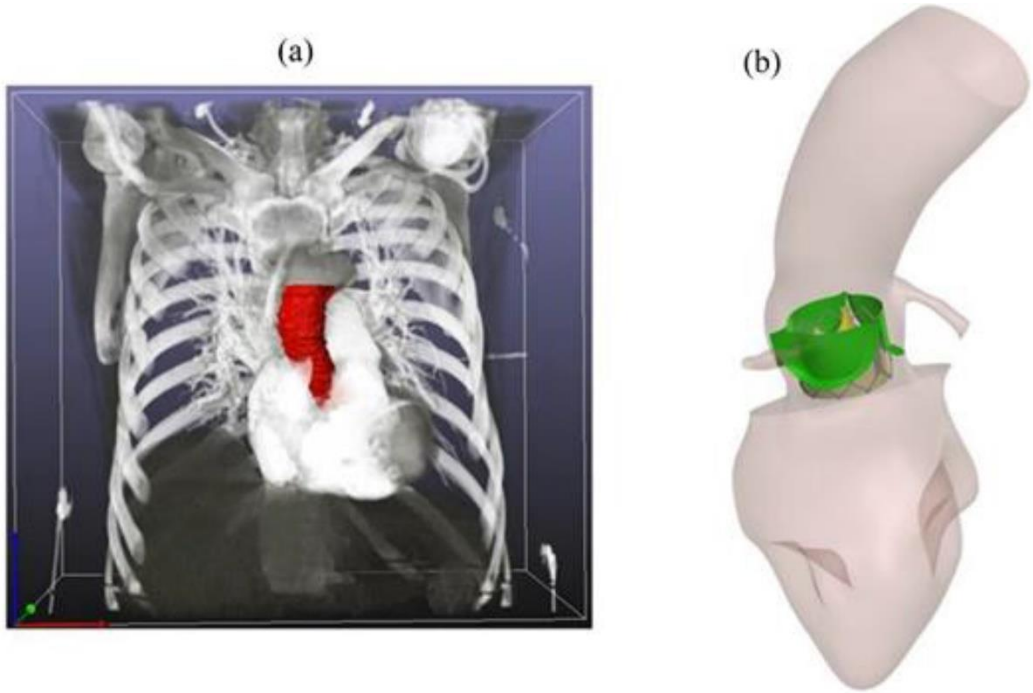

Figure 4.2 (a) Construction of the 3D patient-specific geometry via processing of CTA images. (b) Computational 3D model for the TAV.

The geometry generated for each PVL case was discretized by unstructured tetrahedron cells using ANSYS Meshing. The mesh was refined near of the aortic valve, where large pressure gradients were expected. The PVL flow was generated by prescribing an average aortic pressure of 76.5 mmHg and an average ventricular pressure of 5.0 mmHg to the boundary surfaces of the computational domain. The above choice of pressure values was based on time-averaging the transient aortic and ventricular pressures during diastole. Similarly, at the coronary artery outlets, the average pressure was prescribed based on normal phasic coronary blood flow. The use of time-averaged pressure boundary conditions allowed steady-state simulations and consequently

reduced computational cost and time. In addition, a standard k-ε turbulent model with standard wall functions were employed for the flow simulations. No-slip boundary conditions were applied to the surrounding wall, valve frame and leaflets, as well as the TAV confining geometry. A second-order implicit transient formulation was utilized to solve the conservation equations. The density and the viscosity of blood were 1060.0 kg/m3 and 0.0035 kg.s/m2, respectively.

4.2.3 Fabrication of PVL and Valve Models

Clinically, most of PVL cases accrue near or at the TAV's commissure as it shown in Fig. 4.3 (a-b) (Zamorano et al., 2011). Therefore, to model PVL in vitro, a custom-built 3D printed washer was used by introducing three anatomically realistic gaps between the TAV geometry and the native valve commissures as it shown in Fig. 4.3 (c). Additionally, a 26 mm SAPIEN 3 Transcatheter Heart Valve (Edwards Lifesciences) was implemented within the 3D printed washer as in Fig. 4.3 (c), was placed at the aortic position. The SAPIEN 3 was not fully expanded to its labeled diameter, for a potential higher-pressure gradient than normal. Also, a bileaflet mechanical heart valve was placed at the mitral position. The flow through the gaps are driven by contraction from the aortic side followed by duct entrance and exiting into the left ventricle chamber. The jet flow inside the duct is driven from the pressure gradient between the aorta and the left ventricle. The jet reaches its maximum velocity at the vena contracta which occurs at the entrance of the duct. After the jet exits the duct, the flow is confined by the left ventricle outflow tract (LVOT) geometry and the left ventricle chamber. The stages of PVL severity was controlled by increasing and decreasing the circumference of the gaps, however, the gap width was kept at 2 mm. The 3D printed washer has an outer diameter of 40 mm, and an inner diameter of the TAV 22 mm, and height of 16 mm.

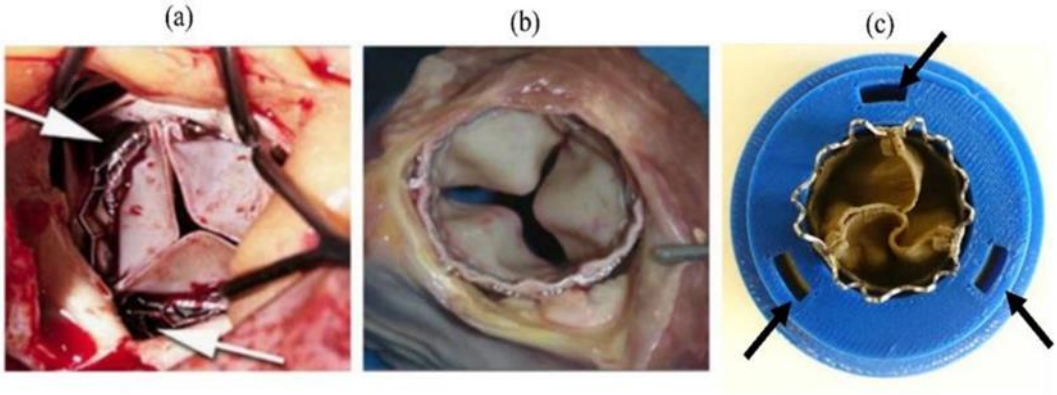

Figure 4.3. (a) TAVR implanted on calcified valve, the white arrows show the TAV's commissure. (b) Show the bottom view of TAV. (c) SAPIEN 3 TAV implanted in the 3D-printed washer, the black arrows show the gaps facing the valve's commissure.

4.2.4 Experimental setup

An in vitro study provides a consistent and well-controlled environment to assess and quantify the severity of PVL. A custom-built pulse duplicator (BDC Labs, Wheat Ridge, CO, USA) was used for testing, as previously illustrated (Litzler et al., 2008). The image of the experimental setup and diagram layout are presented in (Fig. 4.4a-b). The pulse duplicator consists of silicon ventricle chamber pressurized in a water tank. The system generates physiological flow condition by pulsatile pump. Additionally, the pulse duplicator input parameters matched the international standard ISO 5840:2015 recommendations for testing prosthetic heart valves; that is, heart rate of 70 beats/min, and cardiac output of 5 L/min. The mean aortic pressure was set to 100 mmHg first and then to 120 mmHg to generate wide range of data measurements of PVL severity for patients with normal and high mild hypotension. Recirculating fluid of 36% by volume glycerin solution (99% The Science Company, Denver, CO, USA) in phosphate buffered normal saline solution (Research Products International, Mount Prospect, IL, USA) was used as a blood analog fluid. The blood analog solution contained Silver coated hollow glass particles (8 µm diameter, TSI, model 10089-SLVR). Additionally, the running solution has a viscosity of 3.6 cP, a density of 1.102 g/cm3 at room temperature. Pressure

was measured in the aorta and left ventricle chamber using strain gauge pressure transducers (Utah Medical Products, Midvale, UT, USA). Static pressure measurement was taken at 105 mm downstream and 35 upstream of the aortic and left ventricle, respectively. Moreover, pressure transducers were calibrated prior to the tests using Delta-Cal Pressure transducer simulator/tester (Utah Medical Products, Inc). In addition, an electromagnetic flowmeter (Model 501, Carolina Medical Electronics Inc, East Bend, NC, USA) was located on top of the aortic valve and used to measure the regurgitation mass flow rate of the RV in the system as it shown in (Fig. 4.4b).

4.2.5 Doppler Measurements

Doppler echocardiography measurements were perform using iE33 ultrasound system (Philips Medical Systems, Andover, Massachusetts) and a V219 (2.5 MHz) was steadily placed at the bottom and the side of the pulse duplicator tank as it shown in (Fig. 4.4b). The Doppler measurements were performed based on the current recommendation and guidelines (Barakat et al., 2018; Lang et al., 2005)] for evaluating the severity of PVL. Velocity measurement was performed by placing the probe beam at the bottom of the pulse duplicator tank see (Fig. 4.4b). The velocity at the vena contracta was measured along the jets using continuous wave Doppler (CW) from long axis as it seen in (Fig. 4.4b). Furthermore, pulse wave (PW) were used to measure velocity at the exit of the jets in the LVOT region. Area of the jets were taken using color Doppler from short axis view by placing the probe beam on the side of the water tank (Fig. 4.4b). Color Doppler was performed right below at the bottom of the TAV's level, and at the

location where PW velocity was measured using short axis as it's shown in Fig 3(b). Moreover, three cardiac cycles were captured for all echocardiography results.

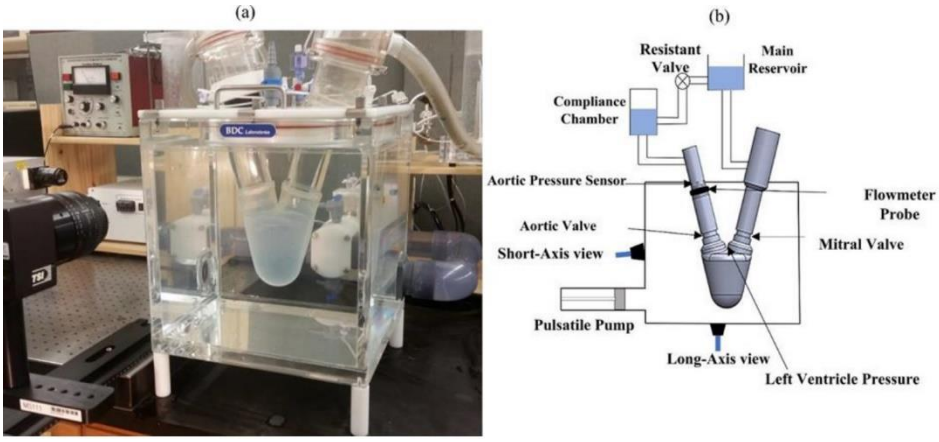

Figure 4.4. (a) Pulse duplicator system with valves positioned within the system. (b) Diagram layout of the experiment setup.

4.3 Results

4.3.1 CFD Steady Validation of Circumferential Extent

The CFD results in (Fig. 4.5a-c) demonstrates a sample of the short axis view from the CFD simulation with RV of 47.7 ml/beat. The velocity contours in (Fig. 4.5a-b) are shown at the bottom plane of the SAPIEN 3 at which the echocardiography views are obtained to evaluate the severity of PVL. As it shown in (Fig. 4.5b), for evaluation the PVL, the contours of velocity magnitude must be ideally viewed at the TAV plane short axis view; i.e. the plane that encompasses the lowest circular curve of the TAV stent and the Dacron at the ventricular side. On the other hand, in (Fig. 5c), a stream traces are colored by the fluid velocity magnitude to visualize the flow view on a plane that longitudinally along the PVL jet at the leakage origin. The PVL severity in each simulation was determined directly by calculating the RV from the flow velocities at the computational outflow. After obtaining the accurate PVL severity from the calculated RV in each case, the accuracy of the PVL assessment by the CE of PVL can be validated.

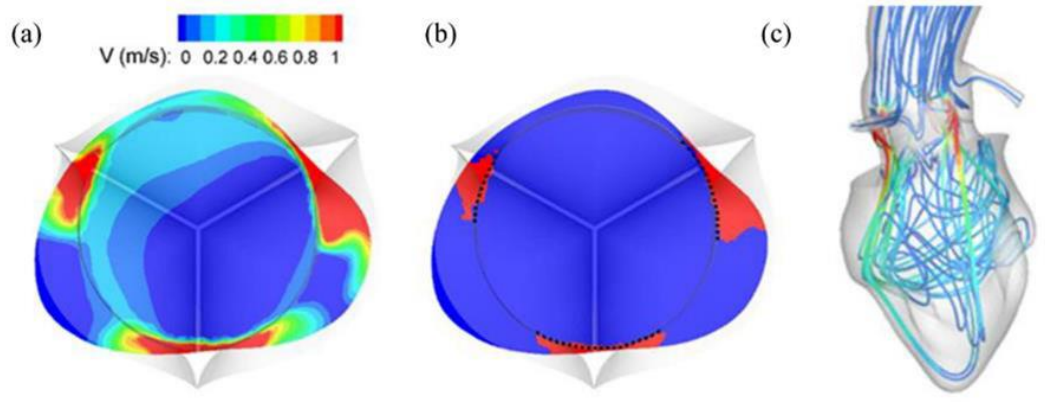

Figure 4.5. CFD results simulation of paravalvular leakage. (a,b) The corresponding contours of flow velocity magnitude of PVL from short axis view. (c) Long axis view velocity flow contours of PVL jet.

The CE of PVL is visually estimated as the percentage of the perimeter of the TAV occupied by high flow velocity regions in the short-axis view. (Fig. 4.5b) demonstrates how CE of PVR was estimated in the simulations, the total length of the dashed lines is calculated and divided by the TAV perimeter. According to the guidelines (Baumgartner et al., 2009; Zamorano et al., 2011) a CE of PVL of 10-29%

Corresponds to medium PVL, and values smaller than 10% and larger than 30% correspond to mild and severe PVL, respectively. The semi-quantitative parameters for the assessment of AR severity, i.e. CE of PVL, were calculated for each simulation. Table 1 shows sample results of CE of the PVL of which spans mild, medium, and severe grades of PVL, along with their corresponding semi-quantitative assessment. The estimated severities are shown in green color for the cases in which the assessment was accurate and in red for those in which the assessment was erroneous. As it is observed, in a considerable number of cases, the semi-quantitative assessment of PVL severity failed to produce accurate predictions. More specifically, the CE of PVL was observed to over-predict the severity of PVL for mild and moderate cases. On the other hand, the CE shows to give a good estimation among the severe cases.

Table 4.1. Semi-quantitate assessment of PVL severity

	RV (ml/beat)	Actual Severity	Circ. Extent of PVL(%)	Severity based on Circ.Extent of PVL
Paravalvular Leakage	14.6	Mild	22	Moderate
	17.6	Mild	29	Moderate
	30.2	Moderate	37	Severe
	39.4	Moderate	30	Severe
	47.7	Moderate	38	Severe
	54.3	Moderate	38	Severe
	60.2	Severe	43	Severe
	63.8	Severe	47	Severe

A linear correlation shown in (Fig. 4.6) demonstrates the variation in the estimated CE of the PVL and the calculated RV in the simulation. As its evident from the R^2 in the plot, a poor correlation was found between CE and RV. The plot illustrates an over predication of the severity of PVL among the mild cases especially, however, the linear correlation can be seen among the moderate/severe and severe cases. The simulation demonstrates a new critical value of CE, i.e CE = 24 and CE = 47, can be defined as mild/moderate and moderate/severe boundary values. Note, the presented data in (Fig. 4.6) corresponds to average aortic pressure of 76.5 mmHg and left vertical pressure of 5 mmHg.

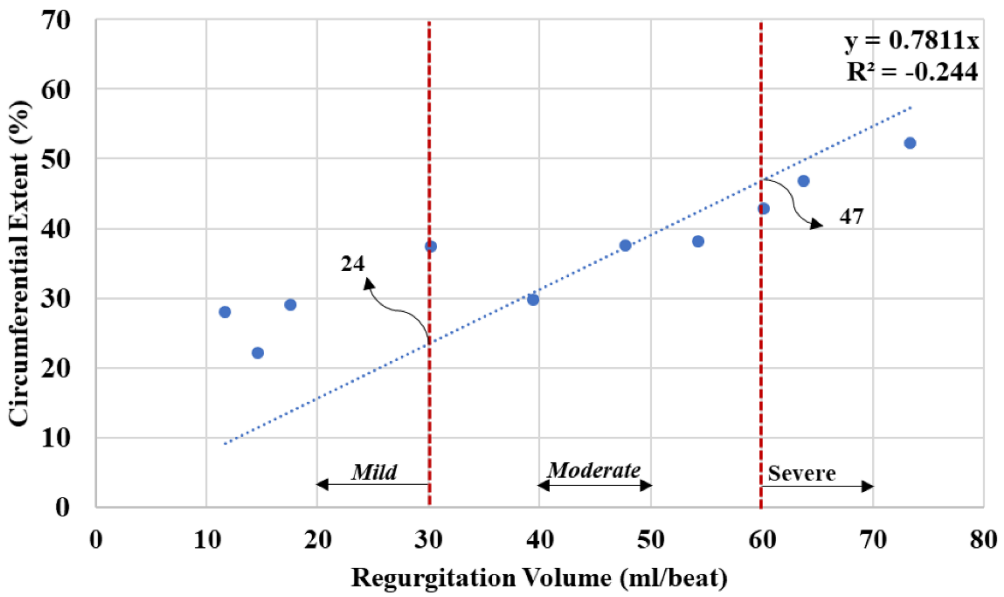

Figure 4.6: Linear correlation between the calculated RV and the estimated CE of the PVL in the CFD simulation.

The above observation highlights the requirement for quantitative assessment of PVL severity. Evidently, an ideal approach would be a comprehensive computer simulation that encompasses all the biophysical phenomena and the geometric details of the case under consideration to predict the RV accurately. However, since such computer simulation would involve time-consuming and costly processes such as the generation of the complex 3D geometry from CTA images and the CFD simulation of flow field, this study aims to propose an alternative approach that in terms of complexity, accuracy, and cost lies between the two ends, one being the semi-quantitative assessment and one accurate computer simulation. The main goal of the CFD approach is to assess in the validation of the CE of PVL, before developing the experimental setup. The proposed method is simple and is based on fluid mechanics concepts, specifically the momentum flux of the leakage.

4.3.2 Estimating Maximum Momentum Flux using CFD Simulation

After estimating the CE of PVL, the momentum flux of the leakage jets was calculated in each simulation. The momentum flux was calculated in the TAV plane as well as parallel planes that span across the TAV height. It was observed that a significant variation in the calculated momentum flux along the jets, due to the geometric confined of TAV stent and Dacron on one side and the aortic root on the other side. The jet flow in the PVL is more like a duct flow in which the duct cross section varies along the flow direction. The contractions and expansions of the duct cross section lead to increase and decrease in the leakage momentum flux, respectively. As shown in (Fig.4.1a), the flow of PVL is modeled by a contraction from the aortic side (Fig. 4.1a) to a duct entrance followed by a duct flow (Fig. 4.1a). The pressure difference between the aortic and the ventricular side drives the fluid into the duct-like chamber where it reaches its maximum velocity at the Vena Contracta (Fig. 4.1a); then the flow is confined by the TAV and aortic root geometry and it pressure/velocity varies based on the variations in the cross section of the duct.

The pressure at the vena contracta is calculated by using Equ. (1), the aortic pressure P_A is known as an input parameter for the CFD model, while the maximum velocity V_{vc} is obtained by measuring the velocity right at the inlet of the duct from the CFD results. The area of the LVOT region A_{LVOT} is found by calculating TAV areas that are occupied by high velocity regions as shown in (Fig. 4.5a). Additionally, the velocity V_{LVOT} is measured as 80% of the maximum velocity magnitude from the simulation, assuming the duct flow by a turbulent pipe flow with a relative low Reynold number (~4000). Having the values of pressure, velocity and surface area at the LVOT, the unknown value of A_{vc} can be calculated using Equ. 2, the ventricle pressure of the CFD simulation can be used as P_{LVOT}. After calculating the area of the vena contracta, the value of the maximum momentum flux of the leakage can be calculate.

Table 2 demonstrates the results for the assessment of the PVL severity using the newly proposed approach. As it is observed the new method offers significant improvements in terms of accuracy compared to the commonly used semi-quantitative method which was previously presented in Table 1. Additionally, (Fig. 4.7) demonstrates the variations in the maximum value of momentum flux, J_{max}, with the RV in the CFD simulation. As it is evident from the value of R^2 in the plot, a linear correlation exists between J_{max} and the calculated RV. The plot shows that there exists a one-to-one correspondence between the regurgitant volume of a valvular leakage and its maximum momentum flux. This indicates that the maximum momentum flux, J_{max}, can be effectively used to assess the severity of the valvular leakage. As shown in (Fig. 4.7), two critical values of J_{max}, i.e. $J_{crit,1} = 0.8$ and $J_{crit,1} = 1.57$, can be defined as the mild/moderate and moderate/severe boundary values.

Table 4.2. Assessment of PVL severity by the newly proposed approach

	RV (ml/beat)	Actual Severity	Estimated Jmax (N)	Severity Baes on Jmax
Paravalvular Leakage	11.7	Mild	0.50	Mild
	14.6	Mild	0.21	Mild
	17.6	Mild	0.38	Mild
	30.2	Moderate	0.68	Mild
	39.4	Moderate	0.89	Moderate
	47.7	Moderate	1.09	Moderate
	54.3	Moderate	1.44	Moderate
	60.2	Severe	1.59	Severe
	63.8	Severe	1.76	Severe

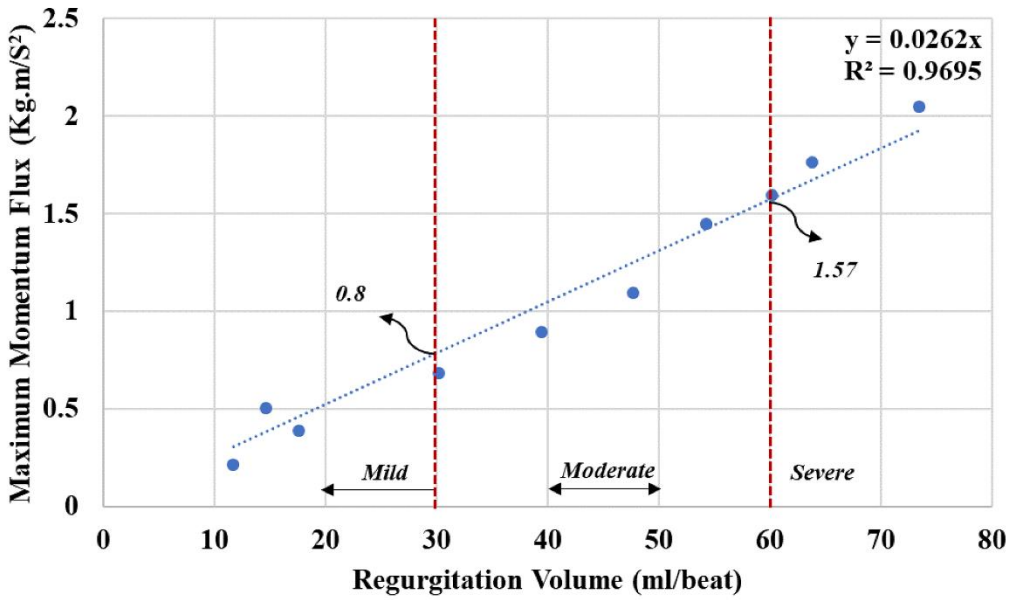

Figure 4.7: Linear Correlation between the calculated RV and the maximum momentum flux of the leakage jets.

The goal of the CFD modeling was to confirm the proposed steps in section (4.2.1) and ensure the validity of neglecting viscous loss throughout the duct. The amount of maximum momentum flux remains relatively constant past the duct under steady condition. This observation increased the desire to develop an experimental testing to compute the maximum momentum flux under pulsatile condition.

4.3.3 Estimating CE Experimentally.

In this study, first we validated the CE which is the most common method used to clinically methodology to evaluate the severity of PVL post-TAVR. The CE of PVL was estimated at 100 and 120 mmHg of mean aortic pressure. The short axis results of the color Doppler in (Fig. 4.8 a-c) demonstrate multiple cases of PVL severity in the present of multiple jets. The color Doppler images were taken at the neck of the leakage jet, right at the bottom plan of the SAPIEN 3 valve. The CE of PVL is visually estimated as the circumference of the perimeter of the TAV occupied by high flow velocity regions with respect to the total

circumference of the TAV bottom plane. The color Doppler image in (Fig. 4.8a) corresponds to a mild case with a RV of 11.46 ml/beat and a CE of 14.64 %. On the other hand, the color Doppler image in (Fig. 4.8b) corresponds to moderate case with RV of 35.74 ml/beat, and 35.21 % of the CE. The short axis image in (Fig 4.8c) corresponds to a severe case with RV of 60.25 ml/beat, and CE of 45.49%.

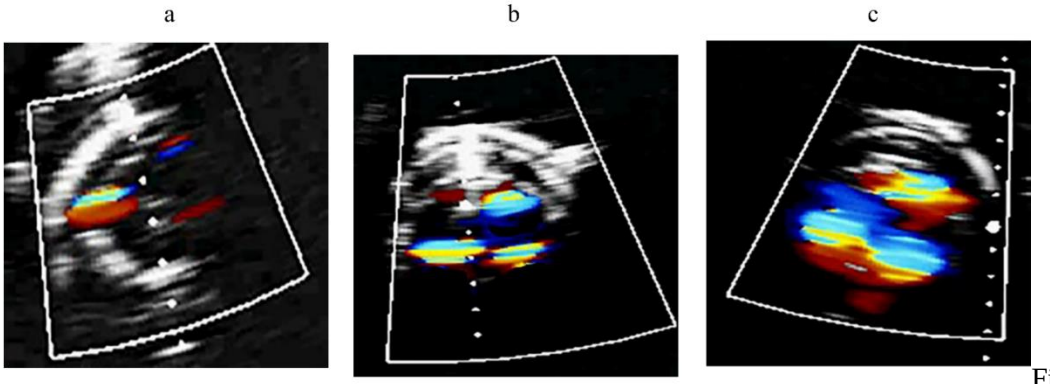

Figure 4.8: In vitro color Doppler images of multiple degrees of PVL severity were taken from the short axis view. (a) Shows results RV of 11.46 ml/beat. (b) Shows results RV of 35.74 ml/beat. (c) Shows results RV of 60.25 ml/beat

The plot in Fig. 4.9 demonstrates variations between the estimated CE with the measured RV, solid circles and empty diamond indicate to 100 and 120 mmHg of mean aortic pressure, respectively. The in vitro results of the estimated CE show poor correlation between the measured RV experimentally and the estimated CE, as its evident from the value of R^2 in the plot. Moreover, the plot indicates that a CE smaller than 24% corresponds to mild PVL, a CE bigger than 48% corresponds to severe PVL and a CE between 24%-48% corresponds moderate. Additionally, the semi-quantitative assessment of PVL severity failed to predicate the severity of PVL accurately. More specific, the CE of PVL was observed to over-predicate the severity of PVL for mild and moderate cases, in fact the plot shows a better correlation between RV and CE among severe cases comparing to mild and moderate cases. The in vitro results of CE confirm

the validity of the CFD simulation results. Additionally, it was noticed that there is no significant impact on the estimated CE from increasing aortic pressure.

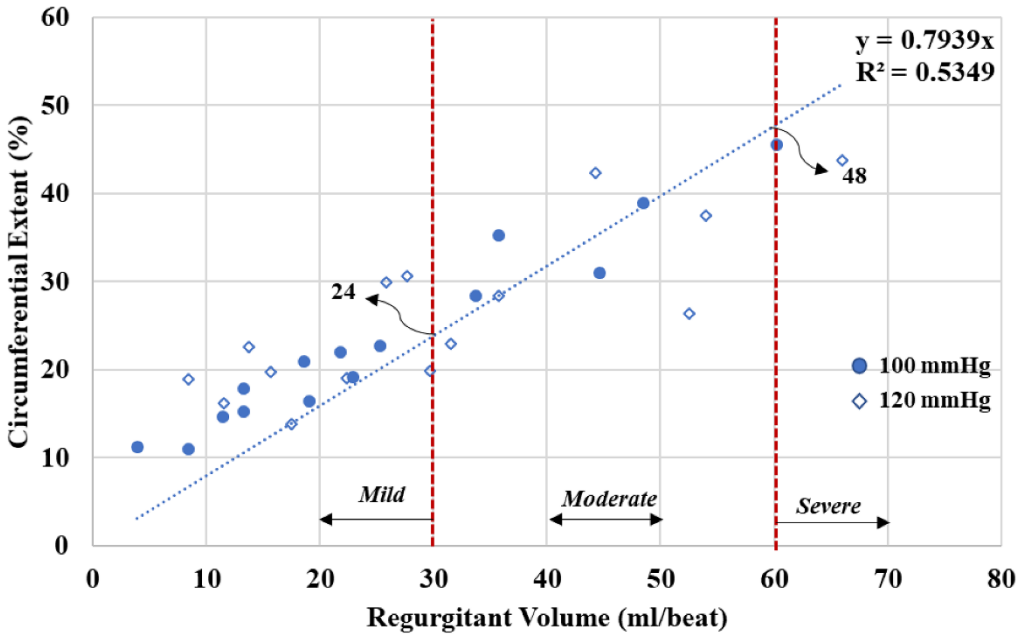

Figure 4.9: Linear correlation between the measured RV and the estimated CE obtained from the in vitro measurements.

4.3.4 Maximum Momentum Flux In Vitro

To confirm the validity of the echocardiographic parameters that were used in the new proposed method, a statistical analysis of these parameters is demonstrated in Table 4.3 at 100 and 120 mmHg of mean aortic pressure. It was observed that the measured pressure in the left ventricular increased with respect to the severity of PVL at 100 and 120 mmHg, while no change within the measured pressure in the aorta for all cases. However, left ventricular pressure increased dramatically with increasing aortic pressure Another thing that was noticed is the pressure gradient between aorta and left ventricle was decreased correspond to the level of severity, additionally, pressure gradient increases with increasing aortic pressure and it decreases with respect to the severity level. Moreover, the measured maximum velocity decreases with

respect the severity of PVL. Maximum velocity magnitude increases with increasing aortic pressure as it illustrated in Table 4.3.

Table 4.3: Hemodynamics measurements from the in vitro testing with different level of severity

Parameters	Aortic pressure at 100 mmHg			Aortic Pressure at 120 mmHg		
	Mild	Moderate	Severe	Mild	Moderate	Severe
LV pressure (mmHg)	32.89±6.5	35.23±2.4	49.06±0	37.65±6.9	39.53±6.6	56.89±0
Pressure Gradient (mmHg)	69.71±6.0	65.49±3.9	52.38±0	86.24±6.3	83.56±6.6	64.21±0
Maximum Velocity (m/s)	4.63±0.22	4.61±0.12	4.30±0	5.27±0.33	4.92±0.26	4.30±0

The maximum momentum flux of the leakage jets was calculated at 100 and 120 mmHg of mean aortic pressure. The estimated momentum flux was calculated with respect to the vena contracta of the duct flow which corresponds to detect the maximum forces presenting in the duct flow. The echocardiographic images in (Fig. 4.10) are sample with different level of PVL severity, those images were used to estimate parameters that used to calculate momentum flux in the leakage jets. In Fig. 4.10a demonstrates a mild case with RV of 13.60 ml/beat, Fig. 4.10b shows a moderate case with RV of 46.65 ml/beat and Fig. 4.10b shows a severe case with RV of 64.32 ml/beat. The color doppler images (Fig 4.10) were used to estimate the area at the LVOT region, image processing was performed to calculate the area of the TAV high velocity occupied areas. The middle raw in Fig. 4.10 demonstrates pulse wave velocity measurement from long axis view, the blue arrow indicates systole while the red arrow indicates diastole. A caliper tool in echocardiography was used to measure velocity at the LVOT region, PW measurements at the LVOT region. The bottom raw in Fig. 4.10 illustrates maximum velocity of the leakage jets was captured using CW doppler, which corresponds to the velocity at the vena contracta. Velocity time integral (VIT) was used to measure the average maximum velocity magnitude along the jets.

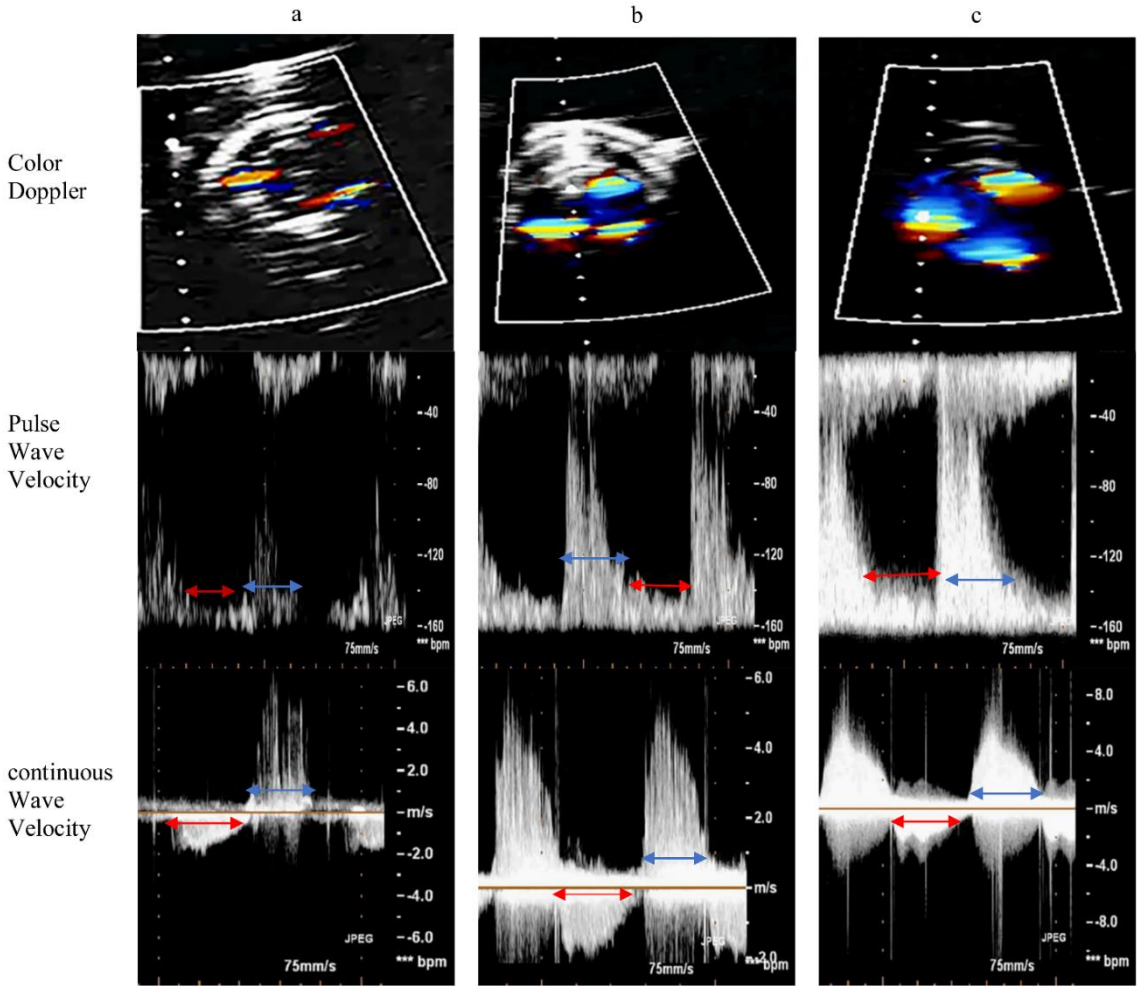

Figure 4.10: A sample of echocardiographic obtained from different level of PVL severity. (a) a mild case with RV of 13.60 ml/beat. (b) a moderate case of 46.65 ml/beat. (c) a severe case of 64.32 ml/beat. The first top raw shows color doppler of the LVOT area. The middle raw shows pulse wave velocity images at the LVOT area. The bottom raw shows continuous wave of the velocity magnitude at the vena contracta.

The plot in Fig. 4.11 demonstrates linear correlation between the measured RV and the calculated momentum flux, the solid circles presents data of 100 mmHg while empty diamonds presents data of 120 mmHg. A significant linear correlation exists between RV and momentum flux, as it is evident from the R^2. The plot in Fig. 4.11 shows that there exists a one-to-one correspondence between the measured RV of a PVL and its maximum momentum flux. This indicates that the maximum momentum flux, J_{max}, can be used to estimate the severity of PVL.

As shown in Fig. 4.11 two critical values of J_{max}, i.e. $J_{crit,1} = 1$ and $J_{crit,2} = 2$, can be defined as the mild/moderate and moderate/severe boundary values. Furthermore, it was observed there is no significant impact on momentum flux from increasing of aortic pressure as it shown in Fig. 4.11.

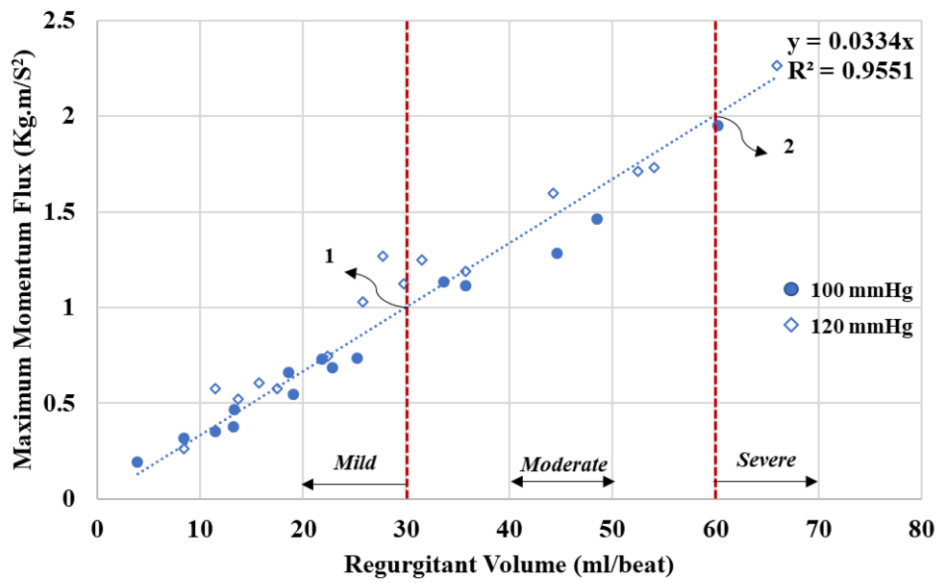

Figure 4.11: Correlation between regurgitant volume (RV) and the maximum momentum flux of PVL. Empty diamond corresponds to mean aortic pressure of 120 mmHg. Filled circles correspond to mean aortic pressure of 100 mmHg.

4.4 Discussion

4.4.1 Summary

Due to the natural of TAVR implantation procedure, PVL is one of the most common clinical issues associated with TAVs devices. The severity of PVL was graded as mild, moderate and severe according to the American Society of Echocardiography recommendation for evaluation native (Zoghbi et al., 2009). Measuring the amount of PVL per beat is the accurate way to evaluate the severity of PVL, however, measuring CE of PVL is consider an alternative solution to evaluate PVL severity due to difficulty to measure the regurgitation volume (Zoghbi et

al., 2009). Nevertheless, the CE of PVL totally depends on capturing accurate images right at the bottom level of TAV device. However, in case of multiple jets are presented, CE can be misleading to estimate the severity of PVL. In the same manner, the CE has not been validated, therefore, the PVL volume of a given CE is basically unknown. In this study, first we validated the CE via CFD and in vitro investigation. Also, we introduce a new method based on fluid dynamics to estimate PVL severity.

4.4.2 Validation of CE

In this chapter, an experimental setup was used to validate the most common methodology that uses to estimate the severity of PVL post-TAVR procedure. To the reader knowledge this is the first study that focused on validating CE with respect to different level of severity experimentally. The CFD simulation was used to validate the CE guide, multiple PVL severities were tested by increasing and decreasing the size of the gap as it shown in (Fig. 4.2). The presented results of the CFD simulation indicates poor correlation between the calculated RV and the estimated CE. The plot in Fig. 4.6 demonstrates that the CE overestimate the severity of PVL. The result obtained from the CFD simulation support the clinical outcomes of several studies (Pibarot et al., 2015, Hayek, 2014 #110). Additionally, an experimental setup was developed to confirm the validity of the CFD simulation. Like the CFD, different level of PVL severities were examined by increasing and decreasing the circumference of the introduced gaps in (Fig. 4.3c). The in vitro result demonstrates a weak correlation between the measured RV and the estimated CE. Also, the plot in (Fig. 4.9) illustrates that CE method overestimate the severity of PVL. The boundary critical values for classification of PVL severity obtained from the in vitro result match the CFD results, those values do not match the critical values presented in (Geleijnse et al., 2015; Zamorano et al., 2011). Therefore, the in vitro results confirm the invalidity of the

CE method. Therefore, developing a new approach based on fluid dynamic was highly encouraged to develop an accurate way of estimating the severity of PVL post-TAVR.

In this study we proved that the CE method overestimate the severity of PVL, many clinical data have suggested that totally depending on short axis images to estimate the severity of PVL could be misleading. One of the most challenging associated with capturing images of PVL is the moment to capture the location of leakage. In diastole, the base of the heart moves far away from the heart apex (Zoghbi et al., 2009). Another issue is that in the present of multiple PVL jets, different location might not be seen in one beat, but it can be seen in other phases of the beat or in a different beat. This will lead to overestimate the real severity of PVL, even though in some cases of a rocking TAVs PVL severity is most likely to be severe and not overestimated (van Dalen et al., 2009).

4.4.3 Maximum Momentum Flux

In this chapter, we also introduced a new method based on estimating the maximum momentum flux of the PVL leakage to evaluate the severity of PVL using parameters that are currently being used to evaluate the severity of PVL. The maximum momentum flux is a combination of the mass flow rate and the maximum velocity that driven the flow in the PVL leakage. The new approach showed a significant correlation with respected to the measured RV in CFD simulation and in vitro results with high value of R^2. Both results demonstrate similar boundary critical values between mild to moderate and moderate to severe as it shown in (Fig. 4.7) and (Fig. 4.11), which indicate the robust of the introduced approach. As we shown previously that CE is not an accurate method to estimate the severity of PVL, and the obtained critical values do not match those were introduced in the current guideline (Jilaihawi et al., 2012; Zamorano et al., 2011). Moreover, the result obtained from the in vitro indicates no significant variation between the estimated momentum flux and increasing of the mean aortic pressure as it

shown in (Fig. 4.11). The plot in Fig. 4.11 shows that the momentum flux approach not only can be used among patients with normal aortic pressure, even among patient with high blood pressure. To the reader knowledge this is the first study that introduce and validate a new simple approach based on fluid dynamics by using echocardiographic parameters.

Furthermore, the good agreements between CFD simulation and in vitro results in term of calculating maximum momentum flux of the PVL jets, confirm the validity of our assumption by neglecting the viscus forces of the flow in the duct. The in vitro result indicates that the measured pressure in LVOT region increases with increasing RV, however, the measured aortic pressure was not influenced with the severity of PVL. Additionally, Table 4.3 demonstrate a significant increase of the LVOT pressure with increasing the aortic pressure. High severity of PVL could lead to heart failure due to expansion in the LV wall, especially when the LV exposes to high pressure. On the other hand, the results obtained by echocardiography demonstrate that the captured area in LVOT region changes significantly with respect to the applied pressure and the duct size of the washer, however CE and PW velocities was remaining similar.

Currently several techniques can be used to estimate the severity of PVL post-TAVR procedure, including magnetic respond imaging, cineangiography, aortic regurgitation index and doppler echocardiography, however each of these techniques has its own limitation and technical difficulties (Zoghbi et al., 2009). Classification of PVL based on hemodynamics measurements can be challenging due to the natural of the PVL jet. Our experimental data shows the possibility to estimate the severity of PVL without measuring RV of the leakage directly. Nevertheless, a recent study addresses a way to estimate the severity of PVL by printing a 3D model of the patient-specific geometry (Pibarot et al., 2015). However, the accuracy of the gap sizes might be not accurate due to smoothing and removing difficult part to print, also the whole procedure is

time consuming. Therefore, in this study we believe that the presented method provides well and accurate way to generate multiple severity by controlling gap sizes as in (Fig. 4.3c). On the other hand, a similar study suggested that increase mean aortic pressure lead increase in PVL RV (Ripley et al., 2016). However, our experimental result shows no significant increase in RV with respect to 100 and 120 mmHg.

4.5 Conclusion

In summary, TAVR has been introduced as an alternative procedure to surgical replacement of aortic valve with less recovery time to SAVR. However, PVL is a frequent clinical issue associated with TAV implantation procedure. Quantifying the severity of PVL clinically is still challenging due to complexity of the PVL jets . CE is the most common technique to estimate the severity of PVL. Nevertheless, in this chapter we demonstrated that CE indicates to over-estimate the severity of PVL. Additionally, we introduced a new approach to estimate the severity of PVL based on estimating maximum momentum flux of the PVL jets. The new approached showed a good linear correlation with the measured RV. Therefore, the maximum momentum flux approach is a more accurate method to evaluate the severity of PVL post-TAVR procedure.

Chapter 5: Quantification the severity of Paravalvular Leakage Based on Energy Loss

5.1 Introduction

Transcatheter aortic valve replacement (TAVR)is a less invasive procedure for aortic valve replacement targeting selected patients whom considered risky for open-heart surgery, recently the Food and Drug Administration (FDA) approved that younger patients can be considered for TAVR (Tanaka et al., 2018). The transcatheter aortic valve (TAV) devices provide similar benefits to surgical valve for patient who cannot undergo a surgical valve replacement (Coylewright et al., 2020; Cribier et al., 2002; Grube et al., 2007) to receive treatment. Several clinical studies have shown that TAVs provides superior systolic performance in term of mean pressure gradient and effective orifice area (Clavel et al., 2009; Daubert et al., 2017; Webb et al., 2007). However, paravalvular leakage (PVL) is a frequent clinical complication post-TAVR, compared to surgical aortic valve replacement rarely (-6%) (Hahn et al., 2013; Ionescu, Fraser, & Butchart, 2003). Mild to Moderate PVL might have little clinical impact among older patients whom life expectancy is limited, however this degree of PVL severity will lead to more serious clinical impact among TAVR younger patients. It has been illustrated that PVL is associated with hemolysis and endocarditis even with mild PVL which result in ventricular dysfunction (Bhindi, Bull, Schrale, Wilson, & Ormerod, 2008; Pibarot et al., 2015). Therefore, qualifying the severity of PVL accurately is quite significant for clinical decisions.

Measuring hemodynamic performance of TAV such as blood velocity, pressure gradient and effective orifice area could be used to evaluate the severity of PVL post-TAVR. However,

none of these parameters take into consideration of measuring PVL volume. Based on these parameters current TAV devices match and may even excessed the performance of surgical valve(Azadani et al., 2009; Maraj, Jacobs, Ioli, & Kotler, 1998). Nevertheless, none of these parameter take in consideration to evaluate the severity of PVL. Therefore, in this study we develop a new methodology by using Doppler echocardiograph parameters that provides an accurate estimation to quantify the severity of PVL based on the concept of energy loss. Evaluating the performance of TAV devices depend on measuring hemodynamic parameters such as pressure gradient, blood velocity and effective orifice area. Based on these parameters, TAV devices match and may exceed the hemodynamic performance of surgical valves (Barakat et al., 2018; Clavel et al., 2009). On the other hand, the circumferential extent and ½ pressure time of PVL are the semi-quantitative parameters currently used to estimate the severity of PVL during diastole (Walther & Falk, 2009). However, more recent data have demonstrated the accuracy of energy loss in examine the performance of TAV devices (Akins, Travis, & Yoganathan, 2008; Azadani et al., 2009; Pibarot et al., 2015).The energy loss concepts provide more accurate criteria to evaluate and examine the total hemodynamic performance of TAV devices during the entire cardiac cycle, and the effect of left ventricle workload during diastole (Garcia, Pibarot, Dumesnil, Sakr, & Durand, 2000, Garcia, 2000 #12, Azadani, 2016 #122). In the cardiac cycle, the energy exists in two forms: potential (in the form of pressure or height) and kinetic energy (in the form of velocity). Color doppler imaging of PVL jets diameter and length illustrate in a semi-quantitate way the kinetic energy across the TAV devices. Nevertheless, the summation of potential and kinetic energy losses must be taken in consideration to evaluate the severity of PVL and to determine the workload on the left ventricular. Additionally, substantial energy loss was measured with TAV devices during diastole, even with mild PVL, TAVs implantation show higher workload on the left ventricle than surgical implanted bioprosthesis (Akins et al., 2008). Moreover, the energy loss has the potential to estimate the severity of aortic stenosis better than

other semi-quantification parameters (Azadani et al., 2009). However, none of these studies have considered measuring energy loss with respect to RV to address the appropriate classification of PVL severity. In this study, we developed two methodologies to measured energy loss invasively and non-invasively during the entire cardiac cycle and comparing invasive energy loss to non-invasive energy loss.

5.2 Material and Method

5.2.1 Energy loss Approach

In this study, we measured transvalvular energy loss in both invasive and non-invasive for different degrees of severity of PVL during systole. The measured invasive energy loss is based on the fundamental of conservation of energy. The invasive energy loss was measured by measuring the instantaneous of flow (Q_{valve}) and instantaneous of pressure gradient (ΔP) using the pulse duplicator based on the formula listed in Table 1 for both systole and diastole. The pressure gradient measured using pressure transducer and the flow measured using flow transducer as it shown in Fig 3. Where $t_{early-systole}$ the beginning of the forward flow through the valve, $t_{end-systole}$ is the end of the forward flow through the valve, $t_{early-diastole}$ is the time of valve closure and $t_{end-diastole}$ is the end of the cardiac cycle. The total invasive energy loss was the sum of the energy loss in systole and diastole.

The non-invasive formal was driven from conservation of mass, energy and momentum. The systolic non-invasive energy loss measurements were performed based on measuring the maximum velocity of the SAPIEN 3 jet (V_{jet}) during systole using CW Doppler from long axis view, the effective orifice area (EOA) was measured instantaneously using LABVIEW software (BDC Labs, Wheat Ridge, CO, USA) based on Gorlin equation, and 40 mm cross-section area of the aorta (A_A). On the other hand, the diastolic non-invasive energy loss measurements were performed based on measuring V_{vc} using CW Doppler, ρ is the density of the running solution,

RV was measured instantaneously using the flowmeter and K was calculated based on the diastolic invasive energy loss measurements. The total non-invasive energy loss was the sum of the energy loss in systole and diastole.

Table 5.1. Illustrates invasive and non-invasive energy loss formulas for the cardiac cycle.

Energy loss measurements	Invasive Energy Formulae	Non-invasive Energy Formulae
Systolic energy loss ($^{\Phi}$Systole)	$\int_{t_{early\ systole}}^{t_{end\ systole}} Q_{valve}.\ \Delta P$	$\int_{t_{early\ systole}}^{end\ systole} \frac{\rho V_{jet}^2 . EOA}{2} . \left(1 - \frac{EOA}{A_A}\right)^2$
Diastolic energy loss ($^{\Phi}$Diastole)	$\int_{t_{early\ diastole}}^{t_{end\ diastole}} Q_{valve}.\ \Delta P$	$k.\rho.RV_{leakage}.\frac{V_{vc}^2}{2}$
Invasive Energy Estimation $Q_{leakage}$ is the instantanous flow through the valve measured using electromagnetic flowmeter in vitro. $\Delta P_{leakage}$ is the instantaneous pressure gradient across the valve using pressure transducer.	**Non-invasive Energy Estimation** ρ is the blood density, V_{vc} is the maximum velocity of the leakage jets measured using CW doppler, $RV_{leakage}$ is the regurgitation volume estimated from $\int max.k$ is the regurgitation coefficient calculated based on the invasive energy measurements. EOA is the effective orifice area, A_A is the aortic cross section area.	

5.2.2 Heart valves and PVL Model

To mimic the flow characterization in PVL, a 3D printed washer was used by introducing anatomically realistic gaps was between the TAV geometry and the native TAV commissures (Fig. 5.1a). A 26 mm SAPIEN 3 was implanted within the inner diameter of the 3D printed washer (Fig. 5.1b) and placed in the aorta side. Also, a bileaflet mechanical heart valve was placed at the mitral position. The 3D printed washer has an outer diameter of 40 mm, inner diameter labeled as the SAPIEN 3 and height of 16 mm. chamber. The stages of PVL severity was controlled by increasing and decreasing the circumference of the gaps, however, the gap width was kept at 2 mm. The flow inside the gaps are govern by the pressure gradient between aorta and left ventricle (Fig. 5.1c) chambers. The flow jet reaches its maximum velocity

at the entrance of the duct . After that, the flow is confirmed by TAV's geometry and the left ventricle chamber, pressure and velocity based on the variation of the duct size.

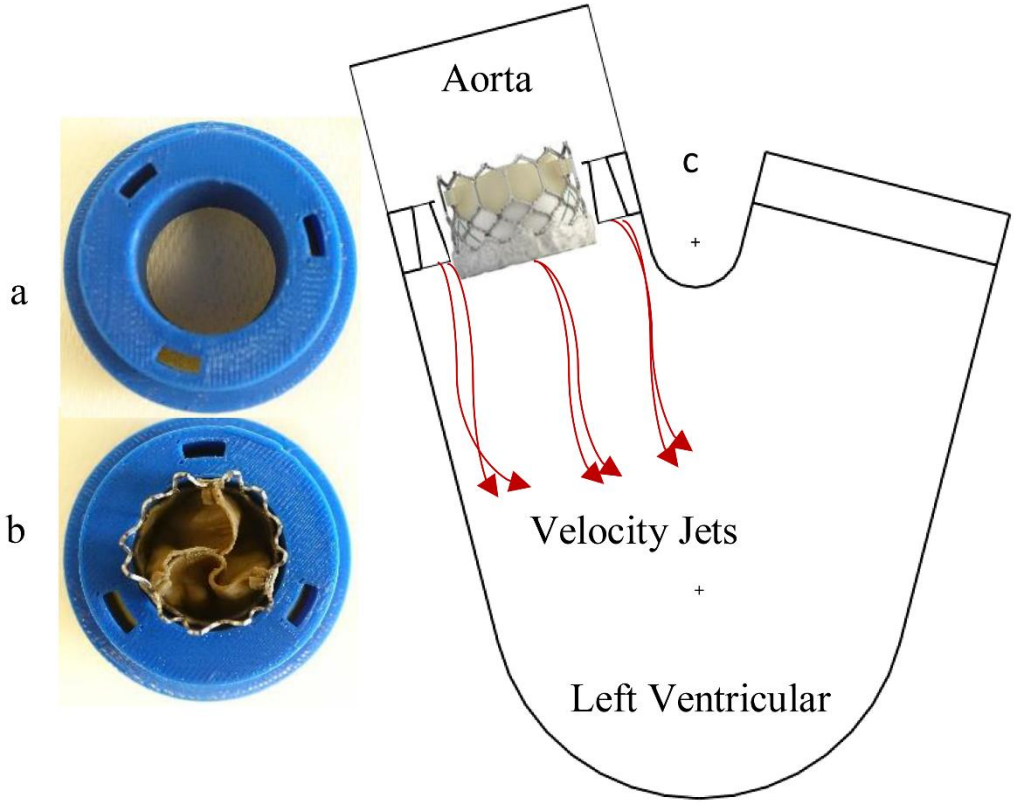

Figure 5.1: (a) 3D-printed washer with 3 gaps. (b) A 26 mm Edwards SAPIEN 3 implemented within the 3D-printed washer. (c) schematics show the flow through PVL channel.

5.2.3 In Vitro testing of TAVs

Multiple gaps size was tested in a custom-build pulse duplicator at room temperature developed for heart valves testing (BDC Labs, Wheat Ridge, CO, USA) to obtain different PVL severity stages. A Recirculating fluid of 36% by volume glycerin solution in phosphate buffered normal saline solution which mimics blood viscosity and density at 37 °C was used as a blood analog fluid. Flow circulation was simulated through silicon ventricular contraction, control of

compliance and peripheral resistance. Our pulse duplicator system was previously descripting in more detail and validated (Garcia et al., 2000). The pulse duplicator input parameters matched the international standard ISO 5840: 2015 recommendations for testing prosthetic heart valves; that is, heart rate of 70 beats/min, mean aortic pressures of 100 mm Hg, and cardiac output of 5 L/min. these hemodynamics parameters were maintain constant through the experiment. Pressure was measured in the aorta and left ventricle using strain gauge pressure transducers (Utah Medical Products, Midvale, UT, USA). pressure measurements were taken at 105 mm downstream and 35 upstream of the valves for aortic and left ventricle respectively. Additionally, pressure transducers were calibrated prior to the tests using Delta-Cal Pressure transducer simulator/tester (Utah Medical Products, Inc). In addition, an electromagnetic flowmeter (Model 501, Carolina Medical Electronics Inc, East Bend, NC, USA) was located on top of the aortic valve and used to measure the regurgitation mass flow rate of the RV in the system. Additionally, iE33 ultrasound system (Philips Medical Systems, Andover, Massachusetts) and a V-219 (2.5 MHz) was used to measure the velocity of PVL.

Figure 5.2: A custom-built pulse duplicator system (BDC Labs, Wheat Ridge, CO)

5.3 Results

5.3.1 Invasive energy loss

The invasive energy loss was measured directly from the data obtained from the pulse duplicator throughout the cardiac cycle. First, energy loss was measured at normal mean aortic pressure of 100 mmHg, second, energy loss was measured at mean aortic pressure of 120 mmHg. The pressure and flow curve in (Fig. 5.3) correspond to moderate case with RV of 48.51 ml/beat. The blue sold line presents the instantaneous left vernacular pressure, while the dash red line presents the instantaneous aortic pressure in (Fig. 5.3a). The green sold line corresponds to the measured flow as it shown in(Fig. 5.3b). The pressure gradient was directly calculated by subtracting left ventricular pressure from aortic pressure. The mean value of the pressure gradient was used to measure the energy loss. Additionally, the volume of the leakage was considered as the red area of the flow during diastole as it shown in (Fig. 5.3). The mean value of the flow was used to measured energy loss. Moreover, the experimental data shows a significant increase in the left ventricular pressure with increasing RV, which led to drop in the pressure gradient.

Fig. 5.4 demonstrates the variation in the measured energy loss invasively with the RV. The plot shows a linear correlation between the measured RV and energy loss by using the equation in Table 5.1, as it is evident from the value of R^2. Note that both the presented data corresponds to mean aortic pressure of 100 mmHg and 120 mmHg in Fig 5.4. The data in the graph indicates that energy loss increases with increasing aortic pressure especially with moderate and severe cases. However, according to the plot in Fig. 5.4, there is matching values of the measured energy loss at 100 and 120 mmHg in the mild section especially. Additionally, two critical values for quantifying the severity of PVL based on energy loss can be defined as, energy loss between 318-635 mJ correspond to moderate, below 318 mJ and above 635 mJ correspond to mild and severe, respectively. The linear correlation in Fig. 5.4 shows that there exists a one-one

correspondence between RV of a PVL and its energy loss. Moreover, the bar charts in (Fig. 5.5) demonstrate that the energy loss during diastole increases with increase PVL severity, however, there is no direct correlation between systolic energy loss and PVL severity.

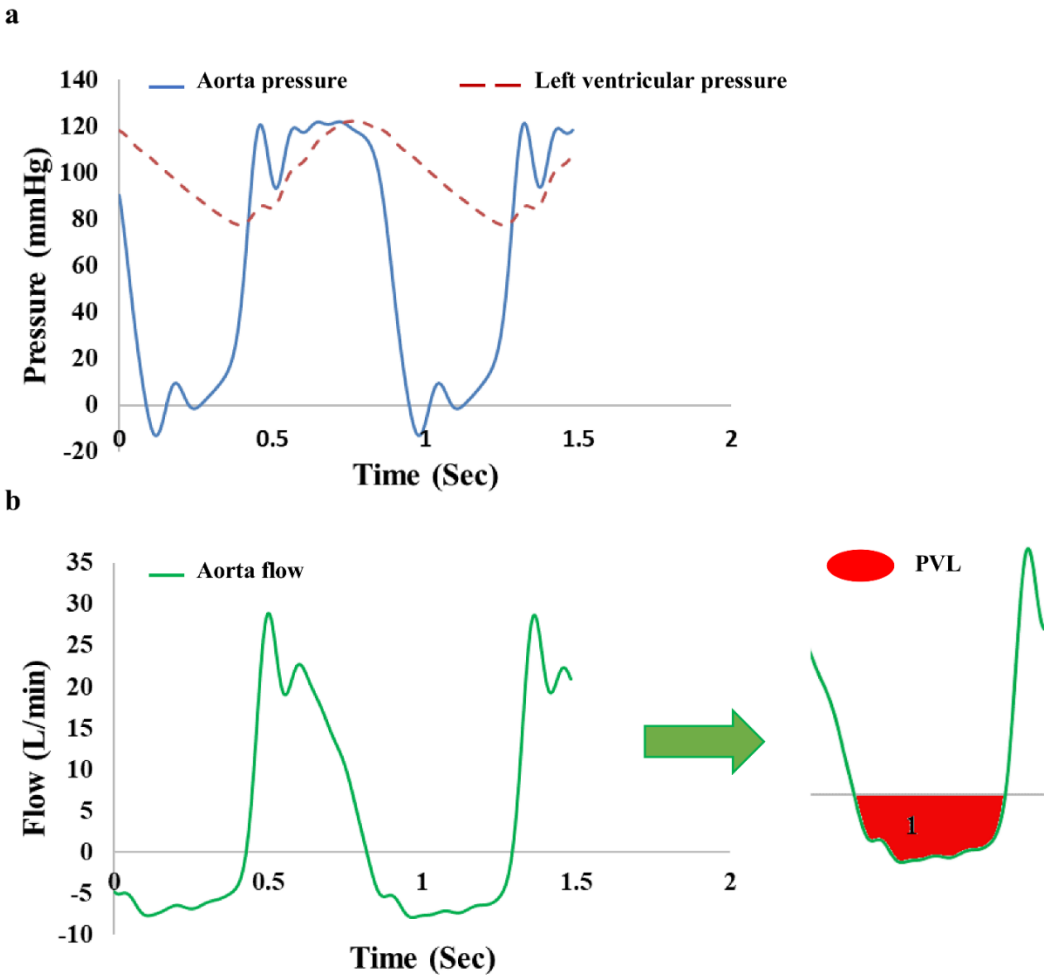

Figure 5.3: Pulse duplicator result with RV of 48.51 ml/beat. (a) pressure waveform of one cardia cycle at mean aortic pressure of 100 mmHg, the blue sold line corresponds to aortic pressure, the red dash line corresponds to left ventricular pressure. (b) the measured flow rate across the aortic valve during the cardiac cycle, on the right, the red area in the right image shows the amount of leakage during diastole.

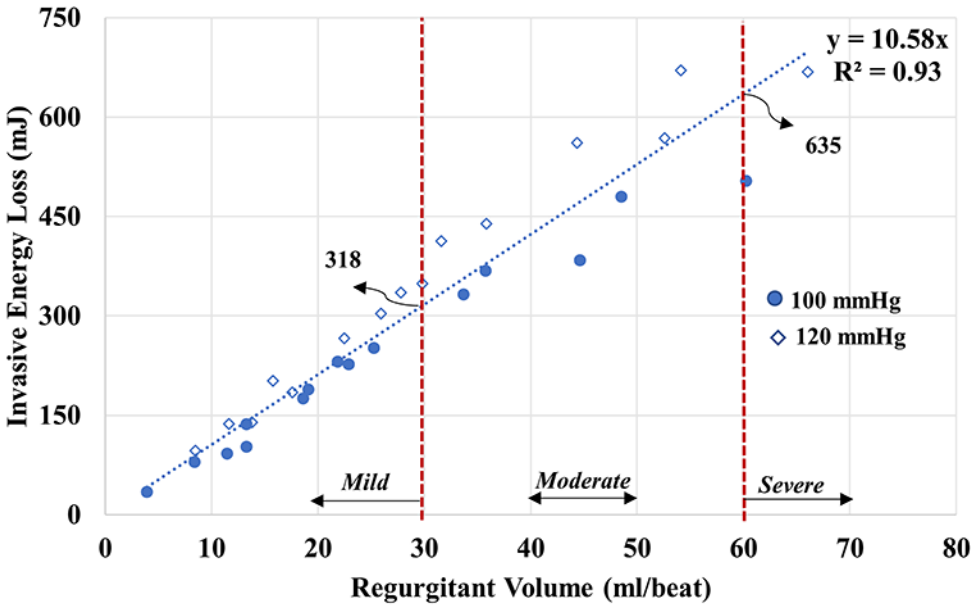

Figure 5.4: Linear correlation between the measured regurgitation volume and the measured energy loss invasively. Solid blue circle and empty diamond correspond to measured energy loss at mean aortic pressure of 100 mmHg and 120 mmHg, respectively.

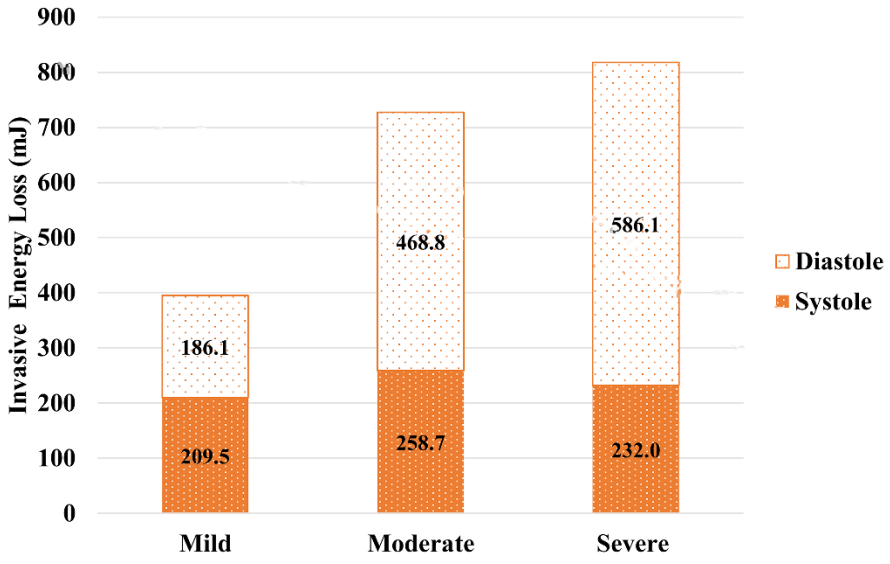

Figure 5.5: Chart bar shows the measured total energy loss invasively per cardiac cycle.

5.3.2 Non-invasive energy loss

After measuring the energy loss invasively for multiple degree of PVL severity, the data obtained from the echocardiography was used to measure energy loss non-invasively. The energy loss was calculated at normal and high mean aortic pressure 100 mmHg and 120 mmHg, respectively. The Echocardiography images in Fig. 5.6 demonstrate a moderate case with RV of 48.51 ml/beat. Long axis of the velocity jets is shown in Fig. 5.6a. The maximum velocity was measured using CW Doppler along the velocity jet as it shown in Fig. 5.6b, the blue arrow indicates diastolic velocity while red arrow indicates systolic velocity. The energy loss was calculated based on the listed equation in Table. 1 non-invasive column throughout the cardiac cycle. To calculate energy loss during diastole, Vvc was measured directly in the echocardiography using velocity time integral function, while RV was directly measured in the pulse duplicator. The regurgitation coefficient (K) value was calculated based on the measured energy loss invasively. While the density was used as the running solution which is around 1.102 g/cm. On the other hand, the effective orifice area (EOA) was directly measured in the pulse duplicator based on Gorline equation.

Fig. 5.7 demonstrates the variation in the calculated energy loss non-invasively with respect to the measured RV. The plot shows a linear correlation between the calculated energy loss based on the equation listed in Table 5.1 during diastole. An excellent correlation between the measured RV and the calculated energy loss was observed, as its evident from the R^2. The plot shows values of energy loss correspond to mean aortic pressure of 100 and 120 mmHg solid blue circle and empty diamond, respectively. Additionally, two critical values for quantifying the severity of PVL based on energy loss can be defined as, energy loss between 255-510 mJ correspond to modetrate, below 255 mJ and above 510 mJ correspond to mild and severe, respectively. The linear correlation in Fig. 5.7 shows that there exists a one-one correspondence

between RV of a PVL and its energy loss. Moreover, the bar charts in (Fig. 5.5) demonstrate that the energy loss during diastole increases with increase PVL severity, however, there is no direct correlation between systolic energy loss and PVL severity.

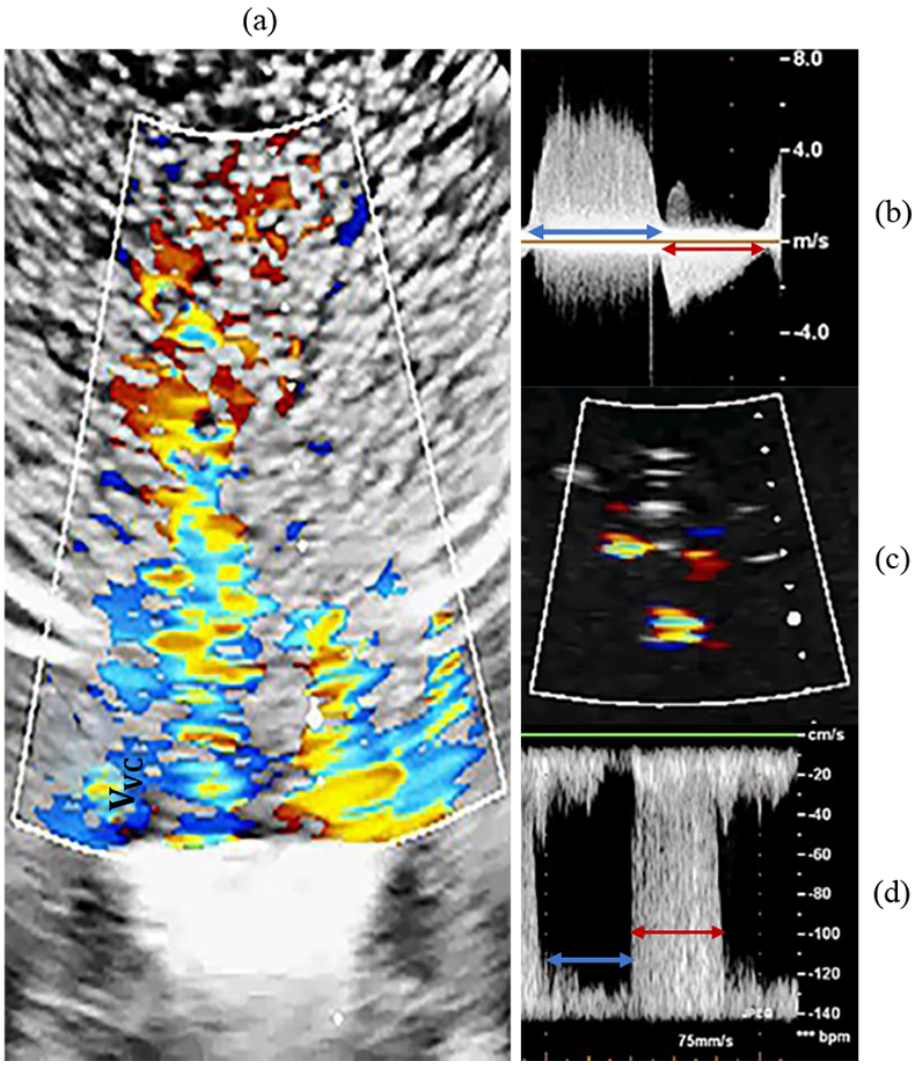

Figure 5.6: A sample of echocardiography parameters that were used to estimate the maximum momentum flux. (a) Long axis view of the velocity jet, illustrating measurement locations. (b) CW Doppler measurement of the maximum velocity of the jet at the vena contracta, red arrow corresponds to systole and blue corresponds to diastole. (c) Short axis view of the area of the jets in the LVOT region. (d) PW Doppler measurement of velocity magnitude at the location where the area was estimated.

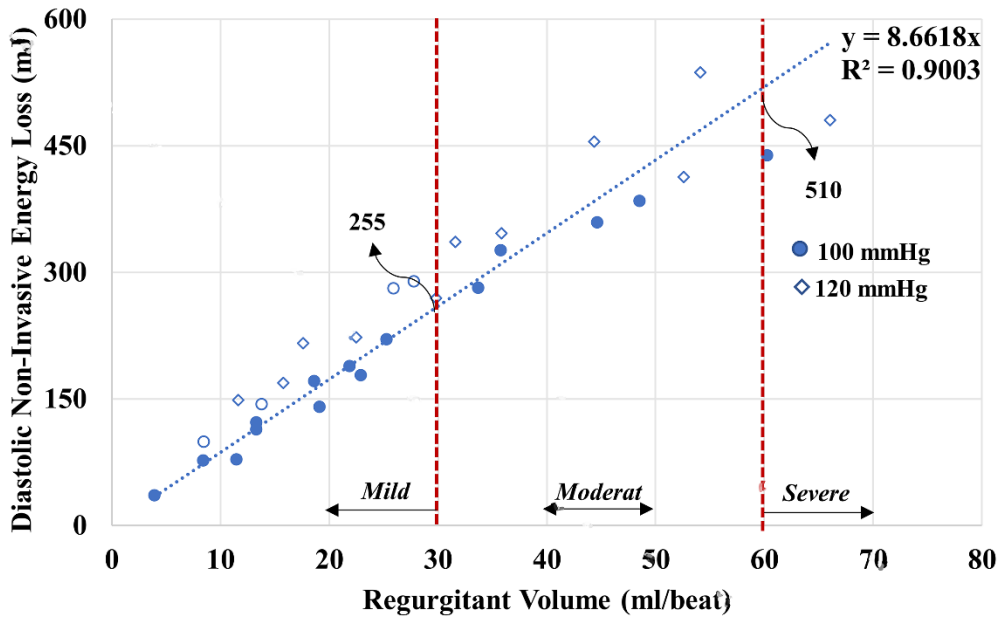

Figure 5.7: Linear correlation between the measured regurgitation volume and the calculated energy loss non-invasively. Solid blue circle and empty diamond correspond to measured energy loss at mean aortic pressure of 100 mmHg and 120 mmHg, respectively.

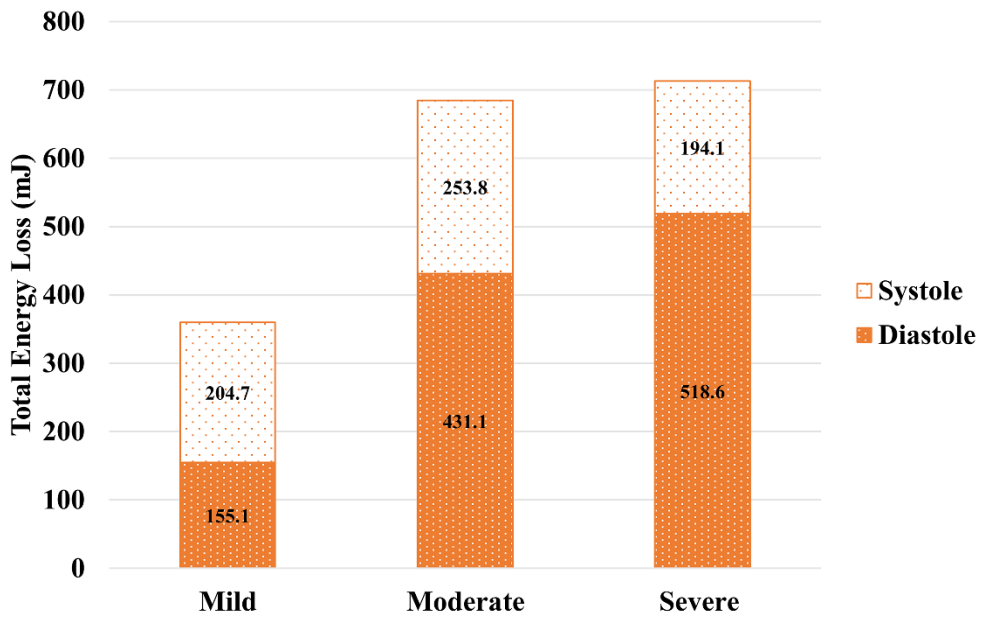

Figure 5.8: Chart bar shows the calculated total energy loss non-invasively per cardiac cycle.

5.4 Discussion

5.4.1 Summary

In the previous chapter we illustrated that the CE of PVL over-estimate the severity of PVL, therefore we introduced a new methodology based on estimating the maximum momentum flux of the PVL jet. In this chapter we introduce a new methodology based on the concept of energy loss to quantify the severity of PVL. The concept of energy has been introduced before to assess the severity of valvular stenosis (Barakat et al., 2018). In this study, energy loss was measured invasively and non-invasively, the invasive energy loss measurement was performed directly from the pulse duplicator using the instantaneous pressure and flow measurements. While the non-invasive energy loss was measured directly from the data obtained from the echocardiography. It was observed that energy loss has an excellent correlation with the measured RV during diastole. The non-invasive energy loss estimation can be very helpful in determining the severity of PVL accurately. Several studies indicate that measuring hemodynamic performance of valvular leakage by measuring energy loss (Akins et al., 2008; Garcia et al., 2000). However, to the reader knowledge, this is the first study that introduced and validated two formula of energy loss invasively and non-invasively.

5.4.2 Energy loss Measurements

Energy loss is a well-founded engineering concept which allows assessment of bioprosthetic heart valve performance during systole, and accounts for the impact of leakage during diastole (Azadani et al., 2009). Evaluation of PVL severity based on energy loss provides more detailed information than currently available semi-quantitative methods (Akins et al., 2008; Zamorano et al., 2011). Totally depending on semi-quantitative parameters can be misleading, especially under low cardiac output. This study demonstrates a one to one corresponding between the measured energy loss invasively experimentally and the estimated energy loss non-invasively

by echocardiography during diastole. Therefore, a good matching fitted line of $R^2 = 0.97$ between invasive and non-invasive energy loss with a slop of 0.9, which means the measured energy loss in vitro and Doppler are almost identical as it shown in (Fig. 5.9). In this way, as the workload on the left ventricle increases, the ventricle becomes the interest of evaluation. Additionally, In the present of PVL, the ventricle must increase its systolic pressure and volume to compensate the lost energy to maintain blood flow at a constant rate. PVL results in high stress applied into the ventricle wall which could lead into a heart failure. Measuring energy loss is an excellent way to estimate the severity of PVL and demonstrates the increase in workload on the ventricle. Nevertheless, the concept of energy loss has not been mostly used clinically since its direct estimation requires complex and invasive measurements of pressure and velocity (Zoghbi et al., 2009).

In this study, the energy loss during systole was calculated as well, however there is no direct correlation between systolic energy loss and RV. (Fig. 5.10) shows a one to one corresponding between the total energy loss invasively and noninvasively $R^2 = 0.94$ and a slop of 0.9. The linear correlation in (Fig. 5.10) indicates the possibility of using the totally energy loss to evaluate the severity of PVL. Classifying the severity of PVL post TAVR based on energy loss provides more detailed information than the currently semi-quantification methods by studying the performance of the entire cardiac cycle. However, measuring energy loss clinically requires complex and invasive measurement. Therefore, in this study we developed a non-invasive approach by using echocardiography to measure energy. The in vitro energy loss measurements show an excellent agreement with the measured energy loss using echocardiography. This is a combination study to assess and quantify the severity of PVL by using maximum momentum flux and energy loss concepts. Measuring RV is the most accurate way to determine the severity of

PVL, however, it's an invasive and expensive procedure. Therefore, the maximum momentum flux can be used to estimate RV, to measure energy non-intensively during diastole.

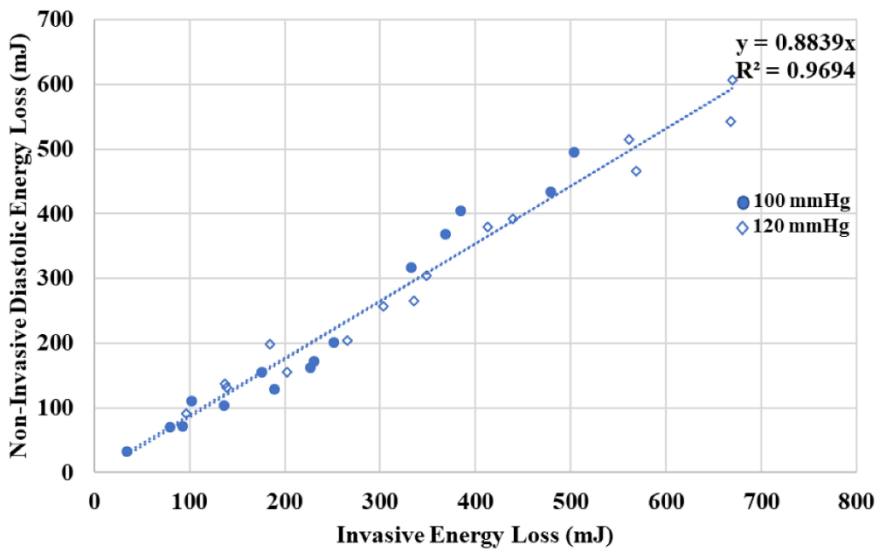

Figure 5.9: Linear correlation between the measured energy loss invasively and noninvasively during diastole.

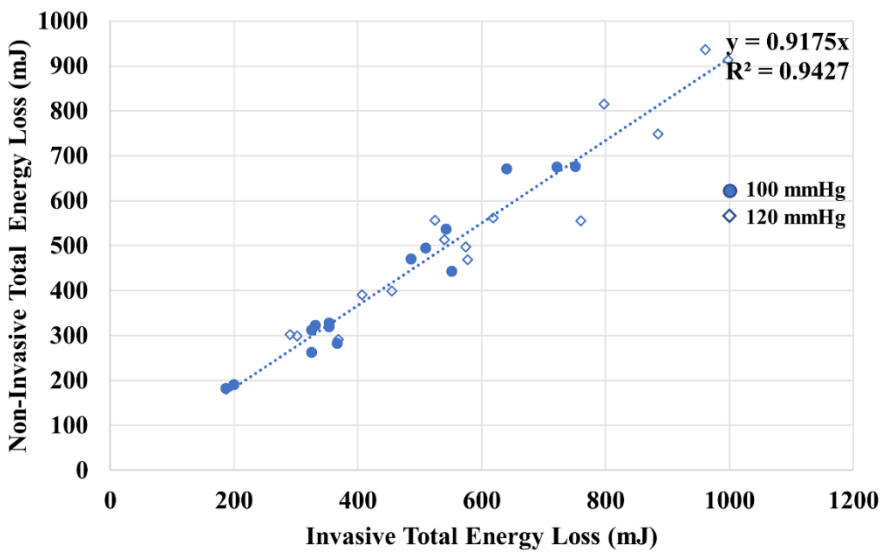

Figure 5.10: Linear correlation between the measured energy loss invasively and noninvasively during the cardiac cycle.

5.5 Conclusion

Measuring RV is the most accurate way of evaluating the severity of PVL, however there is no clinical way to measure RV in patient via the current tools. On the other hand, energy loss is a well-established engineering approach which provides evaluation of TAVs performance and during systole and accounts for any regurgitation during diastole. TAV devices have emerged as an alternative treatment for patients at high risk of open-heart surgery with severe aortic stenosis. Nevertheless, PVL is still frequent clinical complication post TAV implementation. Estimating the severity of PVL is still quite challenging, however, the good agreement between invasive and non-invasive energy loss approves the ability of using energy loss to estimate RV non-invasively. Additionally, we demonstrate the significant workload imposes in the left ventricle which could lead to heart failure. Even with the last generation of TAVs, PVL is expected to remain one of the major clinical issue post TAV implementation.

Chapter 6: Conclusion and Future work

TAVR is a minimally invasive treatment to replace a calcified aortic valve or a degenerated surgical bioprosthetic valve. Unlike surgical valve, TAVR is delivered through a catheter to the affected valve. Previously, the FDA approved TAVR only in patients at high risk of open-heart surgery with limited life expectancy. Recently, the FDA approved TAVR in young patients at low risk of open-heart surgery. In contract to SAV, there are no enough clinical data in term of the fluid dynamics performance of TAV devices. Another clinical challenging is associated with evaluating the performance of TAV post the operation non-invasively and evaluate the overall performance of the valve. Therefore, experimental testing and computational modeling become an important part to evaluate the performance of TAV devices. Consequently, the objectives of this dissertation were to employ experimental testing to investigate the source of clinical issues that are associated with TAV devices, and to validate computational modeling which were developed to obtain close visualization of areas where it's impossible to visual experimentally.

It's been demonstrated that the velocity profile generated by TAVs has been known to play a critical role in thrombotic and hemolytic complications associated with prosthetic heart valves. Therefore, the main goal of this dissertation was to investigate weather stroke happened due to shear induced in TAVs, also to explain the reason behind valvular thrombosis among TAVR patients. Additionally, there is a lack of validated method to estimate the severity of PVL. Thus, I validated semi-quantitative methods that are commonly used to assess the severity of PVL post-TAVR. In the same manner, I introduced a new methodology to classify the severity of

PVL based on fluid dynamics using parameters that can be measured using echocardiography. Moreover, Energy loss is an excellent parameter to evaluate the performance of TAVs, not only allows evaluation of TAV performance during systole, but also allows quantification of PVL during diastole. Therefore, developing and validating non-invasive procedure to estimate energy loss post-TAVR during the cardiac cycle were performed and the workload imposes on the left ventricle was measured.

6.1 Conclusion

Several clinical data have revealed high rate of cerebral emboli among TAVR patients, even in a short time after the procedure. On the other side, it's been known that fluid dynamics play an important role in understanding progression of diseases that are associated with TAVs such as stroke. In this study, the velocity and shear stress magnitude downstream of two commercially available TAV devices were measured throughout a cardiac cycle. Additionally, the hemodynamic performance of TAV devices was compared to a surgical valve in term of mean pressure gradient and orifice effective area. The result of this study revealed that shear stress magnitude of TAV devices was only detected at the peak of flow with low magnitude. The hemodynamic performance of TAVs were comparable and even exceed the performance of the surgical valve. The detected shear stress was below the known threshold for red blood damage and platelet activation. Therefore, it's unlikely that stroke accrue due to high shear induced in TAVs.

Reduced leaflet motion due to valvular thrombosis has been observed among TAVR patients even in a few days after the procedure. Valvular thrombosis was predominantly found on the aortic surface of the valve leaflets. To address the cause of thrombosis formation on TAV leaflets, experimental testing and computational modeling were developed. The hypothesis of this study was based on investigating blood stasis in geometric confinement of TAV device. The

experimental flow field was obtained to validate the flow field that was obtained from the computational simulation. In this study two geometrical models were developed; one represents surgical valve and the other represents the geometric confinement of TAV. After validating the flow field of the simulation, a randomly distributed massless particles were generated in the flow field in both models. The result of this study illustrated longer particles stasis in TAV model in compare to the surgical valve model where the particles washed away especially during diastole. Therefore, we could conclude that the geometric confinement of TAV increase blood stasis between the outer surface of TAV leaflet and the inner surface of the calcified valve, which increase the likelihood of thrombosis formation on TAV leaflet.

PVL is a frequent clinical complication post-TAVR procedure due to the natural of TAV implementation. Unlike surgical valve where the calcified valve is removed and replace it with a bioprosthetic valve, TAV is implanted over the calcified valve or a degenerated bioprosthetic valve (ViV). The only accurate way to estimate the severity of PVL is by measuring leakage volume directly, however, measuring PVL volume is significant challenging and pricy. Nevertheless, there is a lack of validated protocol to evaluate PVL post TAVR and ensure appropriate classification of its severity. On the other hand, the CE of PVL was introduced by to estimate the severity of PVL non-invasively. The goal of this study was to validate CE of PVL experimentally, and to introduce a new methodology base on fluid dynamics to estimate the severity of PVL. The result of this chapter illustrated that CE over-predicate the severity of PVL, and its shown poor correlation with the measured RV. However, the maximum momentum flux of PVL shows an excellent correlation with the measured RV, which could be used as a new tool to assess the severity of PVL post TAVR.

Energy loss is a well-established engineering approach that use to evaluate the performance of bioprosthetic heart valves post procedure. Substantial energy loss during diastole

occurs due to PVL, even in the presence of mild PVL. The concept of energy loss has not been widely used in clinics, because the measurement of energy loss in patients require invasive measurements of instantaneous temporal of pressures and velocities directly from the heart. However, in this study we developed a method to estimate energy loss non-invasively using doppler echocardiography. In this work the invasive energy loss was measured directly from the pulse duplicator, while the non-invasive energy loss was calculated using parameters obtained from the echocardiography. The result of this study demonstrated a significant correlation between the measured RV and energy loss invasively. The energy loss obtained from non-invasive measurements match well with invasive measurement. Therefore, energy loss could be used to estimate the severity of PVL accurately. Also, the experimental results showed significant workload on the left ventricle due the present of PVL jets. Energy loss could be used as a quantitative parameter to quantify the severity of PVL precisely.

6.2 Future Works

A few limitations are associated with the study in chapter 2 that should have been addressed as future work. In this chapter, we only used two commercially available of TAV devices which were SAPIEN 3 and CoreValve because they are widely used in clinical trial and practice. However, each year the heart valve industries release different designs and configurations of TAVs, therefore, studying the flow field of the most recent generation of TAVs, will benefit in validating computational modeling. To understanding the structure of flow field during diastole, a 3D-PIV system should be used to obtain flow field of TAVs. In addition, multiple parameters such as Reynold shear stress (RSS) and vorticity should be measured. Furthermore, Echo-PIV can be performed in the future simultaneously to assess the overall performance of TAVs in term of hemodynamics measurements.

In this dissertation, we developed a hypothesis to address the issue behind reduced leaflet motion among TAVR patients. Due to the complexity of the TAVR setting, we used a validated computational modeling to visualize the blood motion between the calcified valve and TAV using BRT approach. Applying the BRT approach to address the likelihood of thrombosis formation in patients post transcatheter mitral valve replacement (TMVR). In addition, testing multiple devices of TAV could be more valuable since super-annular valve such as CoreValve might not show large BRT in compare to annular valves such as SAPIEN 3. Also including valves types, size and positioning of TAV device, as well as considering anatomic structure such as coronary and non-coronary leaflets in the CFD-model.

In this dissertation we illustrated that the CE of PVL over-estimate the severity of PVL post-TAVR procedure. The introduced non-invasive energy loss formula cannot be accomplished without estimating RV of the PVL. Therefore, the maximum momentum flux method can be used to estimate RV first in the future, then the obtained RV can be used to calculated energy loss non-invasively. Additionally, we would like to see the energy loss method being applied to large population of TAVR patients non-invasively.

Bibliography

Abbasi, M., Barakat, M. S., Vahidkhah, K., & Azadani, A. N. (2016). Characterization of three-dimensional anisotropic heart valve tissue mechanical properties using inverse finite element analysis. *Journal of the mechanical behavior of biomedical materials, 62*, 33-44.

Adams, D. H., Popma, J. J., Reardon, M. J., Yakubov, S. J., Coselli, J. S., Deeb, G. M., . . . Kleiman, N. S. (2014). Transcatheter aortic-valve replacement with a self-expanding prosthesis. *New England Journal of Medicine, 370*(19), 1790-1798.

Akhras, N., Al Sergani, H., Al Buraiki, J., Fadel, B. M., Khaliel, F., Al Allaf, A., . . . Dahdouh, Z. (2016). Thrombolytic therapy as the management of mitral transcatheter valve-in-valve implantation early thrombosis. *Heart, Lung and Circulation, 25*(5), e65-e68.

Akins, C. W., Travis, B., & Yoganathan, A. P. (2008). Energy loss for evaluating heart valve performance. *The Journal of Thoracic and Cardiovascular Surgery, 136*(4), 820-833.

Alemu, Y., & Bluestein, D. (2007). Flow-induced platelet activation and damage accumulation in a mechanical heart valve: numerical studies. *Artificial organs, 31*(9), 677-688.

Anning, S. (1957). The historical aspects of venous thrombosis. *Medical history, 1*(1), 28-37.

Aranki, S., Rizzo, R., Couper, G., Adams, D., Collins, J. J., Gildea, J., . . . Cohn, L. (1993). Aortic valve replacement in the elderly. Effect of gender and coronary artery disease on operative mortality. *Circulation, 88*(5 Pt 2), II17-23.

Arnold, M., Schulz-Heise, S., Achenbach, S., Ott, S., Dörfler, A., Ropers, D., . . . Mahmoud, F. (2010). Embolic cerebral insults after transapical aortic valve implantation detected by magnetic resonance imaging. *JACC: Cardiovascular Interventions, 3*(11), 1126-1132.

Association, A. H. (2002). Heart disease and stroke statistics-2003 update. *http://www. americanheart. org/downloadable/heart/10590179711482003HDSStatsBookREV7-03. pdf.*

Association, A. H. (2017). Heart disease and stroke statistics 2017 at-a-glance. *Geraadpleegd van: https://healthmetrics. heart. org/wp-content/uploads/2017/06/Heart-Disease-and-Stroke-Statistics-2017-ucm_491265. pdf.*

Astarci, P., Glineur, D., Kefer, J., D'Hoore, W., Renkin, J., Vanoverschelde, J.-L., . . . Grandin, C. (2011). Magnetic resonance imaging evaluation of cerebral embolization during percutaneous aortic valve implantation: comparison of transfemoral and trans-apical approaches using Edwards Sapiens valve. *European Journal of Cardio-Thoracic Surgery, 40*(2), 475-479.

Athappan, G., Patvardhan, E., Tuzcu, E. M., Svensson, L. G., Lemos, P. A., Fraccaro, C., . . . Capodanno, D. (2013). Incidence, predictors, and outcomes of aortic regurgitation after transcatheter aortic valve replacement: meta-analysis and systematic review of literature. *Journal of the American College of Cardiology, 61*(15), 1585-1595.

Azadani, A. N., Jaussaud, N., Matthews, P. B., Ge, L., Guy, T. S., Chuter, T. A., & Tseng, E. E. (2009). Energy loss due to paravalvular leak with transcatheter aortic valve implantation. *The Annals of thoracic surgery, 88*(6), 1857-1863.

Azadani, A. N., & Tseng, E. E. (2010). Transcatheter valve-in-valve implantation for failing bioprosthetic valves. *Future cardiology, 6*(6), 811-831.

Azadani, A. N., & Tseng, E. E. (2011). Transcatheter heart valves for failing bioprostheses: state-of-the-art review of valve-in-valve implantation. *Circulation: Cardiovascular Interventions, 4*(6), 621-628.

Barakat, M., Dvir, D., & Azadani, A. N. (2018). Fluid dynamic characterization of transcatheter aortic valves using particle image velocimetry. *Artificial organs, 42*(11), E357-E368.

Barbanti, M., Webb, J. G., Gilard, M., Capodanno, D., & Tamburino, C. (2017). Transcatheter aortic valve implantation in 2017: state of the art. *EuroIntervention, 13*(AA), AA11-AA21.

Baumgartner, H., Hung, J., Bermejo, J., Chambers, J. B., Evangelista, A., Griffin, B. P., . . . Quiñones, M. (2009). Echocardiographic assessment of valve stenosis: EAE/ASE recommendations for clinical practice. *Journal of the American Society of Echocardiography, 22*(1), 1-23.

Becker, R. C., Eisenberg, P., & Turpie, A. (2001). Pathobiologic features and prevention of thrombotic complications associated with prosthetic heart valves: fundamental principles and the contribution of platelets and thrombin. *American heart journal, 141*(6), 1025.

Benjamin, E. J., Muntner, P., & Bittencourt, M. S. (2019). Heart disease and stroke statistics-2019 update: a report from the American Heart Association. *Circulation, 139*(10), e56-e528.

Bevan, G. H., Zidar, D. A., Josephson, R. A., & Al-Kindi, S. G. (2019). Mortality Due to Aortic Stenosis in the United States, 2008-2017. *Jama, 321*(22), 2236-2238.

Bhindi, R., Bull, S., Schrale, R. G., Wilson, N., & Ormerod, O. J. (2008). Surgery insight: percutaneous treatment of prosthetic paravalvular leaks. *Nature Clinical Practice Cardiovascular Medicine, 5*(3), 140-147.

Bloomfield, G. S., Gillam, L. D., Hahn, R. T., Kapadia, S., Leipsic, J., Lerakis, S., . . . Douglas, P. S. (2012). A practical guide to multimodality imaging of transcatheter aortic valve replacement. *JACC: Cardiovascular Imaging, 5*(4), 441-455.

Bluestein, D., Niu, L., Schoephoerster, R. T., & Dewanjee, M. K. (1997). Fluid mechanics of arterial stenosis: relationship to the development of mural thrombus. *Annals of biomedical engineering, 25*(2), 344.

Brown, M. L., Park, S. J., Sundt, T. M., & Schaff, H. V. (2012). Early thrombosis risk in patients with biologic valves in the aortic position. *The Journal of Thoracic and Cardiovascular Surgery, 144*(1), 108-111.

Carabello, B. A. (2011). Transcatheter aortic-valve implantation for aortic stenosis in patients who cannot undergo surgery. *Current cardiology reports, 13*(3), 173-174.

Chakos, A., Wilson-Smith, A., Arora, S., Nguyen, T. C., Dhoble, A., Tarantini, G., . . . Yan, T. D. (2017). Long term outcomes of transcatheter aortic valve implantation (TAVI): a systematic review of 5-year survival and beyond. *Annals of cardiothoracic surgery, 6*(5), 432.

Chakravarty, T., Abramowitz, Y., Jilaihawi, H., & Makkar, R. R. (2016). Leaflet motion abnormality after TAVI: genuine threat or much ado about nothing? *EuroIntervention: journal of EuroPCR in collaboration with the Working Group on Interventional Cardiology of the European Society of Cardiology, 12*(Y), Y28-32.

Chakravarty, T., Søndergaard, L., Friedman, J., De Backer, O., Berman, D., Kofoed, K. F., . . . Jørgensen, T. H. (2017). Subclinical leaflet thrombosis in surgical and transcatheter bioprosthetic aortic valves: an observational study. *The Lancet, 389*(10087), 2383-2392.

Clark, M. A., Duhay, F. G., Thompson, A. K., Keyes, M. J., Svensson, L. G., Bonow, R. O., . . . Cohen, D. J. (2012). Clinical and economic outcomes after surgical aortic valve replacement in Medicare patients. *Risk management and healthcare policy, 5*, 117.

Clavel, M.-A., Webb, J. G., Pibarot, P., Altwegg, L., Dumont, E., Thompson, C., . . . Bergeron, S. (2009). Comparison of the hemodynamic performance of percutaneous and surgical bioprostheses for the treatment of severe aortic stenosis. *Journal of the American College of Cardiology, 53*(20), 1883-1891.

Coffey, S., d'Arcy, J. L., Loudon, M. A., Mant, D., Farmer, A. J., & Prendergast, B. D. (2014). The OxVALVE population cohort study (OxVALVE-PCS)—population screening for undiagnosed valvular heart disease in the elderly: study design and objectives. *Open heart, 1*(1), e000043.

Córdoba-Soriano, J. G., Puri, R., Amat-Santos, I., Ribeiro, H. B., Altisent, O. A.-J., del Trigo, M., . . . Rodés-Cabau, J. (2015). Valve thrombosis following transcatheter aortic valve implantation: a systematic review. *Revista Española de Cardiología (English Edition), 68*(3), 198-204.

Coylewright, M., Forrest, J. K., McCabe, J. M., & Nazif, T. M. (2020). TAVR in Low-Risk Patients. *Journal of the American College of Cardiology, 75*(10).

Cribier, A., Eltchaninoff, H., Bash, A., Borenstein, N., Tron, C., Bauer, F., . . . Leon, M. B. (2002). Percutaneous transcatheter implantation of an aortic valve prosthesis for calcific aortic stenosis: first human case description. *Circulation, 106*(24), 3006-3008.

Dasi, L. P., Simon, H. A., Sucosky, P., & Yoganathan, A. P. (2009). Fluid mechanics of artificial heart valves. *Clinical and experimental pharmacology and physiology, 36*(2), 225-237.

Daubert, M. A., Weissman, N. J., Hahn, R. T., Pibarot, P., Parvataneni, R., Mack, M. J., . . . Siegel, R. J. (2017). Long-term valve performance of TAVR and SAVR: a report from the PARTNER I trial. *JACC: Cardiovascular Imaging, 10*(1), 15-25.

De Marchena, E., Mesa, J., Pomenti, S., y Kall, C. M., Marincic, X., Yahagi, K., . . . Ragosta, M. (2015). Thrombus formation following transcatheter aortic valve replacement. *JACC: Cardiovascular Interventions, 8*(5), 728-739.

De Santo, L. S., Romano, G., Della Corte, A., D'Oria, V., Nappi, G., Giordano, S., . . . De Feo, M. (2012). Mechanical aortic valve replacement in young women planning on pregnancy: maternal and fetal outcomes under low oral anticoagulation, a pilot observational study on a comprehensive pre-operative counseling protocol. *Journal of the American College of Cardiology, 59*(12), 1110-1115.

Del Trigo, M., Muñoz-Garcia, A. J., Wijeysundera, H. C., Nombela-Franco, L., Cheema, A. N., Gutierrez, E., . . . Benitez, L. M. (2016). Incidence, timing, and predictors of valve hemodynamic deterioration after transcatheter aortic valve replacement: multicenter registry. *Journal of the American College of Cardiology, 67*(6), 644-655.

Dencker, D., Taudorf, M., Luk, N. V., Nielsen, M. B., Kofoed, K. F., Schroeder, T. V., . . . De Backer, O. (2016). Frequency and effect of access-related vascular injury and subsequent vascular intervention after transcatheter aortic valve replacement. *The American journal of cardiology, 118*(8), 1244-1250.

Ducci, A., Tzamtzis, S., Mullen, M. J., & Burriesci, G. (2013). Hemodynamics in the Valsalva sinuses after transcatheter aortic valve implantation (TAVI). *J Heart Valve Dis, 22*(5), 688-696.

Dvir, D., Webb, J. G., Bleiziffer, S., Pasic, M., Waksman, R., Kodali, S., . . . Rodés-Cabau, J. (2014). Transcatheter aortic valve implantation in failed bioprosthetic surgical valves. *Jama, 312*(2), 162-170.

Dwyer, H. A., Matthews, P. B., Azadani, A., Jaussaud, N., Ge, L., Guy, T. S., & Tseng, E. E. (2009). Computational fluid dynamics simulation of transcatheter aortic valve degeneration. *Interactive cardiovascular and thoracic surgery, 9*(2), 301-308.

Egbe, A. C., Pislaru, S. V., Pellikka, P. A., Poterucha, J. T., Schaff, H. V., Maleszewski, J. J., & Connolly, H. M. (2015). Bioprosthetic valve thrombosis versus structural failure: clinical and echocardiographic predictors. *Journal of the American College of Cardiology, 66*(21), 2285-2294.

Friedrich, P., & Reininger, A. J. (1995). Occlusive thrombus formation on indwelling catheters: in vitro investigation and computational analysis. *Thrombosis and haemostasis, 73*(01), 066-072.

Garcia, D., Pibarot, P., Dumesnil, J. G., Sakr, F. d. r., & Durand, L.-G. (2000). Assessment of aortic valve stenosis severity: a new index based on the energy loss concept. *Circulation, 101*(7), 765-771.

Ge, L., Dasi, L. P., Sotiropoulos, F., & Yoganathan, A. P. (2008). Characterization of hemodynamic forces induced by mechanical heart valves: Reynolds vs. viscous stresses. *Annals of biomedical engineering, 36*(2), 276-297.

Geleijnse, M. L., Di Martino, L. F., Vletter, W. B., Ren, B., Galema, T. W., Van Mieghem, N. M., . . . Soliman, O. I. (2015). Limitations and difficulties of echocardiographic short-axis assessment of paravalvular leakage after corevalve transcatheter aortic valve implantation. *Cardiovascular ultrasound, 14*(1), 37.

Ghanem, A., Müller, A., Nähle, C. P., Kocurek, J., Werner, N., Hammerstingl, C., . . . Fimmers, R. (2010). Risk and fate of cerebral embolism after transfemoral aortic valve implantation: a prospective pilot study with diffusion-weighted magnetic resonance imaging. *Journal of the American College of Cardiology, 55*(14), 1427-1432.

Goodman, P. D., Barlow, E. T., Crapo, P. M., Mohammad, S. F., & Solen, K. A. (2005). Computational model of device-induced thrombosis and thromboembolism. *Annals of biomedical engineering, 33*(6), 780-797.

Gorbet, M. B., & Sefton, M. V. (2004). Biomaterial-associated thrombosis: roles of coagulation factors, complement, platelets and leukocytes *The Biomaterials: Silver Jubilee Compendium* (pp. 219-241): Elsevier.

Gotzmann, M., Korten, M., Bojara, W., Lindstaedt, M., Rahlmann, P., Mügge, A., & Ewers, A. (2012). Long-term outcome of patients with moderate and severe prosthetic aortic valve regurgitation after transcatheter aortic valve implantation. *The American journal of cardiology, 110*(10), 1500-1506.

Gotzmann, M., Pljakic, A., Bojara, W., Lindstaedt, M., Ewers, A., Germing, A., & Mügge, A. (2011). Transcatheter aortic valve implantation in patients with severe symptomatic aortic valve stenosis—predictors of mortality and poor treatment response. *American heart journal, 162*(2), 238-245. e231.

Groves, E. M., Falahatpisheh, A., Su, J. L., & Kheradvar, A. (2014). The effects of positioning of transcatheter aortic valve on fluid dynamics of the aortic root. *ASAIO journal (American Society for Artificial Internal Organs: 1992), 60*(5), 545.

Grube, E., Schuler, G., Buellesfeld, L., Gerckens, U., Linke, A., Wenaweser, P., . . . Zickmann, B. (2007). Percutaneous aortic valve replacement for severe aortic stenosis in high-risk patients using the second-and current third-generation self-expanding CoreValve prosthesis: device success and 30-day clinical outcome. *Journal of the American College of Cardiology, 50*(1), 69-76.

Grunkemeier, G. L., & Rahimtoola, S. H. (1990). Artificial heart valves. *Annual review of medicine, 41*(1), 251-263.

Hahn, R. T., Pibarot, P., Stewart, W. J., Weissman, N. J., Gopalakrishnan, D., Keane, M. G., . . . Lindman, B. R. (2013). Comparison of transcatheter and surgical aortic valve replacement in severe aortic stenosis: a longitudinal study of echocardiography parameters in cohort A of the PARTNER trial (placement of aortic transcatheter valves). *Journal of the American College of Cardiology, 61*(25), 2514-2521.

Hamm, C. W., Möllmann, H., Holzhey, D., Beckmann, A., Veit, C., Figulla, H.-R., . . . Zahn, R. (2013). The German aortic valve registry (GARY): in-hospital outcome. *European heart journal, 35*(24), 1588-1598.

Hansson, N. C., Grove, E. L., Andersen, H. R., Leipsic, J., Mathiassen, O. N., Jensen, J. M., . . . Tang, M. (2016). Transcatheter aortic valve thrombosis: incidence, predisposing factors, and clinical implications. *Journal of the American College of Cardiology, 68*(19), 2059-2069.

Hsu, M.-C., Kamensky, D., Xu, F., Kiendl, J., Wang, C., Wu, M. C., . . . Sacks, M. S. (2015). Dynamic and fluid–structure interaction simulations of bioprosthetic heart valves using parametric design with T-splines and Fung-type material models. *Computational mechanics, 55*(6), 1211-1225.

Hung, T., Hochmuth, R., Joist, J., & Sutera, S. (1976). Shear-induced aggregation and lysis of platelets. *ASAIO Journal, 22*(1), 285-290.

Ionescu, A., Fraser, A. G., & Butchart, E. (2003). Prevalence and clinical significance of incidental paraprosthetic valvar regurgitation: a prospective study using transoesophageal echocardiography. *Heart, 89*(11), 1316-1321.

Isaacs, A. J., Shuhaiber, J., Salemi, A., Isom, O. W., & Sedrakyan, A. (2015). National trends in utilization and in-hospital outcomes of mechanical versus bioprosthetic aortic valve replacements. *The Journal of Thoracic and Cardiovascular Surgery, 149*(5), 1262-1269. e1263.

Iung, B., Baron, G., Butchart, E. G., Delahaye, F., Gohlke-Bärwolf, C., Levang, O. W., . . . Boersma, E. (2003). A prospective survey of patients with valvular heart disease in Europe: The Euro Heart Survey on Valvular Heart Disease. *European heart journal, 24*(13), 1231-1243.

Jilaihawi, H., Kashif, M., Fontana, G., Furugen, A., Shiota, T., Friede, G., . . . Makkar, R. R. (2012). Cross-sectional computed tomographic assessment improves accuracy of aortic annular sizing for transcatheter aortic valve replacement and reduces the incidence of paravalvular aortic regurgitation. *Journal of the American College of Cardiology, 59*(14), 1275-1286.

Jones, S. A. (1995). A relationship between Reynolds stresses and viscous dissipation: implications to red cell damage. *Annals of biomedical engineering, 23*(1), 21-28.

Kahlert, P., Knipp, S., Schlamann, M., Thielmann, M., Johansson, U., Wendt, D., . . . Erbel, R. (2009). *Silent and apparent cerebral ischemia after percutaneous transfemoral aortic valve implantation.* Paper presented at the AMERICAN JOURNAL OF CARDIOLOGY.

Kappetein, A. P., Head, S. J., Généreux, P., Piazza, N., Van Mieghem, N. M., Blackstone, E. H., . . . van Es, G.-A. (2012). Updated standardized endpoint definitions for transcatheter aortic valve implantation: the Valve Academic Research Consortium-2 consensus document. *Journal of the American College of Cardiology, 60*(15), 1438-1454.

Karino, T., & Goldsmith, H. (1979). Aggregation of human platelets in an annular vortex distal to a tubular expansion. *Microvascular research, 17*(3), 217-237.

Kheradvar, A., Groves, E. M., Goergen, C. J., Alavi, S. H., Tranquillo, R., Simmons, C. A., . . . Falahatpisheh, A. (2015). Emerging trends in heart valve engineering: Part II. Novel and standard technologies for aortic valve replacement. *Annals of biomedical engineering, 43*(4), 844-857.

Kobayashi, T., Giri, J., Vallabhajosyula, P., Herrmann, H. C., & Jagasia, D. H. (2015). Overestimation of paravalvular leak with Edwards SAPIEN 3 transcatheter aortic valve replacement. *JACC: Cardiovascular Interventions, 8*(5), e69-e71.

Kodali, S. K., Williams, M. R., Smith, C. R., Svensson, L. G., Webb, J. G., Makkar, R. R., . . . Pichard, A. D. (2012). Two-year outcomes after transcatheter or surgical aortic-valve replacement. *New England Journal of Medicine, 366*(18), 1686-1695.

Krishnaswamy, A., Kapadia, S. R., & Tuzcu, E. M. (2012). Percutaneous paravalvular leak closure. *Circulation Journal*, CJ-12-1433.

Külling, M., Külling, J., Wyss, C., Hürlimann, D., Reho, I., Salzberg, S., . . . Corti, R. (2017). Effective orifice area and hemodynamic performance of the transcatheter Edwards Sapien 3 prosthesis: short-term and 1-year follow-up. *European Heart Journal-Cardiovascular Imaging, 19*(1), 23-30.

Lang, R., Bierig, M., Devereux, R., Flachskampf, F., Foster, E., Pellikka, P., . . . Shanewise, J. (2005). A report from the American Society of Echocardiography's Guidelines and Standards Committee and the Chamber Quantification Writing Group, developed in conjunction with the European Association of Echocardiography, a branch of the European Society of Cardiology. *J Am Soc Echocardiogr, 18*(12), 1440-1463.

Lansky, A. J., Schofer, J., Tchetche, D., Stella, P., Pietras, C. G., Parise, H., . . . Reinöhl, J. (2015). A prospective randomized evaluation of the TriGuard™ HDH embolic DEFLECTion device during transcatheter aortic valve implantation: results from the DEFLECT III trial. *European heart journal, 36*(31), 2070-2078.

Latib, A., Naganuma, T., Abdel-Wahab, M., Danenberg, H., Cota, L., Barbanti, M., . . . De Lezo, J. S. (2015). Treatment and clinical outcomes of transcatheter heart valve thrombosis. *Circulation: Cardiovascular Interventions, 8*(4), e001779.

Leetmaa, T., Hansson, N. C., Leipsic, J., Jensen, K., Poulsen, S. H., Andersen, H. R., . . . Tang, M. (2015). Early aortic transcatheter heart valve thrombosis: diagnostic value of contrast-enhanced multidetector computed tomography. *Circulation: Cardiovascular Interventions, 8*(4), e001596.

Leon, M., Smith, C., Mack, M., Miller, D., Moses, J., Svensson, L., . . . Makkar, R. (2010). Pocock S; PARTNER Trial Investigators. Transcatheter aortic-valve implantation for aortic stenosis in patients who cannot undergo surgery. *N Engl J Med, 363*(17), 1597-1607.

Leon, M. B., Smith, C. R., Mack, M. J., Makkar, R. R., Svensson, L. G., Kodali, S. K., . . . Herrmann, H. C. (2016). Transcatheter or surgical aortic-valve replacement in intermediate-risk patients. *New England Journal of Medicine, 374*(17), 1609-1620.

Leverett, L., Hellums, J., Alfrey, C., & Lynch, E. (1972). Red blood cell damage by shear stress. *Biophysical journal, 12*(3), 257-273.

Linden, B., Leon, M., Smith, C., Mack, M., & Investigators, P. T. (2011). Transcatheter aortic-valve implantation for aortic stenosis in patients who cannot undergo surgery. *British Journal of Cardiac Nursing, 6*(1), 48-48.

Litzler, P.-Y., Cribier, A., Zajarias, A., Comte, D., Eltchaninoff, H., Tron, C., . . . Bessou, J.-P. (2008). Surgical aortic valve replacement after percutaneous aortic valve implantation: What have we learned? *The Journal of Thoracic and Cardiovascular Surgery, 136*(3), 697-701.

Mack, M., & Holmes, D. (2016). Bioprosthetic valve thrombosis: the harder one looks, the more one finds. *The Journal of Thoracic and Cardiovascular Surgery, 152*(4), 952-953.

Makkar, R. R., Fontana, G., Jilaihawi, H., Chakravarty, T., Kofoed, K. F., De Backer, O., . . . Trento, A. (2015). Possible subclinical leaflet thrombosis in bioprosthetic aortic valves. *New England Journal of Medicine, 373*(21), 2015-2024.

Makkar, R. R., Fontana, G. P., Jilaihawi, H., Kapadia, S., Pichard, A. D., Douglas, P. S., . . . Herrmann, H. C. (2012). Transcatheter aortic-valve replacement for inoperable severe aortic stenosis. *New England Journal of Medicine, 366*(18), 1696-1704.

Maraj, R., Jacobs, L. E., Ioli, A., & Kotler, M. N. (1998). Evaluation of hemolysis in patients with prosthetic heart valves. *Clinical cardiology, 21*(6), 387-392.

Martí, D., Rubio, M., Escribano, N., de Miguel, R., Rada, I., & Morís, C. (2015). Very late thrombosis of a transcatheter aortic valve-in-valve. *JACC: Cardiovascular Interventions, 8*(9), e151-e153.

Members, A. T. F., Vahanian, A., Alfieri, O., Andreotti, F., Antunes, M. J., Barón-Esquivias, G., . . . De Bonis, M. (2012). Guidelines on the management of valvular heart disease (version 2012) The Joint Task Force on the Management of Valvular Heart Disease of the European Society of Cardiology (ESC) and the European Association for Cardio-Thoracic Surgery (EACTS). *European heart journal, 33*(19), 2451-2496.

Midha, P. A., Raghav, V., Condado, J. F., Arjunon, S., Uceda, D. E., Lerakis, S., . . . Yoganathan, A. P. (2015). How can we help a patient with a small failing bioprosthesis?: an in vitro case study. *JACC: Cardiovascular Interventions, 8*(15), 2026-2033.

Midha, P. A., Raghav, V., Sharma, R., Condado, J. F., Okafor, I. U., Rami, T., . . . Babaliaros, V. (2017). The fluid mechanics of transcatheter heart valve leaflet thrombosis in the neosinus. *Circulation, 136*(17), 1598-1609.

Moore, B. L., & Dasi, L. P. (2015). Coronary flow impacts aortic leaflet mechanics and aortic sinus hemodynamics. *Annals of biomedical engineering, 43*(9), 2231-2241.

Morris, P. D., Narracott, A., von Tengg-Kobligk, H., Soto, D. A. S., Hsiao, S., Lungu, A., . . . Hose, D. R. (2016). Computational fluid dynamics modelling in cardiovascular medicine. *Heart, 102*(1), 18-28.

Neragi-Miandoab, S., & Michler, R. E. (2013). A review of most relevant complications of transcatheter aortic valve implantation. *ISRN cardiology, 2013*.

Nishimura, R., Otto, C., Bonow, R., Carabello, B., Erwin, J., Guyton, R., . . . Sorajja, P. (2014). Correction: 2014 AHA/ACC guideline for the management of patients with valvular heart disease: Executive summary: A report of the American College of Cardiology/American Heart

Association Task Force on practice guidelines.(Journal of the American College of Cardiology (2014) 63 (2438-88)). *Journal of the American College of Cardiology, 63*(22).

Nkomo, V. T., Gardin, J. M., Skelton, T. N., Gottdiener, J. S., Scott, C. G., & Enriquez-Sarano, M. (2006). Burden of valvular heart diseases: a population-based study. *The Lancet, 368*(9540), 1005-1011.

Oberkampf, W. L., Trucano, T. G., & Hirsch, C. (2004). Verification, validation, and predictive capability in computational engineering and physics. *Applied Mechanics Reviews, 57*(5), 345-384.

Organization, W. H. (2004). *Rheumatic fever and rheumatic heart disease: report of a WHO Expert Consultation, Geneva, 29 October-1 November, 2001* (Vol. 923): World Health Organization.

Pibarot, P., Hahn, R. T., Weissman, N. J., & Monaghan, M. J. (2015). Assessment of paravalvular regurgitation following TAVR: a proposal of unifying grading scheme. *JACC: Cardiovascular Imaging, 8*(3), 340-360.

Raghav, V., Okafor, I., Quach, M., Dang, L., Marquez, S., & Yoganathan, A. P. (2016). Long-term durability of Carpentier-Edwards Magna Ease valve: a one billion cycle in vitro study. *The Annals of thoracic surgery, 101*(5), 1759-1765.

Rajamannan, N. M., Evans, F. J., Aikawa, E., Grande-Allen, K. J., Demer, L. L., Heistad, D. D., . . . O'Brien, K. D. (2011). Calcific aortic valve disease: not simply a degenerative process a review and agenda for research from the National Heart and Lung and Blood Institute Aortic Stenosis Working Group. *Circulation, 124*(16), 1783.

Ramstack, J., Zuckerman, L., & Mockros, L. (1979). Shear-induced activation of platelets. *Journal of biomechanics, 12*(2), 113-125.

Rayz, V., Boussel, L., Ge, L., Leach, J., Martin, A., Lawton, M., . . . Saloner, D. (2010). Flow residence time and regions of intraluminal thrombus deposition in intracranial aneurysms. *Annals of biomedical engineering, 38*(10), 3058-3069.

Reininger, A. J., Reininger, C. B., Heinzmann, U., & Wurzinger, L. J. (1995). Residence time in niches of stagnant flow determines fibrin clot formation in an arterial branching model-detailed flow analysis and experimental results. *Thrombosis and haemostasis, 73*(03), 916-922.

Ripley, B., Kelil, T., Cheezum, M. K., Goncalves, A., Di Carli, M. F., Rybicki, F. J., . . . Blankstein, R. (2016). 3D printing based on cardiac CT assists anatomic visualization prior to transcatheter aortic valve replacement. *Journal of cardiovascular computed tomography, 10*(1), 28-36.

Rodés-Cabau, J. (2012). Transcatheter aortic valve implantation: current and future approaches. *Nature Reviews Cardiology, 9*(1), 15.

Sirois, E., & Sun, W. (2011). Computational evaluation of platelet activation induced by a bioprosthetic heart valve. *Artificial organs, 35*(2), 157-165.

Sliwa, K., Carrington, M., Mayosi, B. M., Zigiriadis, E., Mvungi, R., & Stewart, S. (2009). Incidence and characteristics of newly diagnosed rheumatic heart disease in urban African adults: insights from the heart of Soweto study. *European heart journal, 31*(6), 719-727.

Smith, C. R., Leon, M. B., Mack, M. J., Miller, D. C., Moses, J. W., Svensson, L. G., . . . Makkar, R. R. (2011). Transcatheter versus surgical aortic-valve replacement in high-risk patients. *New England Journal of Medicine, 364*(23), 2187-2198.

Sondergaard, L. (2016). Time to explore transcatheter aortic valve replacement in younger, low-risk patients. *JACC: Cardiovascular Interventions, 9*(21), 2183-2185.

Spethmann, S., Dreger, H., Schattke, S., Baldenhofer, G., Saghabalyan, D., Stangl, V., . . . Knebel, F. (2012). Doppler haemodynamics and effective orifice areas of Edwards SAPIEN and CoreValve transcatheter aortic valves. *European Heart Journal–Cardiovascular Imaging, 13*(8), 690-696.

Stewart, S. F., Hariharan, P., Paterson, E. G., Burgreen, G. W., Reddy, V., Day, S. W., . . . Berman, M. R. (2013). Results of FDA's first interlaboratory computational study of a nozzle with a sudden contraction and conical diffuser. *Cardiovascular Engineering and Technology, 4*(4), 374-391.

Stewart, S. F., Paterson, E. G., Burgreen, G. W., Hariharan, P., Giarra, M., Reddy, V., . . . Berman, M. R. (2012). Assessment of CFD performance in simulations of an idealized medical device: results of FDA's first computational interlaboratory study. *Cardiovascular Engineering and Technology, 3*(2), 139-160.

Stühle, S., Wendt, D., Hou, G., Wendt, H., Schlamann, M., Thielmann, M., . . . Kowalczyk, W. (2011). In-vitro investigation of the hemodynamics of the Edwards Sapien™ transcatheter heart valve. *Journal of Heart Valve Disease, 20*(1), 53.

Sukavaneshvar, S. (2017). Device thrombosis and pre-clinical blood flow models for assessing antithrombogenic efficacy of drug-device combinations. *Advanced drug delivery reviews, 112*, 24-34.

Takkenberg, J., Rajamannan, N. M., Rosenhek, R., Kumar, A. S., Carapetis, J. R., & Yacoub, M. H. (2008). The need for a global perspective on heart valve disease epidemiology. The SHVD working group on epidemiology of heart valve disease founding statement. *The Journal of heart valve disease, 17*(1), 135-139.

Tan, F., Xu, X., Torii, R., Wood, N., Delahunty, N., Mullen, M., . . . Mohiaddin, R. (2012). Comparison of aortic flow patterns before and after transcatheter aortic valve implantation. *Cardiovascular Engineering and Technology, 3*(1), 123-135.

Tanaka, Y., Saito, S., Sasuga, S., Takahashi, A., Aoyama, Y., Obama, K., . . . Iwasaki, K. (2018). Quantitative assessment of paravalvular leakage after transcatheter aortic valve replacement using a patient-specific pulsatile flow model. *International journal of cardiology, 258*, 313-320.

Thourani, V. H., Li, C., Devireddy, C., Jensen, H. A., Kilgo, P., Leshnower, B. G., . . . Kanitkar, M. (2015). High-risk patients with inoperative aortic stenosis: use of transapical, transaortic, and transcarotid techniques. *The Annals of thoracic surgery, 99*(3), 817-825.

Vahanian, A., & Otto, C. M. (2010). Risk stratification of patients with aortic stenosis. *European heart journal, 31*(4), 416-423.

Vahidkhah, K., Abbasi, M., Barakat, M., Azadani, P. N., Tandar, A., Dvir, D., & Azadani, A. N. (2017). Effect of reduced cardiac output on blood stasis on transcatheter aortic valve leaflets: implications for valve thrombosis. *EuroIntervention: journal of EuroPCR in collaboration with the Working Group on Interventional Cardiology of the European Society of Cardiology, 13*(7), 811-819.

Vahidkhah, K., & Azadani, A. N. (2017). Supra-annular Valve-in-Valve implantation reduces blood stasis on the transcatheter aortic valve leaflets. *Journal of biomechanics, 58*, 114-122.

Vahidkhah, K., Barakat, M., Abbasi, M., Javani, S., Azadani, P. N., Tandar, A., . . . Azadani, A. N. (2017). Valve thrombosis following transcatheter aortic valve replacement: significance of blood stasis on the leaflets. *European Journal of Cardio-Thoracic Surgery, 51*(5), 927-935.

Vahidkhah, K., Cordasco, D., Abbasi, M., Ge, L., Tseng, E., Bagchi, P., & Azadani, A. N. (2016). Flow-induced damage to blood cells in aortic valve stenosis. *Annals of biomedical engineering, 44*(9), 2724-2736.

Vahidkhah, K., Javani, S., Abbasi, M., Azadani, P. N., Tandar, A., Dvir, D., & Azadani, A. N. (2017). Blood stasis on transcatheter valve leaflets and implications for valve-in-valve leaflet thrombosis. *The Annals of thoracic surgery, 104*(3), 751-759.

Vahl, T. P., Kodali, S. K., & Leon, M. B. (2016). Transcatheter aortic valve replacement 2016: a modern-day "through the looking-glass" adventure. *Journal of the American College of Cardiology, 67*(12), 1472-1487.

Van Belle, E., Hengstenberg, C., Lefevre, T., Kupatt, C., Debry, N., Husser, O., . . . Mehran, R. (2016). Cerebral embolism during transcatheter aortic valve replacement: the BRAVO-3 MRI study. *Journal of the American College of Cardiology, 68*(6), 589-599.

van Dalen, B. M., Bosch, J. G., Kauer, F., Soliman, O. I., Vletter, W. B., Folkert, J., & Geleijnse, M. L. (2009). Assessment of mitral annular velocities by speckle tracking echocardiography versus tissue Doppler imaging: validation, feasibility, and reproducibility. *Journal of the American Society of Echocardiography, 22*(11), 1302-1308.

Walther, T., Blumenstein, J., van Linden, A., & Kempfert, J. (2012). Contemporary management of aortic stenosis: surgical aortic valve replacement remains the gold standard. *Heart, 98*(Suppl 4), iv23-iv29.

Walther, T., & Falk, V. (2009). Hemodynamic evaluation of heart valve prostheses: paradigm shift for transcatheter valves? : Journal of the American College of Cardiology.

Webb, J. G., Pasupati, S., Humphries, K., Thompson, C., Altwegg, L., Moss, R., . . . Ricci, D. (2007). Percutaneous transarterial aortic valve replacement in selected high-risk patients with aortic stenosis. *Circulation, 116*(7), 755-763.

Williams, A. (1974). Release of serotonin from human platelets by acoustic microstreaming. *The Journal of the Acoustical Society of America, 56*(5), 1640-1643.

Yacoub, M., & Takkenberg, J. (2005). Will heart valve tissue engineering change the world? *Nature Reviews Cardiology, 2*(2), 60.

Yoganathan, A. P., He, Z., & Casey Jones, S. (2004). Fluid mechanics of heart valves. *Annu. Rev. Biomed. Eng., 6*, 331-362.

Zamorano, J. L., Badano, L. P., Bruce, C., Chan, K.-L., Gonçalves, A., Hahn, R. T., . . . Nihoyannopoulos, P. (2011). EAE/ASE recommendations for the use of echocardiography in new transcatheter interventions for valvular heart disease. *European heart journal, 32*(17), 2189-2214.

Zoghbi, W. A., Chambers, J. B., Dumesnil, J. G., Foster, E., Gottdiener, J. S., Grayburn, P. A., . . . Miller, F. A. (2009). Recommendations for evaluation of prosthetic valves with echocardiography and Doppler ultrasound: a report from the American Society of Echocardiography's Guidelines and Standards Committee and the Task Force on Prosthetic

Valves, developed in conjunction with the American College of Cardiology Cardiovascular Imaging Committee, Cardiac Imaging Committee of the American Heart Association, the European Association of Echocardiography, a registered branch of the European Society of Cardiology, the Japanese Society of Echocardiography and the Canadian Society of Echocardiography, endorsed by the American College of Cardiology Foundation, American Heart Association, European Association of Echocardiography, a registered branch of the European Society of Cardiology, the Japanese Society of Echocardiography, and Canadian Society of Echocardiography. *Journal of the American Society of Echocardiography, 22*(9), 975-1014.